STATISTICAL METHODS FOR COMPUTER AIDED DIAGNOSIS IN CHEST RADIOGRAPHY

HOSSEIN EBRAHIMIAN

DISSERTATION SUBMITTED IN FULFILMENT OF THE
REQUIREMENTS FOR THE DEGREE OF
MASTER OF SCIENCE

INSTITUTE OF MATHEMATICAL SCIENCES
FACULTY OF SCIENCE
UNIVERSITY OF MALAYA
KUALA LUMPUR

2013

UNIVERSITI MALAYA

ORIGINAL LITERARY WORK DECLARATION

Name of Candidate: **HOSSEIN EBRAHIMIAN** (passport No.: **J16624371**)

Registration / Matrix No.: **SGP100006**

Name of Degrees: **MASTER OF SCIENCE (M.Sc.)**

Title of Thesis ("this Work"):

STATISTICAL METHODS FOR COMPUTER AIDED DIAGNOSIS IN CHEST RADIOGRAPHY

Field of Study: **APPLIED STATISTICS**

I do solemnly and sincerely declare that:

(1) I am the sole author/writer of this Work;

(2) This Work is original;

(3) Any use of any work in which copyright exists was done by way of fair dealing and for permitted purposes and any excerpt or extract from, or reference to or reproduction of any copyright work has been disclosed expressly and sufficiently and the title of the Work and its authorship have been acknowledged in this Work;

(4) I do not have any actual knowledge nor do I ought reasonably to know that the making of this work constitutes an infringement of any copyright work;

(5) I hereby assign all and every rights in the copyright to this Work to the University of Malaya ("UM"), who henceforth shall be owner of the copyright in this Work and that any reproduction or use in any form or by any means whatsoever is prohibited without the written consent of UM having been first had and obtained;

(6) I am fully aware that if in the course of making this Work I have infringed any copyright whether intentionally or otherwise, I may be subject to legal action or any other action as may be determined by UM.

Candidate's Signature	Date:
HOSSEIN EBRAHIMIAN	**20 JULY 2013**

Subscribed and solemnly declared before,

Witness's Signature

Name:	Date:
DR. OMAR MOHD BIN RIJAL	**25 JULY 2013**

Designation:

SUPPERVISOR

ABSTRAK

Kajian ini dijalankan untuk membangunkan satu prosedur separa automatik bagi diskriminasi tiga penyakit paru-paru menggunakan radiograf dada. Prosedur statistik diskriminasi menggunakan keselarasan fasa dan sukatan tekstur sebagai ciri-ciri untuk diskriminasi.

Kajian literatur yang telah dijalankan menunjukkan bahawa keselarasan fasa belum pernah dikaji untuk prosedur diskriminasi yang dicadangkan. Kes-kes yang digunakan dalam kajian ini menggunakan filem X-ray dada pesakit dari Institut Perubatan Respiratori yang telah didigitkan ke format DICOM sebelum mengekstrak data pengimejan yang berkaitan.

Kajian ini dijalankan dalam tiga bahagian. Pertama, rantau jangkitan (ROI) untuk semua empat kes iaitu paru-paru normal (NL), kanser paru-paru (LC), lobar pneumonia (PNEU) dan tuberkulosis pulmonari (PTB) telah dikesan dalam satu applikasi baru yang menggunakan momen statistik. Kedua, ROI dalam bentuk piksel asal telah dijelmakan kepada nilai keselarasan fasa yang sepadan. Siasatan ke atas keupayaan keselarasan fasa sebagai ciri untuk diskriminasi dijalankan. Akhir sekali, sukatan tekstur dari nilai keselarasan fasa telah digunakan sebagai ciri-ciri global bagi tujuan diskriminasi.

Pilihan muktamad ciri-ciri untuk diskriminasi telah diputuskan selepas analisis ROC. Tenaga, kontras dan kehomogenan telah ditunjukkan untuk menjadi calon terbaik sebagai vektor ciri.

Akhir kata, gabungan prosedur untuk pencarian ROI dan prosedur diskriminasi yang dibangunkan membentuk prosedur diskriminasi separa automatik. Prosedur diskriminasi tersebut menjadi teras kepada diagnosis berbantukan komputer (CAD) yang dicadangkan.

ABSTRACT

This study was done to create a semi automatic procedure for the discrimination of three different lung diseases using chest radiograph. The statistical discrimination procedure make use of phase congruency and texture measures as features for discrimination.

Initially, a literature review was carried out which showed that phase congruency in the proposed discrimination procedure has not been attempted before. The cases studied are chest X-ray films collected from the Institute of Respiratory Medicine, Kuala Lumpur, which were digitized into DICOM format before extracting the relevant imaging data.

This study continues in three independent parts. Firstly, the region of infection (ROI) for all four cases including normal lung (NL), lung cancer (LC), lobar pneumonia (PNEU) and pulmonary tuberculosis (PTB) was detected in a novel application of statistical moments. Secondly, the ROI in the original pixel form were transformed to the corresponding phase congruency value. The ability of phase congruency as a feature for discrimination was then investigated. The texture measures of phase congruency values that were shown to have univariate normal distributions were used as a global feature for discrimination.

The final choice of features for discrimination was decided after a Receiver Operating Characteristics (ROC) analysis. Energy, contrast and homogeneity were shown to be suitable candidate for feature vectors.

Consequently, the semi automatic procedure to find the ROI and the corresponding discrimination procedure are combined to develop a prototype computer aided diagnosis (CAD) system. The construction of this CAD system will allow the methods and procedures in this study to be verified by the radiologists and medical practitioner.

ACKNOWLEGMENTS

First, I would like to express my deepest gratitude and appreciation to my supervisor Associate Professor Dr. Omar Bin Mohd Rijal and my co-supervisor Associate Professor Dr. Norliza Binti Mohd Noor who have provided valuable guidance and encouragement during the term of my study.

My many thanks to the Institute of Mathematical Sciences (ISM) for their co-operating.

Also I wish to acknowledge Dr. Ashari from Institute of Respiratory Medicine-Kuala Lumpur for his contributions.

This work is devoted to my mother and lovely wife for her kind patience during all these years. Last and not least to the support from my friend Professor Dr. Saad Al-Jassabi for his substantial advice and support through the period of my study.

Finally I am grateful for the financial support from IPPP under project number PS013-2011A.

TABLE OF CONTENTS

LIST OF FIGURES

LIST OF TABLES

CHAPTER 1

INTRODUCTION

1.1 Introduction

Failure to detect infectious lung diseases result in serious consequences to the individual as well as to the nation. The chance of recovering is higher and treatment cost is lower when a disease is detected in the early stages (Schilham, Van Ginneken & Loog, 2006). To eradicate an epidemic disease having the knowledge about its nature, the cause of disease, diagnosing techniques and methods of treatments becomes the focus of many studies (Clark, 1981; Krech, Davis, Walsh & Curtis, 1992; Crofton, Horne & Miller, 1992; Karetzky, Cunha & Brandstetter, 1993; Frieden, 2004).

Physical signs and symptoms as well as many possible pathological and radiological tests may assist medical officers to diagnose lung diseases. The results of a pathological test may take a certain period of time before being available for use. As such the chest X-ray images provide the most likely indicator of the presence of a disease. For example in the pulmonary tuberculosis (PTB) detection problem, because the sputum test takes several days before completion therefore the medical officers may have to depend on visually detecting abnormalities in the chest X-ray images. The latter problem is made even more difficult if the patient has more than one lung disease such as lobar pneumonia (PNEU) and lung cancer (LC).

Although there are some accurate radiological imaging techniques such as CT-scan and MRI, cost considerations result in the chest X-ray images being widely used in medical institutions despite its shortcomings (Schilham et al., 2006).

Lung cancer is one of the causes of cancer death worldwide (Jemal et al., 2008). Despite efforts to control lung cancer, the chance of survival from this disease is still low (5-10% in five years). Annually 1.52 million new cases of lung cancer are detected and more than 1.31 million deaths are reported (Boyle & Levin, 2008). Lung cancer in early stages does not have clear signs and symptoms, however, continued coughing, shortness of breath, chest pains, wheezing and coughing of blood are common indicators (Krech et al., 1992).

Pneumonia is a serious infection of the lungs and may have over 30 different causes. Symptoms of pneumonia include fever, coughing, shortness of breath, chest pain and loss of appetite (Karetzky et al., 1993). Over fifty five thousand people died of pneumonia in the United States of America in the year 2006 (*State of Lung Disease in Diverse Communities*, 2010). Pneumonia is the ninth leading cause of death in 2010, with the highest mortality rate of all infectious diseases especially for people over 65 years of age (Murphy, Xu & Kochanek, 2012).

Despite the availability of highly efficacious treatment for decades, pulmonary tuberculosis (PTB) remains a major global health problem. In 2010, there were over eight million cases and more than one million deaths. Socioeconomic consequences may be severe, for example 66% of people with tuberculosis are in the economically productive age group of 15–59 years and the majority of incidences occur in the developing countries (*Global tuberculosis control*, 2011).

Current methods or algorithms for disease detection mainly focus on the discrimination between normal images and images with signs of disease involving chest radiograph. A large range of imaging methods may be applied which makes use of wavelets (Oliveira, Ribeiro, de Oliveira, Coelho & Andrade, 2008; Noor, Rijal, Yunus & AbuBakar, 2010; Noor, Yunus, AbuBakar, Hussin & Rijal, 2011), textures (Ginneken, Katsuragawa, HaarRomeny, Doi & Viergever, 2002; Arzhaeva, Tax & Ginneken, 2009; Noor, Rijal, Yunus & AbuBakar, 2010), contrast enhancement (Katsuragawa & Doi, 2007), computing tomography (Arzhaeva et al., 2007), histogram information (Sklansky & Petkovic, 1984; Giger, Ahn, Doi, MacMahon, & Metz, 1990), filter outputs (Keserci & Yoshida, 2002) and descriptions of candidate shape (Sankar & Sklansky, 1982; Carreira, Cabello, Penedo, & Mosquera, 1998; Li, Katsuragawa & Doi, 2001). Imaging methods that are successful in handling the disease-absent and disease-present discrimination problem may be improved or modified for the problem of discriminating two diseases.

This thesis is a continuation of current studies and creates a semi automatic statistical discrimination procedure that may be used for developing a Computer Aided Diagnosis (CAD) system. Good discrimination results for the disease-absent and disease-present problems motivate us to develop the CAD system for discriminating between two different types of lung diseases.

The central theme in this study is the search for a new feature for discriminating two lung diseases that appear to be similar on the chest X-ray images. In particular phase congruency and texture measures will be investigated in appropriate statistical discrimination procedures.

A brief Receiver Operating Charachteristic (ROC) analysis will also be carried out to make the final choice of features before the development of a semi automatic CAD system.

1.2 Statement of the Problem

Discrimination of the three diseases lung cancer (LC), lobar pneumonia (PNEU) and pulmonary tuberculosis (PTB) from visual interpretations of chest X-ray images can usually be done by the very experienced medical practitioner. There is always the possibility that a disease such as LC may not be detected in its early stages. The problem is more so if two different types of diseases has to be differentiated. Therefore a consistent and objective procedure of detection is needed.

This study is essentially a discrimination problem for similar populations with features derived from digital images of the chest X-ray. In particular the pair wise discrimination of normal lung (NL) and LC, NL and PNEU, NL and PTB, LC and PNEU, LC and PTB and PNEU and PTB will be investigated.

1.3 Objective of Study

The first objective is to find appropriate features for discrimination using phase congruency and texture measures which will then be used in an optimal discrimination procedure. Another objective is to develop a simple procedure of detecting the region of infection (ROI). The combination of the procedure to find the ROI and the optimal discrimination procedure allows the development of a semi automatic method for discriminating NL, LC, PNEU and PTB. The final objective of developing a CAD system may then be developed if sufficient data is available.

1.4 Research Methodology

X-ray images of NL, LC, PNEU and PTB from the Institute of Respiratory Medicine (IPR), Kuala Lumpur, were collected, digitized into DICOM format and added to an existing database currently used in a related study.

For each image the ROI was detected in a statistical procedure using geometric moments. The original image was converted to a binary image where white pixels represent the lungs and black pixels represent the non-lung area. Appropriate ratios of the number of white pixels on the right lung to that of the left lung gave an indication of the ROI.

Once the ROI was obtained the original pixels values were converted to phase congruency value (PC(x)). Summary statistics of PC(x), line profiles and two-dimensional profile of PC(x) were investigated before deciding the suitable feature for discriminating NL, LC, PNEU and PTB.

Since the ROI shows no obvious shape, size and configuration, texture measures of PC(x) were studied as a possible feature. Texture measures provide global information (over a subset of the whole image) and this property may overcome the problem that the ROI has no obvious shape, size and configuration.

The texture measures were tested for normality. The existence of the normal distribution will provide an optimal discriminant function in the form of the linear discriminant function (LDF) and the quadratic discriminant function (QDF).

The use of LDF and QDF assumes knowledge of a prior probabilities and misclassification costs. In practice these parameters are un-known and assume to be equal. As such a Receiver Operating Characteristics (ROC) analysis was carried out where texture measures were selected for all possible values of the a prior probabilities and misclassification costs.

Finally the procedure to obtain the ROI and the discrimination procedure were combined to form a semi-automatic detection procedure for NL, LC, PNEU and PTB to develop a prototype CAD system.

1.5 Outline of Dissertation

The dissertation is organized into eight chapters. A general introduction about the study is given in Chapter 1 which includes statement of problem, objective of study followed by research methodology. To understand the medical nature of the project a brief literature review about lung cancer, pneumonia and tuberculosis was carried out in Chapter 2. This is followed by a literature review on general digital image analysis with emphasis on statistical moments, phase congruency model and texture measures. Chapter 2 ends with a final review on statistical discriminant analysis.

Chapter 3 is a simulation study for discrimination analysis when features for two populations are similar. The performance of the LDF and QDF were investigated for two multivariate normal distributions. The second part of Chapter 3 is another simulation study where the parameters of the phase congruency model were investigated. The final choice of phase congruency parameters was made when the images (in PC(x)) showed the ribs and ROI clearly.

A description of the data is given in Chapter 4. Chapter 5 shows the method of obtaining the ROI.

Chapter 6 begins with the investigation of the suitability of PC(x) as a feature for discrimination. Summary statistics, line profiles and texture measures of PC(x) were studied. Chapter 6 ends with developing the required discrimination procedure using texture measures of PC(x) and an ROC analysis. The prototype CAD system with combination of the procedure to find the ROI and the procedure to discriminate lung diseases are given in Chapter 7. The thesis will be concluded by Chapter 8.

CHAPTER 2

LITERATURE REVIEW

2.1 Literature Review on Lung Diseases

This Study focus on three different lung diseases namely, lung cancer (LC), lobar pneumonia (PNEU) and pulmonary tuberculosis (PTB). These three lung diseases caused millions of death all over the world. A brief review of these lung diseases is given in this section.

2.1.1 Lung Cancer

In the early twentieth century lung cancer was a rare disease. Due to smoking tobacco and air pollution the number of new lung cancer cases has increased rapidly. Lung cancer is the most frequent cause of cancer death worldwide (Jemal et al., 2008). Despite many efforts to control lung cancer, the chance of survival is still low (5-10% at five years). A survey study in the year 2008, estimates yearly more than 1,350,000 new lung cancer cases and more than 1,180,000 deaths (Boyle & Levin, 2008).

Figure 2.1 shows the rate of lung cancer with respect to gender between 1973-2006 in the United States.

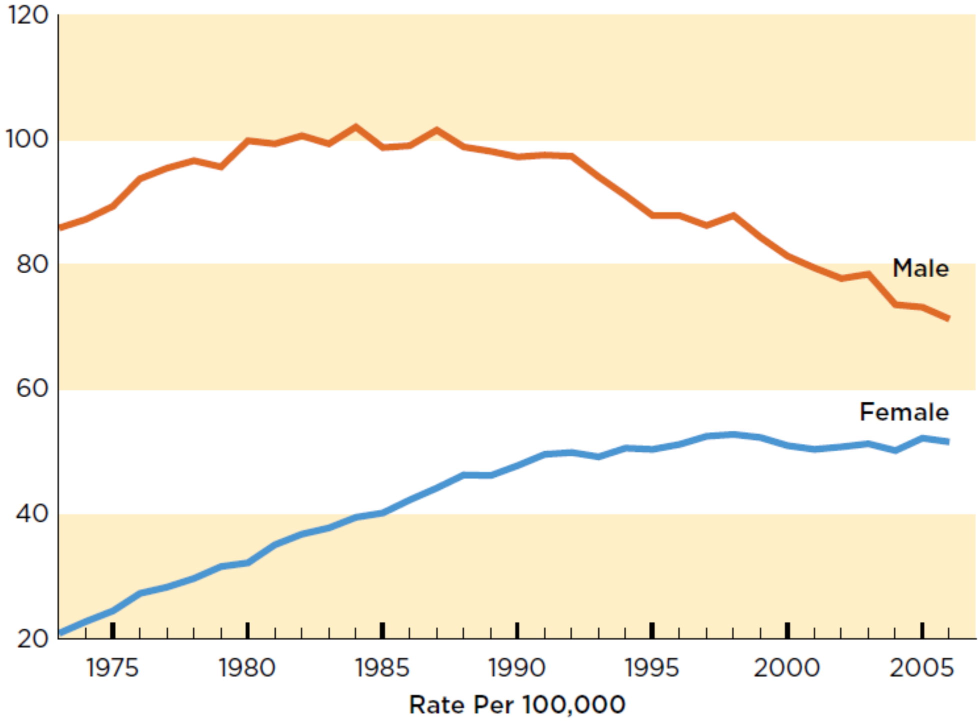

Figure 2.1: Lung cancer age-adjusted incidence rates by sex, 1973-2006.
Source: State of Lung Disease in Diverse Communities 2010.

Due to tobacco consumption, incidence of lung cancer in males is 2.5 times more than females. Highest rates have been recorded in Eastern and Central European countries. In United States of America incidence of lung cancer in black males is much more than white males. In China even though smoking is not prevalent among females, lung cancer among females is higher than males (Curado & Cáncer, 2008).

When a group of abnormal lung cells grow rapidly a patient is diagnosed with lung cancer. Abnormal cells develop and grow up faster than normal cells. Lumps of cancer cells are called tumors. Lung cancer cells may enter the blood and spread out to other organs (*State of Lung Disease in Diverse Communities*, 2010).

Lung cancer may caused by tobaccos, second hand smoke, radon, benzene, diesel air pollution, formaldehyde and asbestos (*State of Lung Disease in Diverse Communities*, 2010).

Lung cancer is categorized into two major groups called non-small cell lung cancer (NSCLC) and small cell lung cancer (SCLC). Eighty five percent of lung cancers are categorized in NSCLC category. Fourteen percent are in SCLC and only one percent have characteristics of both NSCLC and SCLC, so-called mixed small cell/large cell carcinoma. SCLC, which is known as oat cell cancer, grows and spread to other organs much more faster than NSCLC. SCLC often attacks the bronchi in the middle zone. Unfortunately, only six percent of patients having SCLC survive for more than five years.

NSCLC is classified into three sub-categories, namely, squamous cell carcinoma, adenocarcinoma, and large cell carcinoma. The chance of survival for more than 5 years for a patient who has NSCLC is less than eighteen percent. (Johnson, Blot, & Carbone, 2008).

Continues coughing, shortness in breath, pain in the chest, wheezing and bloody coughing are symptoms of lung cancer. Lung cancer can sometimes occur together with pneumonia and bronchitis (Krech et al., 1992).

Lung cancer in early stages does not have clear signs and symptoms. Lung cancer often is diagnosed in advanced stages since current techniques are still not able to detect lung cancer in early stages (Aberle et al., 2011).

Although some clinical tests are developed to diagnose lung cancers, there is no accepted technique for screening lung cancer in early stages (Schiller, Parles, & Cipau, 2009). Sputum cytology, needle biopsy and bronchoscopy are some routine clinical and pathological tests to detect lung cancer cases (Barbara, Carr, Lee, & Harman, 1998). However, chest radiograph is still widely used for detection of lung cancer since a tumor as small as half inch in diameter can be captured with X-ray (Barbara et al., 1998). An example of chest X-ray for lung cancer is showing in Figure 2.2.

Recently some hope has been found by researchers to predict lung cancer using oral examination (Xiong, Man, Wang, & Jing, 2010).

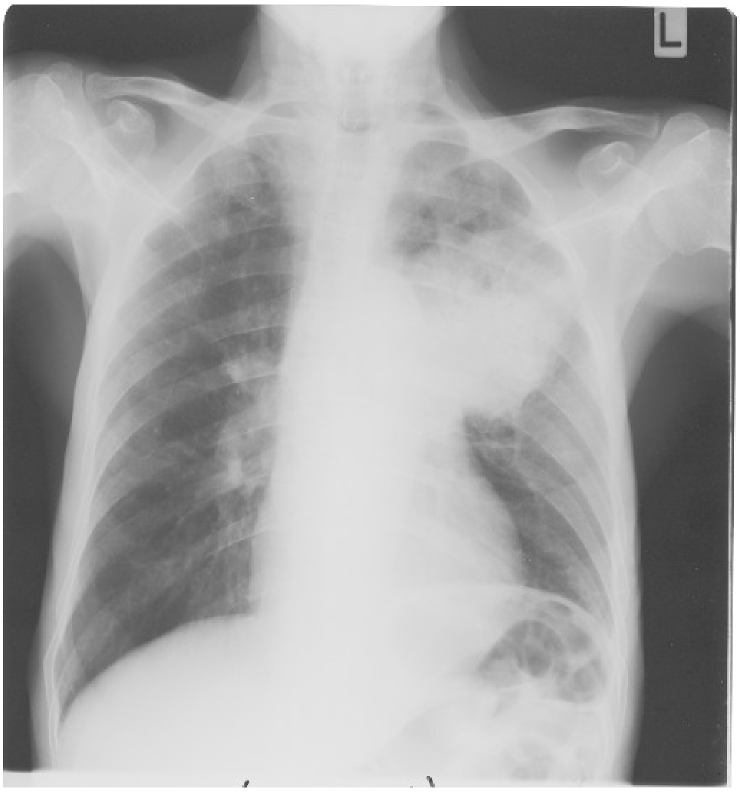

Figure 2.2: Lung cancer on left middle zone.
Source: Institute of Respiratory Medicine, Kuala Lumpur.

2.1.2 Lobar Pneumonia

Pneumonia is a serious infection and is a leading cause of death worldwide. Pneumonia is caused by more than 30 different agents. Bacteria, viruses, fungi and mycoplasmas are examples of those agents. Viruses are main cause of pneumonia in infants and young children. Although half of Pneumonia cases caused by viruses, pneumonia caused by bacteria is severe compare to other agents (*State of Lung Disease in Diverse Communities*, 2010).

Pneumonia is classified into two anatomic categories, namely, lobar pneumonia (PNEU) which infects a large area of the lobe of a lung and bronchopneumonia which is the acute inflammation of the bronchioles (Karetzky et al., 1993). Figure 2.3 illustrates the normal lung and lobar pneumonia.

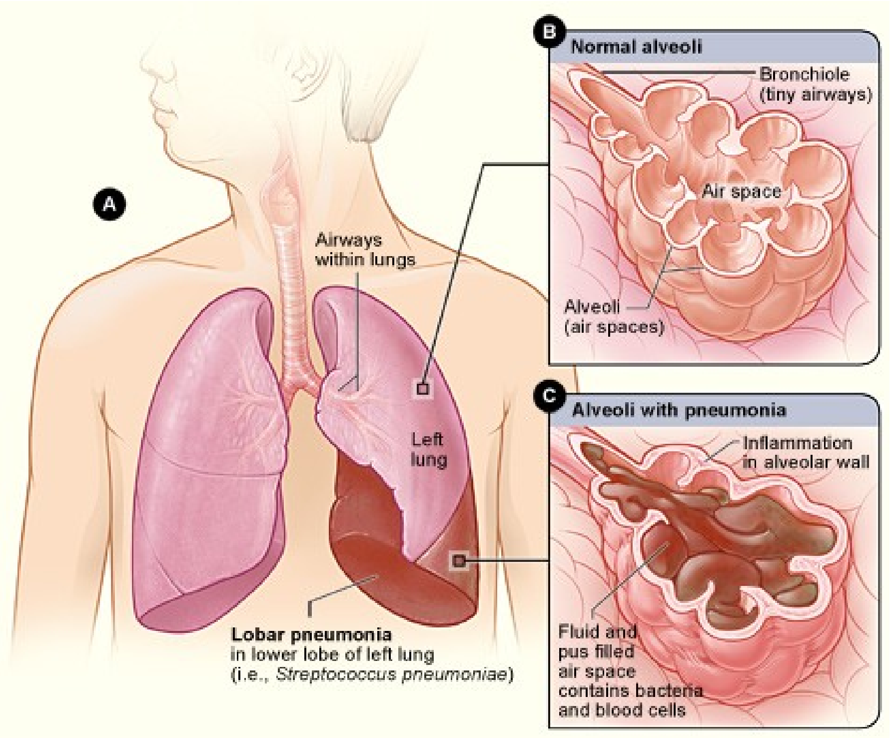

Figure 2.3: Lobar pneumonia. Sacs in left lower zone are filled by pus and fluid.
Source: National Heart, Lung and Blood Institute, USA.

Different agents develops different signs and symptoms of pneumonia, however, the symptoms of pneumonia in initial stages are very similar to influenza. Fever, cough with sputum, chest pain and shortness of breathing are some symptoms of pneumonia. Symptoms of pneumonia caused by bacteria are red-brown, green or yellow sputum and high fever in degree. Loss of appetite, tin and whitish sputum are signs of pneumonia caused by either mycoplasmas or viruses. There are other symptoms that implies pneumonia are shivering, chills, headache, delirium, muscle pain, weakness and blue lips and nail (Karetzky et al., 1993). Once Pneumonia affects a lung, the air sacs fills with pus, this fact then cause lower volumes of oxygen. Oxygen deficiency will make the body's cells vulnerable. With the nature of this weakness, the infection may be spread throughout the body (Karetzky et al., 1993).

Mortality rate of pneumonia is still high. In the year 2006, over 12 million pneumonia cases were recorded worldwide which is nearly 41.3 cases per 10,000 people (DeFrances, Lucas, Buie, & Golosinskiy, 2008). In the United States of America pneumonia killed 55,477 people in 2006 (*State of Lung Disease in Diverse Communities*, 2010). The United States of America's government spent $40.2 billion, to control, prevention and treatment of pneumonia in the year 2005 (*National Heart, Lung and Blood Institute*, 2007).

Smokers and people whose have a weak immune system are at high risk for pneumonia. In particular, infants, young children and people over 65 years of age are at high risk. Some diseases those impair immune system such as diabetes, cardiovascular disease and AIDS may help to develop pneumonia (Murphy et al., 2012). If pulmonary tuberculosis is not treated in a timely manner, the tubercle bacillus (mycobacterium tuberculosis) may also cause pneumonia (Harries, Maher, & Graham, 2004).

Once a pneumonia case is suspected, further investigations such as chest X-ray is usually ordered to confirm the diagnosis. A chest X-ray is ordered immediately since X-ray is a painless and fast test. In a chest X-ray the infected region by pneumonia seen as a cloudy area. However further clinical tests such as blood test and sputum culture are required for a definitive diagnosis of the type of pneumonia (Wipf et al., 1999). An example of lobar pneumonia is shown by Figure 2.4.

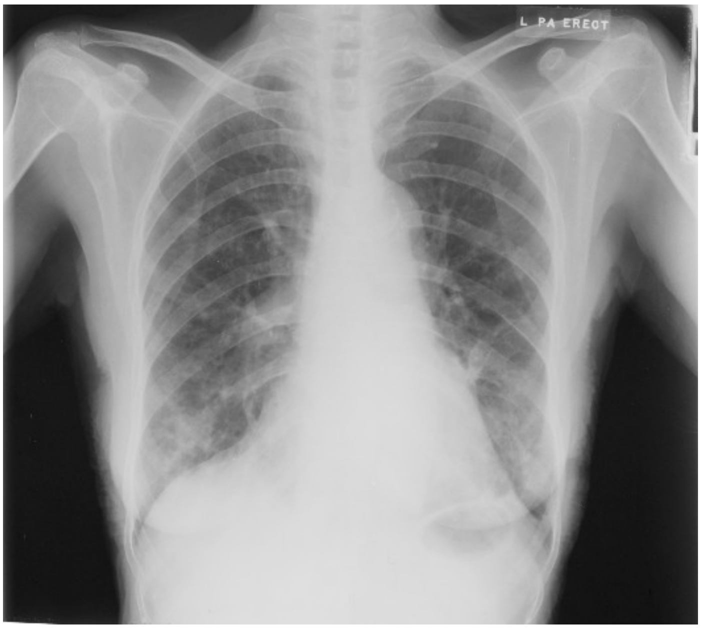

Figure 2.4: Lobar pneumonia both lower left and right zones.
Source: Institute of Respiratory Medicine, Kuala Lumpur.

2.1.3 Pulmonary Tuberculosis

Despite many effective treatment and prevention procedures, tuberculosis is still a global health problem especially in Asia and Africa with 59 and 26 percent of worldwide recorded cases respectively. After HIV, tuberculosis is the second cause of infectious death worldwide. In the year 2010, over 8.5 million tuberculosis cases with over 1.2 million deaths were recorded. Socioeconomic consequences may be severe, for example 66 percent of people with tuberculosis are in the economically productive age of 15-59 years and the majority of incidences occur in developing countries (*Global tuberculosis control*, 2011). Figure 2.5 illustrates the global tuberculosis incidence rate in the year 2003.

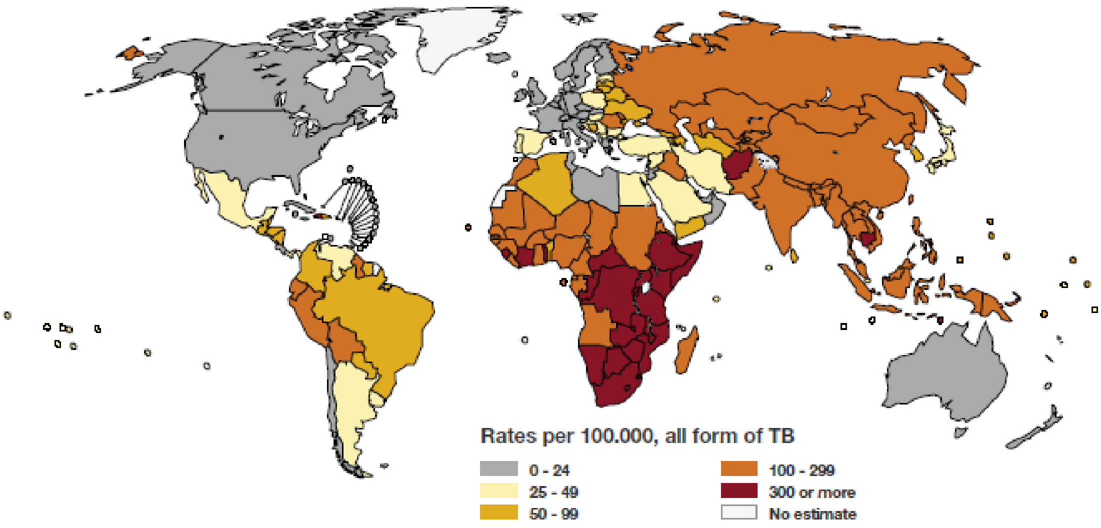

Figure 2.5: Tuberculosis incidence in the world.
Source: WHO: The global plan to stop TB 2006-2015.

Although tuberculosis is classified into four major categories, mycobacterium tuberculosis, rod-shape aerobic bacterium, is the most common type of tuberculosis (Frieden, 2004). Regardless of the type of bacilli, tuberculosis is categorized into three categories, namely, pulmonary tuberculosis (PTB), extra pulmonary tuberculosis (EPTB) and tuberculosis in children (TC). Pulmonary tuberculosis includes lung tuberculosis, tuberculous pleural effusion, empyema and miliary tuberculosis (Rieder, Yuan, Gie, & D.A, 2009).

PTB is a highly infectious disease that can be transmitted easily. Millions of people may potentially carry the tuberculosis bacilli for a long term. An active bacteria occurs in only ten percent of carrying cases.

PTB is highly contagious and can spread rapidly if people do not observe the personal hygiene. The chance of PTB transmission indoors without ventilation is very high since sunlight quickly kills mycobacterium tuberculosis and ventilation absorb them. Once an infected person coughs or sneezes, approximately 3,000 droplets containing the bacilli spreads. These bacilli are an aerobic bacterium and may survive for several hours. Once the bacilli is inhaled, those germs enter into the respiratory system. The bacilli breathed in stick to the upper lobes and proliferate rapidly (Harries et al., 2004).

Fever in the evening, night sweats, loss of weight, loss of appetite, fatigue, muscle weakness, cough with sputum production (sometimes with blood), shortness of breath and chest pain are some signs and symptoms of tuberculosis (*Background information about tuberculosis*, 2007).

The chance of recovering is high if the PTB is diagnosed in early stages. Although, the best way to diagnose a PTB is to culture the patient's sputum three times and perform microscopic pathological test, the use of chest radiograph is advised to provide more information on disease status. PTB is clearly detected using chest radiograph when the abnormality can be seen as patchy or nodular shadows in the upper zones, possibly with cavitations (Rieder et al., 2009). An Example of chest X-ray for a confirmed pulmonary tuberculosis is shown in Figure 2.6.

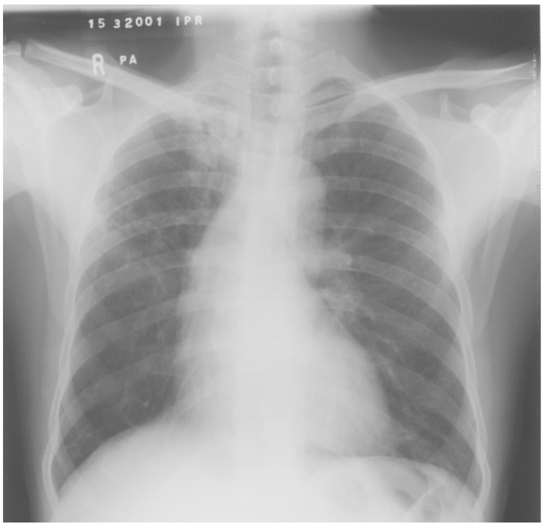

Figure 2.6: Pulmonary tuberculosis on right upper zone.
Source: Institute of Respiratory Medicine, Kuala Lumpur.

2.2 Literature Review on Chest Radiography

In the electromagnetic radiation spectrum, X-rays have a short wavelength with the range of $[0.01\times10^{-9}, 10\times10^{-9}]$ meter, frequency in the range of $[3\times10^{16}, 3\times10^{19}]$ Hertz and energy in the range of $[100, 100\times10^{3}]$ electron-volts.

Figure 2.7 shows the electromagnetic radiation spectrums. X-rays are usually classified into two major groups, namely, hard X-rays and soft X-rays. Hard X-rays have a wavelength in the range of $[0.01\times10^{-9}, 0.10\times10^{-9}]$ meter and soft X-rays have a wavelength in the range of $[0.10\times10^{-9}, 10.0\times10^{-9}]$ meter.

Hard X-rays are widely used in many applications, for example, interior monitoring and object detection such as luggage security control in airports, quality control in industries (Someda, 2006).

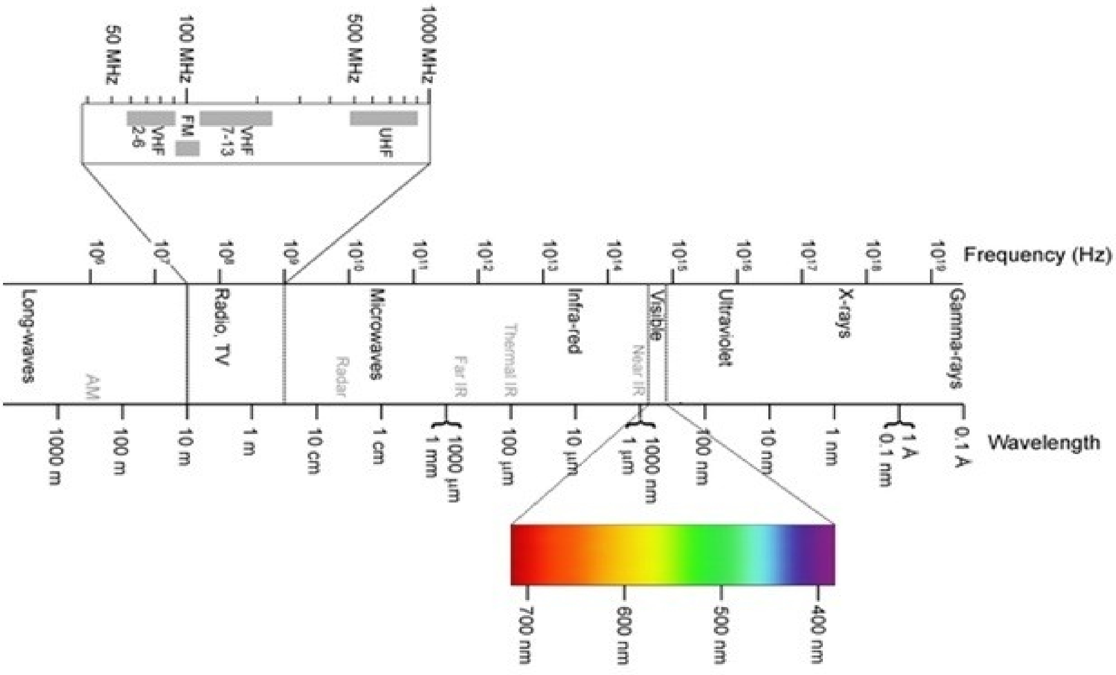

Figure 2.7: Electromagnetic radiation spectrum.

2.2.1 The Use of X-ray in Clinical Radiography

Hard X-rays are widely used in medical institution to monitoring inside the body. Heart and other organs, rib-bones and some lung abnormalities such as tumor cells can be seen clearly in chest X-ray film (Corne, Carroll, Delany, & Moxham, 2002).

The first systematic studies on observing and effects of X-rays is attributed to Wilhelm Rontgen (Rontgen, 1895).

Figure 2.8: The first X-ray image taken by Wilhelm Rontgen in 1895.

The mechanism of imaging with X-ray tube is different with the optical cameras. In optical camera the image is raised on negative film with reflecting light beams from the object, but in X-ray imaging, the X radiations are emitted to an object then X-rays penetrate the softer parts and blocked by more dense parts. The X-ray radiograph finally will be appeared on the film depending on radiation flux. Figure 2.9 illustrates the mechanism of ordinary camera and X-ray camera (McClelland, 2004).

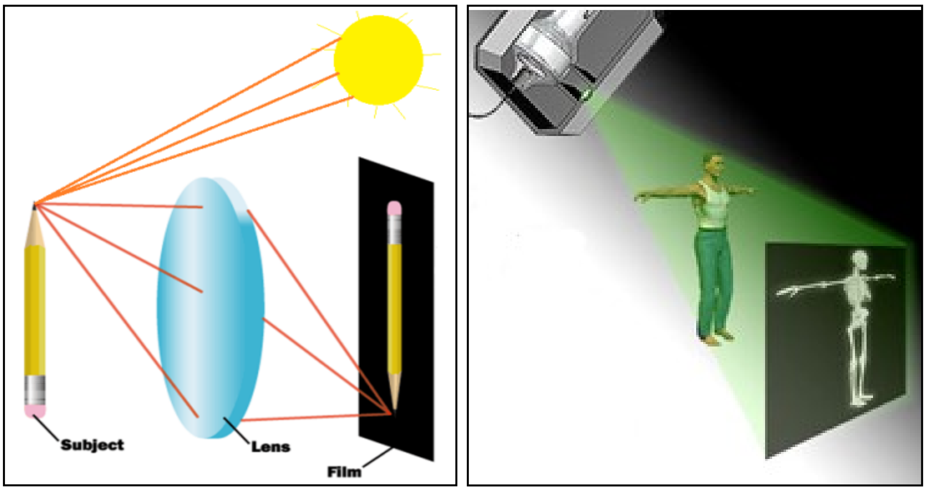

(a) (b)

Figure 2.9: Mechanism of (a) ordinary camera and (b) X-ray radiograph.

X-ray imaging was involved in medical and surgical services in 1896 when John Hall-Edwards captured a needle in the hand of a patient (Frame, 2010). However problems arise with the use of X-rays where studies have shown that the accuracy of the X-ray interpretation is subject to varying degrees of observer error (Frieden, 2004; Nakamura, Ohmi, Kurihara, Suzuki, & Tadera, 1970). Digital X-ray images involved in current studies to detect disease mainly focus on the discrimination between normal images and images with signs of disease; for example, the use of wavelets for detection and discrimination of pneumonia (Noor, Rijal, Yunus, & AbuBakar, 2010) and tuberculosis (Noor, Rijal, Yunus, Mahayiddin, et al., 2010; Noor et al., 2011), texture analysis for detection of abnormality (Arzhaeva et al., 2009; Ginneken et al., 2002) andThe use of contrast enhancement in computer aided diagnosis (Katsuragawa & Doi, 2007). It should be noted that being exposed to radiation with a single high dose or even small exposures within short period damages living cells, tissue and organs. X-ray radiation may even damage DNA, and cause rapidly dividing skin cells, hair follicles that may caused premature aging and growth of cancer cells (Hargreaves & Moridi, 2010). However, X-ray radiography is still widely used in many clinical situations due to economic consideration and affordable facilities.

2.2.2 Region of Infection on Chest X-ray

In medical sciences, a chest X-ray is usually divided into six zones namely, right-upper zone (RU), right-middle zone (RM), right-lower zone (RL), left-upper zone (LU), left-middle zone (LM) and left-lower zone (LL). The infected zone or the zone that we are studying is so called the Region Of Interest (ROI). The six zones on a chest radiograph are shown in Figure 2.10.

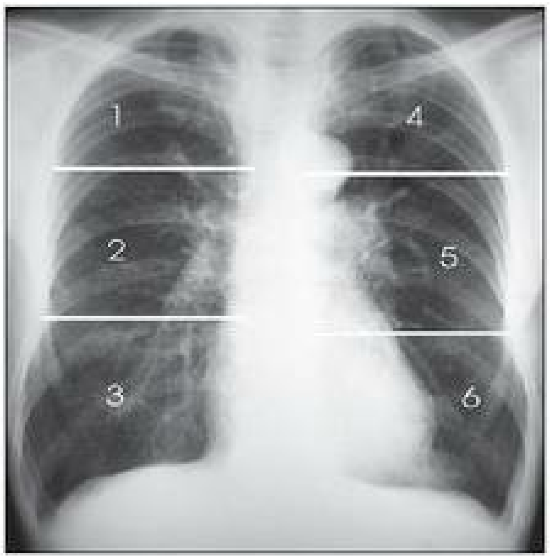

Figure 2.10: Six zones of a chest radiograph are RU(1), RM(2), RL(3), LU(4), LM(5) and LL(6).

2.3 Digital Image

In digital imaging, an image is made of the smallest physical addressable elements called pixel. The size of a digital image is determined by arrangement of pixels in width (number of columns) and height (rows). Therefore, a simple digital image mathematically, can be considered to be a two dimensional function (matrix) where for a pixel located at spatial coordinate (x,y) the value of $f(x,y)$ given by the light-intensity with the range of 0 to 255. Unlike in mathematics, in the imaging applications, the origin for a digital image is in the left top corner. Axis x is increasing from top to bottom and *y* is increasing from left to right. The only historical reason that may explain why the reference coordinate system in a digital image is not according to mathematical convention is that digital image were defined in terms of the electron beam scanning pattern of televisions and the beam scanned left to right and top to bottom. The position of *x* and *y* axis is shown in Figure 2.11.

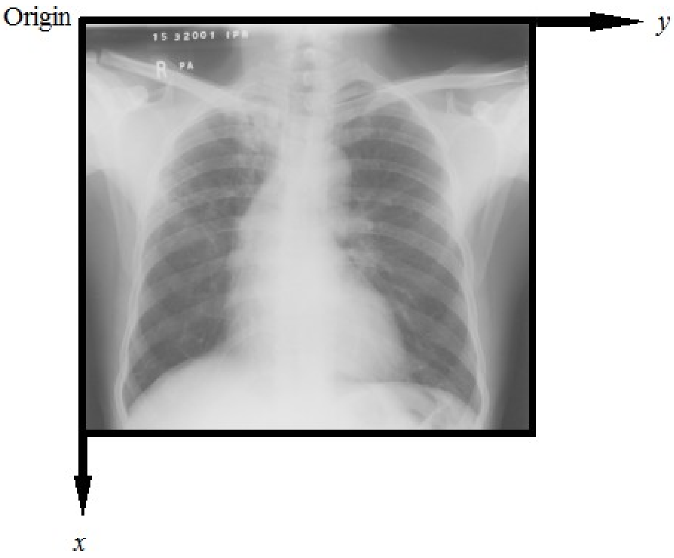

Figure 2.11: Illustration the origin of axis for a digital image.

The value of *f* is depending on the type of image, for example, for a binary image *f*(*x*,*y*) can be either 0 or 1. For a grayscale image, the pixel value can be vary from 0 to 255 when each pixel is represented by eight bits. A 12-bit image has pixel values in range 0 - 4095 and for a 16-bits image, the pixel intensity is varies from 0 to 65535. The number of bits required to store a grayscale image is obtained by $N \times M \times m$ where N and M obtain image size (number of rows and columns respectively) and *m* is the number of gray level for example an image of size 256 x 256 pixels with 8 gray level (one byte for each pixel) is stored in 65536 bytes. In a digitized image, the value of discrete brightness is called gray level (Gonzalez & Woods, 1992).

Mathematically, a grayscale digital image is a unique matrix including light-intensity values such as $\begin{bmatrix} f(1,1) & f(1,2) & \dots & f(1,M) \\ f(2,1) & f(2,2) & \dots & f(2,M) \\ \vdots & \vdots & \dots & \vdots \\ f(N,1) & f(N,2) & \dots & f(N,M) \end{bmatrix}$.

2.3.1 Digital Image Analysis

Digital image analysis is a set of activities that are carried out in order to extract meaningful information for a specific purpose from a given image in terms of digital image processing techniques when a computer is utilized for auto-computation. Applications of digital image analysis can be as simple as bar code reading or as complicated as image understanding and object identification.

2.3.2 Texture Measures

A texture measure is a metric which is carries global information about the arrangement of pixel intensities in a digital image. A set of texture measures is generally designed to quantify the perceived texture of an image for the purpose of image segmentation and object classification. Image texture analysis methods may be labeled into three major groups: First is texture analysis methods in terms of image intensity, the second is structured approaches (using symbolic level techniques) and the third is texture analysis in terms of statistical modelling. In structured approach an image texture is considered as a set of texture elements with a pattern in a region. Statistical approaches consider a texture as quantitative measure of pixel intensity arrangements (Tuceryan & Jain, 1993). Gray level co-occurrence matrix (GLCM) (Haralick, 1979), generalized co-occurrence matrices (GCM) (Davis, Clearman, & Aggarwal, 1981), auto-correlation function analysis (Haralick, 1979), two-dimensional filtering in the spatial and frequency domain (M. Clark, Bovik, & Geisler, 1987; Coggins & Jain, 1985; Turner, 1986; Voorhees & Poggio, 1987), and second order spatial averages (Gagalowicz & Graffigne, 1988) are some known texture analysis methods that directly involve gray levels of an image. Some approaches in symbolic texture analysis can be reviewed in Julez's researches (Julesz, 1981, 1986). Perceptual grouping and spatial frequency channels (Beck, Prazdny, & Rosenfeld, 1983; Beck, Sutter, & Ivry, 1987) are examples of symbolic level texture analysis. Examples of statistical modelling can be found as Markov random fields (MRF) (Cross & Jain, 1983; Kashyap, Chellappa, & Ahuja, 1981) and fractal based modelling (Pentland, 1984).

However, this study involves using area moments as statistical texture measures for the purpose of detection of ROI. Energy, mean energy, entropy, homogeneity, contrast, standard deviation of pixel value, standard deviation of energy and correlation are used as statistical texture measures to discriminate lung diseases.

2.4 Literature Review on Area Moments

In statistics useful information can be derived from moments or functions of moments, such as the mean, variance, skewness and kurtosis, which may describe the characteristics of distribution of a given random variable (Milton & Arnold, 2002). In terms of the moment uniqueness theorem, the distribution of random variable is uniquely defined by the set of moments.

In practice, a given image may be characterized with a set of low order (Gonzalez & Woods, 1992). In this section the definition and properties of two dimensional moments is discussed.

2.4.1 Area Moments

Two dimensions moment of order $p+q$ for a given continuous function such as $f(x,y)$ is defined by:

$$m_{pq}(f(x,y)) = \int_{-\infty}^{\infty}\int_{-\infty}^{\infty} x^p . y^q . f(x,y)\, dx\, dy \text{, where } p+q = 0,1,2,\ldots.$$

The discrete form of two-dimensional moments is defined by:

$$m_{pq}(f) = \sum_{i=1}^{N}\sum_{j=1}^{M} x_i^{\ p} . y_j^{\ q} . f(x_i, y_j).$$

Let I be an image of size $N \times M$ where $I(x,y)$ denotes the pixel intensity, the area moment of order $p+q$ is given by:

$$m_{pq}(I) = \sum_{x=0}^{N-1}\sum_{y=0}^{M-1} x^p . y^q . I(x,y) \qquad (2.1)$$

The use of two-dimensional moments for pattern recognition was motivated by (Hu, 1962).

2.4.2 Moments Uniqueness Theorem

Let $f(x,y)$ be piecewise continuous and has nonzero values only in a finite region on the (x,y) plane, then the moments of all orders exist and the set of moments $\{m_{pq}\}$ is uniquely determined by $f(x,y)$. Conversely $f(x,y)$ is uniquely determined by its moments (Hu, 1962):

$$f(x,y)=\int_{-\infty}^{\infty}\int_{-\infty}^{\infty}\exp\left[-j2\pi(ux+vy)\right]\left[\sum_{p=0}^{\infty}\sum_{q=0}^{\infty}m_{pq}\frac{(j2\pi)^{p+q}}{p!q!}u^{p}v^{q}\right]du\,dv\,.$$

2.4.3 Properties of Area Moments

For a given region, *I*, the area moment with low orders (small value for *p* and *q*) can be interpreted geometrically. Explanation and illustration of area moments for complicated images is difficult, however, properties of each moment can be studied with simple images.

2.4.3.1 Moment of Order Zero

Moment of order zero ($p = q = 0$) is defined by

$$m_{00}(I)=\sum_{x=0}^{N-1}\sum_{y=0}^{M-1}x^{0}.\,y^{0}.\,I(x,y)=\sum_{x=0}^{N-1}\sum_{y=0}^{M-1}I(x,y)\cdot$$

Moment of order zero can be considered as total mass of the given image *I* and represents the total object area. For an image where "black" is given intensity value zero and "white" the value 255, therefore $m_{00}(I)$ is zero for a black-image and a very large value for a white-image. In fact $m_{00}(I)$ is an indicator of the texture measure energy.

2.4.3.2 Moment of Order One

There are two moments of order one since $p+q=1\Rightarrow\begin{cases}p=1,q=0\\p=0,q=1\end{cases}$, thus

$$m_{10}(I)=\sum_{x=0}^{N-1}\sum_{y=0}^{M-1}x^{1}.\,y^{0}.\,I(x,y)=\sum_{x=0}^{N-1}\sum_{y=0}^{M-1}x\,.\,I(x,y),$$

and

$$m_{01}(I)=\sum_{x=0}^{N-1}\sum_{y=0}^{M-1}x^0 . y^1 . I(x,y)=\sum_{x=0}^{N-1}\sum_{y=0}^{M-1}y . I(x,y).$$

The moments of order one are used to obtain the center of mass. The coordinate of the center of mass is located on the intersection of two lines $x=\bar{x}$ and $y=\bar{y}$ where $\bar{x}=\frac{m_{10}}{m_{00}}$ and $\bar{y}=\frac{m_{01}}{m_{00}}$ (Prokop & Reeves, 1992).

Similar information is also given by the central moments (moments about centre of mass) which are calculated when the origin locates on the centre of mass. The central mass is defined by:

$$\mu_{pq}(I)=\sum_{x=0}^{N-1}\sum_{y=0}^{M-1}(x-\bar{x})^p . (y-\bar{y})^q . I(x,y). \tag{2.2}$$

Note that $\mu_{10}=\mu_{01}=0$.

2.4.3.3 Moments of Order Two

The moments of order two, often called moments of inertia, is such that when,

$$p+q=2 \Rightarrow \begin{cases} p=2, q=0 \\ p=1, q=1 \\ p=0, q=2 \end{cases}$$, therefore

$$m_{20}(I)=\sum_{x=0}^{N-1}\sum_{y=0}^{M-1}x^2 . y^0 . I(x,y)=\sum_{x=0}^{N-1}\sum_{y=0}^{M-1}x^2 . I(x,y) ,$$

$$m_{11}(I)=\sum_{x=0}^{N-1}\sum_{y=0}^{M-1}x^1 . y^1 . I(x,y)=\sum_{x=0}^{N-1}\sum_{y=0}^{M-1}x . y . I(x,y)$$ and

$$m_{02}(I)=\sum_{x=0}^{N-1}\sum_{y=0}^{M-1}x^0 \, . \, y^2 \, . \, I(x,y)=\sum_{x=0}^{N-1}\sum_{y=0}^{M-1}y^2 \, . \, I(x,y) \cdot$$

Several characteristics of an object can be described with the second moments such as principal axes, image ellipse and radii of gyration.

- **Principal Axes**

The major and minor principal axes of an ellipse may be described by the maximum and minimum moments of order two. The angle of the principal axis may be used as descriptor of object orientation. The orientation is calculated by

$$\phi=\frac{1}{2}\tan^{-1}\left(\frac{2\mu_{11}}{\mu_{20}-\mu_{02}}\right).$$

- **Image Ellipse**

The image ellipse is a elliptical disk with same centre of mass as original image. The intensity of image ellipse is calculate by $I=\frac{\mu_{00}}{\pi\alpha\beta}$ where semi-major axis (α) and semi-minor axis (*β*) in terms of second moments are given by:

$$\alpha=\left(\frac{2\left[\mu_{20}+\mu_{02}+\sqrt{(\mu_{20}-\mu_{02})^2+4\mu_{11}^2}\right]}{\mu_{00}}\right)^{1/2}\quad\text{and}$$

$$\beta=\left(\frac{2\left[\mu_{20}+\mu_{02}-\sqrt{(\mu_{20}-\mu_{02})^2+4\mu_{11}^2}\right]}{\mu_{00}}\right)^{1/2}.$$

- **Radii of Gyration**

In terms of second moments, the radii of gyration about x axis and y axis are calculated by

$$\rho_x = \sqrt{\frac{m_{20}}{m_{00}}} \text{ and } \rho_y = \sqrt{\frac{m_{02}}{m_{00}}} .$$

For a given axis, the radius of gyration is the distance between the axis and the line that mass in concentrated. Alternatively, the radius of gyration about the origin is calculated by $\rho_C = \sqrt{\frac{\mu_{20} + \mu_{02}}{\mu_{00}}}$.

The ρ_C is used to determine the features based on rotational invariance since it is invariant to image orientation.

2.4.3.4 Moments of Order Three

There are four moments of order, $p + q = 3 \Rightarrow \begin{cases} p = 3, q = 0 \\ p = 2, q = 1 \\ p = 1, q = 2 \\ p = 0, q = 3 \end{cases}$,and subsequently

$$m_{30}(I) = \sum_{x=0}^{N-1} \sum_{y=0}^{M-1} x^3 . y^0 . I(x, y) = \sum_{x=0}^{N-1} \sum_{y=0}^{M-1} x^3 \ . I(x, y),$$

$$m_{21}(I) = \sum_{x=0}^{N-1} \sum_{y=0}^{M-1} x^2 . y^1 . I(x, y) = \sum_{x=0}^{N-1} \sum_{y=0}^{M-1} x^2 \ .y \ . I(x, y),$$

$$m_{12}(I) = \sum_{x=0}^{N-1} \sum_{y=0}^{M-1} x^1 . y^2 . I(x, y) = \sum_{x=0}^{N-1} \sum_{y=0}^{M-1} x \ . y^2 \ . I(x, y) \text{ and}$$

$$m_{03}(I)=\sum_{x=0}^{N-1}\sum_{y=0}^{M-1}x^{0}.\,y^{3}.\,I(x,y)=\sum_{x=0}^{N-1}\sum_{y=0}^{M-1}y^{3}\,.\,I(x,y)\cdot$$

Generally, the moments of order k with forms of m_{k0} and m_{k0} are called moments of image projection on x axis and y axis respectively.

The central moments of order three are used to determine the skewness of image projections. If $\gamma_x(I)=\frac{\mu_{30}}{\mu_{20}^{3/2}}$ is positive the image projected on x axis has skewnees on left side of y axis. if it is negative the image projected on x axis has skewnees on right side of y axis and if it is equal to zero the image projected on x axis is symmetric about y axis.

Alternatively $\gamma_y(I)=\frac{\mu_{03}}{\mu_{02}^{3/2}}$ is used as indicator to measure the skewness of image projection on y axis about x axis.

2.4.3.5 Moments of Order Four

The two central moments of image projection with order four is the main factor to measure the kurtosis of image projection. The indicators for image projection on x axis and y axis respectively are $\lambda_x(I)=\frac{\mu_{40}}{\mu_{20}^{2}}-3$ and $\lambda_y(I)=\frac{\mu_{04}}{\mu_{02}^{2}}-3$.

For further information please refer to (Mukundan & Ramakrishnan, 1998) and (Prokop & Reeves, 1992).

2.4.4 Applications of Moments in Image Processing

Due to the moment uniqueness theorem and the fact that moments are easy to apply, area moments are still widely used in many subjects. Examples of using moments in image analysis can be found in image segmentation (Tuceryan, 1994) and object recognition (Barbu, Costin, & Ciobanu, 2010). Other applications of 2D moments include object detection (Rizon et al., 2006), object identification (Dudani, Breeding & McGhee, 1977), shape description (Zusne, 1965), shape discrimination (Yinan, Weijun & Yuechao, 2003), characterizing texture (Pentland, 1984) and (Tuceryan & Jain, 1990).

2.5 Literature Review on Phase Congruency

2.5.1 Introduction

Phase congruency model is a frequency based method that provides information from adjacent pixels with considering both phase and amplitude of the frequency components instead of processing spatially. This property helps to measure transition between adjacent pixels regardless of configuration illumination, blurring and magnification of image. The use of phase congruency values was motivated by Oppenhiem where phase information in signals is more important than its amplitude (Oppenheim & Lim, 1981). Local energy model was involved in terms of Fourier components to develop the use of points which are maximally in phase (Kovesi, 1991, 1993; Morrone & Burr, 1988; Morrone & Owens, 1987; Morrone, Ross, Burr & Owens, 1986; Owens, Venkatesh & Ross, 1989; Venkatesh & Owens, 1990). Phase congruency function in terms of the Fourier series expansion was presented by Morrone and Owens where Fourier components are maximally in phase at points which are correspond to human perceived edges (Morrone & Owens, 1987). It is proven that local energy is proportional to phase congruency (Venkatesh & Owens, 1989). In the year 1999, Kovesi extract some image features such as edge and boundaries using phase congruency model in terms of log-Gabor transfer function. The value of phase congruency PC(x)-value is between zero and one, value close to one (high congruency in phases) indicates large transition on adjacent pixels, or alternatively, the pixel x located on a sharp edge and value close to zero (low congruency in phases) indicates mild transition on adjacent pixels.

The properties of the phase congruency model has been used in new and interesting technique in the recent decade, for example, for image feature detection (Burlacu & Lazar, 2008), edge and corner detection (Kovesi, 2003), image splicing detection (Chen, Shi & Su, 2007) and region detection (Ahmed, Sayadi & Faniech, 2009).

The disadvantages of phase congruency model, however, are intensive computation and sensitivity to change its parameters such as noise.

2.5.2 Components of a Wave

Consider a sinusoidal wave such as $f(t) = A\cos(\omega t + \phi)$. The components of $f(t)$ are as follows:

a) Amplitude, A: magnitude of the wave length,
b) Frequency, ω: number of complete cycles per unit of time,
c) Phase shifting, ϕ.

Figure 2.12 is showing two waves with different frequencies at one second period time.

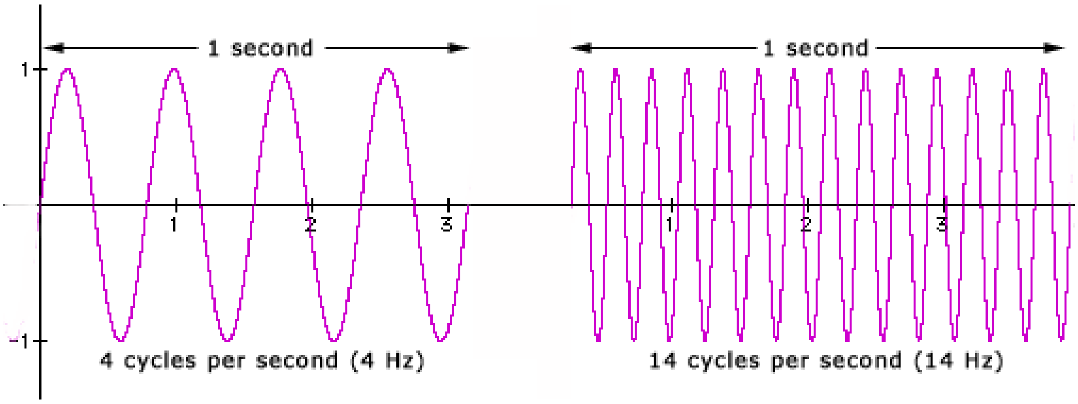

(a) (b)

Figure 2.12: Waves with (a) frequency 4Hz and (b) frequency 14Hz.

A wave stretches when the value of amplitude is increased, compresses when frequency is increased and can be shifted to the right when phase shift is positive and shifted to the left when it is negative (see Figure 2.13).

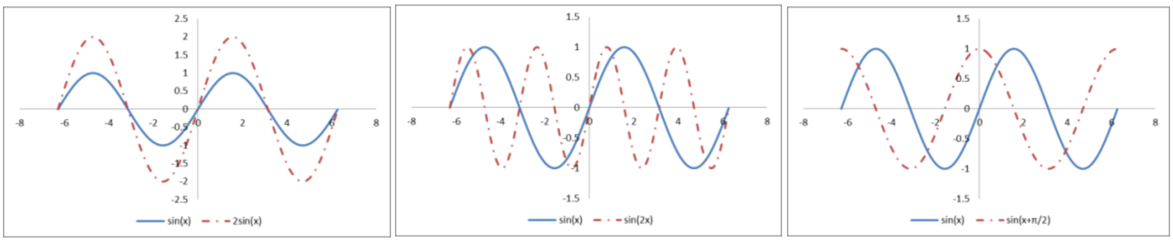

(a) (b) (c)

Figure 2.13: Effects of changing (a) amplitude , (b) frequency and (c) phase shift on the wave sin(*x*).

Phase shift is the relative displacement between or among waves with the same frequency. Phase also measures the angle of a fixed point in the cycle wave. Phase is important when a wave is studied individually or in series.

Two waves are called in-phase if the peaks and valleys occur at the same time. In other words, two waves are in-phase if they travel simultaneously.

2.5.3 Fourier Series Expansion

A given function can be decomposed into periodic functions (signals). Fourier series expansion is a reversible function. The importance of Fourier series expansion is highlighted when a complicated function can be decomposed into simple terms and can be recombined to original form.

Let $f(t)$ is a one dimensional periodic and continuous signal in the interval $[-\pi, \pi]$. $f(t)$ is decomposed in terms of Fourier series expansion by

$$f(t) = \frac{1}{2} a_0 + \sum_{n=1}^{\infty} a_n \cos(nt) + \sum_{n=1}^{\infty} b_n \sin(nt) \ ,$$

where

$$\begin{aligned} a_0 &= \frac{1}{\pi} \int_{-\pi}^{\pi} f(t)\, d(t), \\ a_n &= \frac{1}{\pi} \int_{-\pi}^{\pi} f(t) \cos(nt)\, d(t), \\ b_n &= \frac{1}{\pi} \int_{-\pi}^{\pi} f(t) \sin(nt)\, d(t). \end{aligned}$$

The signal $f(t)$ may be simplified as $f(t) = DC + \sum_{n=1}^{\infty} A_n \cos(nt + \Phi)$, where $DC = \frac{1}{2} a_0$, A_n is amplitude and Φ is phase shifted.

2.5.4 Phase Congruency Model for One Dimensional Signal

Let $f(x)$ is a one dimensional signal, phase congruency function in terms of the Fourier series expansion at some location x computed by

$$\mathrm{PC}_1(x) = \max_{\bar{\phi}\in[0,2\pi]} \frac{\sum_n A_n \cos\left(\phi_n(x) - \bar{\phi}(x)\right)}{\sum_n A_n}, \tag{2.3}$$

where A_n represents the amplitude of the n^{th} Fourier component, and $\phi_n(x)$ represents the local phase of the Fourier component at position *x*. The value $\bar{\phi}(x)$ that maximizes Equation 2.3 is the amplitude weighted mean local phase angle of all the Fourier terms at the point being considered (Kovesi, 1999).

In terms of Taylor series expansion, the value of $\cos\left(\phi_n(x) - \bar{\phi}(x)\right)$ can be estimated by $\cos\left(\phi_n(x) - \bar{\phi}(x)\right) \approx 1 - \frac{\left(\phi_n(x) - \bar{\phi}(x)\right)^2}{2}$. Therefore to maximize the value of $\mathrm{PC}_1(x)$, we need to minimize the difference between local angles of amplitudes and the angle of weighted mean amplitude (minimize the $\left(\phi_n(x) - \bar{\phi}(x)\right)$).

Calculating the $\mathrm{PC}_1(x)$ from definition is computationally difficult. In the year 1981, Venkatesh and Ownes showed that point of maximum phase congruency can be calculated equivalently by searching for peaks in the local energy function. The local energy function is defined one dimensional luminance profile *I*(*x*) as

$$E(x) = \sqrt{F^2(x) + H^2(x)} \ ,$$

where *F*(*x*) is the signal *I*(*x*) with its DC component removed and *H*(*x*) is the $\frac{\pi}{2}$ phase shift of *F*(*x*). Note that DC is the constant part of a wave which is independent of function variable *x*. In the other words DC is the vertical offset on the signal. For a given wave such as $f(x) = A + B\sin(\omega x + \phi)$, *A* is the DC component.

Local energy at position *x* is calculated based on phase congruency that scaled by the sum of the Fourier amplitudes as:

$$E(x) = \mathrm{PC}_1(x)\sum_n A_n$$

Peaks in local energy will correspond to peaks in phase congruency since local energy is directly proportional to the phase congruency function.

The relationship between phase congruency, energy and the sum of the Fourier amplitudes can be seen geometrically in Figure 2.14.

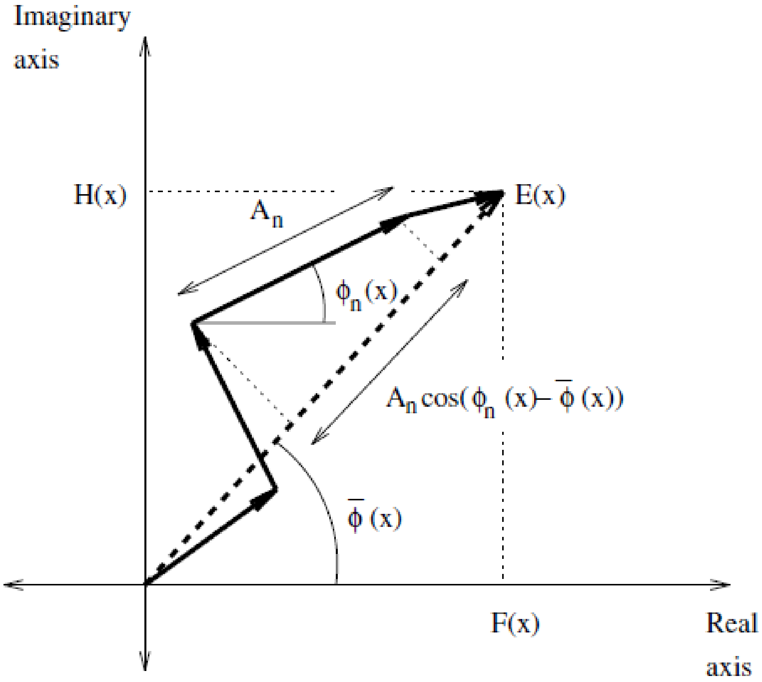

Figure 2.14: Polar diagram showing the Fourier components at a location in the signal plotted head to tail.

2.5.5 Phase Congruency Model for Digital Images

In 1999, Kovesi developed the phase congruency model for the digital images. Phase congruency value corresponding to pixel x in a given digital is computed by:

$$\mathrm{PC}(x) = \frac{\sum_o \sum_n W_o(x) \lfloor A_{no}(x) \Delta\Phi_{no}(x) - T_o \rfloor}{\sum_o \sum_n A_{no}(x) + \varepsilon} \tag{2.4}$$

where "*o*" and "*n*" denote the indexes over orientation and wavelet scale respectively. Function $\lfloor . \rfloor$ returns its enclosed quantity when the value is positive and zero otherwise,

$$\lfloor u \rfloor = \begin{cases} u\,, & u \geq 0 \\ 0\,, & otherwise \end{cases} .$$

For a given orientation, *o*, W_o is a weighting function for phase congruency, A_{no} is the amplitude of the transform at the given wavelet scale *n*. $\Delta\Phi_{no}(x)$ is a measure of phase congruency, and T_o compensates the effect of noise in the phase congruency calculation. To prevent division of zero in numerical calculations, $\varepsilon = 0.001$ is added.

It should be noted that Equation 2.4 is an extension of Equation 2.3 into two dimensions with some modification such as response to noise.

2.5.6 Phase Congruency Parameters

A major disadvantage of the phase congruency model is its computational intensiveness. For example, for estimating a value for amplitude, a filter bank with both radial and angular filter components is regarded.

2.5.6.1 Amplitude

In Equation 2.4, A_{no} is amplitude of the transform at given wavelet scale, *n*, over orientation, *o*. For a given orientation *o* the amplitude is calculated by: $A_n(x) = \sqrt{e_n(x)^2 + o_n(x)^2}$ where $e_n(x)$ and $o_n(x)$ are the result of convolving the image intensity function into the even-symmetric (cosine) and odd-symmetric (sine) filters at scale n respectively.

In terms of convolution theorem,

$$e_n(x) = real\left[F^{-1}\{IM(x)\,.\,filter\}\right] ,$$

$$o_n(x) = imag\left[F^{-1}\{IM(x)\,.\,filter\}\right],$$

where $IM(x)$ represents the Fourier transformed of the image and *filter* is a designed filter bank in terms of log-Gabor function.

On linear frequency scale the log-Gabor function has a transfer model as:

$$G_r = \frac{-\log\left(r/f\right)^2}{2\log(\sigma)^2} \qquad (2.5)$$

where r is the radius filter of a given pixel in polar system , f is the minimum center frequency of filter and σ controls the filter bandwidth.

Note that in polar coordinate system basically each pixel recalls by (r,θ) where

$$r = \sqrt{x^2 + y^2} \text{ and } \theta = \tan^{-1}\left(\frac{-y}{x}\right).$$

With assumption of the wavelength of smallest scale filter ($\lambda_{\min}$) as minimum wavelength, the maximum wavelength will be defined by:

$$\lambda_{\max} = \lambda_{\min} * \alpha^{n-1} ,$$

where α is the scaling between the center frequency of successive filters and n is the number of wavelet scales.

Minimum centre frequency of filter is related by maximum wavelength in a filter by: $f_{\min} = \frac{1}{\lambda_{\max}}$.

In Equation 2.5, σ controls the filter bandwidth. For example using σ = 0.75 covers approximately one octave filter bandwidth and using σ = 0.55 approximately covers two octaves filter bandwidth.

An octave is the interval between two points where the frequency at the second point is twice the frequency of the first (see Figure 2.15). One and two octaves bandwidth for a given frequency is listed in Table 2.1.

Table 2.1: Upper and lower frequency bound for one and two octaves bandwidth.

	f_1 Lower frequency bound	f_c Middle frequency	f_2 Upper frequency bound
One octave bandwidth	$\frac{f_c}{\sqrt{2}}$	f_c	$\sqrt{2} f_c$
Two octaves bandwidth	$\frac{f_c}{2}$	f_c	$2 f_c$

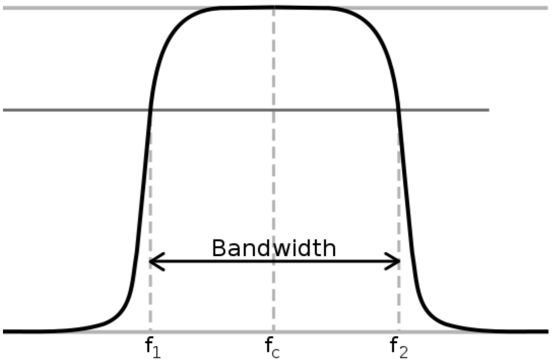

Figure 2.15: Frequency bandwidth for f_c with lower bound f_1 and upper bound f_2.

Approximate one octave bandwidth and two octaves bandwidth coverage is given in Table 2.2.

Table 2.2: Approximate coverage of bandwidth

σ	α	Coverage of bandwidth
0.85	1.3	Half octave
0.75	1.6	One octave
0.65	2.1	One and half octaves
0.55	3.0	Two octaves

The filter bank is designed in both radial component, C_r, and angular component, C_θ. The radial component controls the frequency band and the angular component controls the orientation. Overall filter bank will then be constructed by multiply both radial and angular components.

By multiplying the log-Gabor filter into a low-pass filter, the radial filter component will be constructed.

A low-pass filter for a given filter radius is calculated by:

$lp_r = \dfrac{1}{1+\left(\dfrac{r}{c}\right)^{2N}}$, where r is radial, c is cut-off frequency and N is order of the filter which controls sharpness of filter.

The filter bank for a given radial component, r, is constructed by:

$$C_r = lp_r \,.\, G_r$$

where lp_r low- pass filter and G_r is log-Gabor filter.

The angular filter component is constructed by the angular spread filter. The angular spread of filter is computed by: $C_\theta = e^{\frac{-(\theta-\theta_i)^2}{2\sigma_\theta^2}}$ where θ_i is the orientation angle of the filter and defined by $\theta_i = \frac{(i-1)\pi}{o}$, where *i* denotes the current orientation and *o* is the number of orientation. For example for calculation PC(*x*) over 6 orientations (*o* = 6), filter angles is set as:

$$\left\{\theta_1 = 0, \theta_2 = \frac{\pi}{6}, \theta_3 = \frac{\pi}{3}, \theta_4 = \frac{\pi}{2}, \theta_5 = \frac{2\pi}{3}, \theta_6 = \frac{5\pi}{6}\right\}.$$

σ_θ is standard deviation of the Gaussian spreading functions in the angular direction and defined by $\sigma_\theta = \frac{\pi}{d\,.\,o}$ where *d* is the ratio of angular interval between filter orientations and the standard deviation of the angular Gaussian function and *o* is the number of orientations.

Finally the filter is contracted by multiplying radial component and angular component, $filter = C_r\,.\,C_\theta$. The amplitude at a given scale n then is numerically calculated by convolving filter in to Fourier transformed of image.

2.5.6.2 Weighting Function

In Equation 2.4, $W_o(x)$ is the phase congruency weighting value at pixel *x* over orientation *o*. Weighting function has sigmoid form and for a given orientation defined as:

$$W(x) = \frac{1}{1+e^{\gamma(C-S(x))}},$$

where C is filter cut-off, value of filter, γ is a gain factor that controls the sharpness of the cut-off and $S(x)$ is the filter response spread and defined by:

$$S(x) = \frac{1}{N}\left(\frac{\sum_n A_n(x)}{A_{\max}(x) + \varepsilon} \right),$$

where N is the total number of scales being considered, $A_{\max}(x)$ is the amplitude of the filter pair having maximum response at x and ε is added to prevent division by zero.

2.5.6.3 A new Measure of Phase Congruency

A new measure of phase congruency is developed in original paper by (Kovesi, 1999).

$$\Delta\Phi_n(x) = \cos(\phi_n(x) - \bar{\phi}(x)) - \left| \sin(\phi_n(x) - \bar{\phi}(x)) \right|,$$

where $\phi_n(x)$ is the local phase of the amplitude $A_n(x)$ defined by:

$$\phi_n(x) = \tan^{-1}\left(\frac{e_n(x)}{o_n(x)} \right),$$

where $e_n(x)$ and $o_n(x)$ are the result of convolving the image intensity function into the even-symmetric (cosine) and odd-symmetric (sine) filters at scale n respectively.

2.5.6.4 Noise

Phase congruency model is highly depended on noise in a given image. For example for a given step function, phase congruency values has only one high peak value at step point. while there is no significant high peak value in phase congruency values when the step function is became noisy even small value of noises (see Figure 2.16).

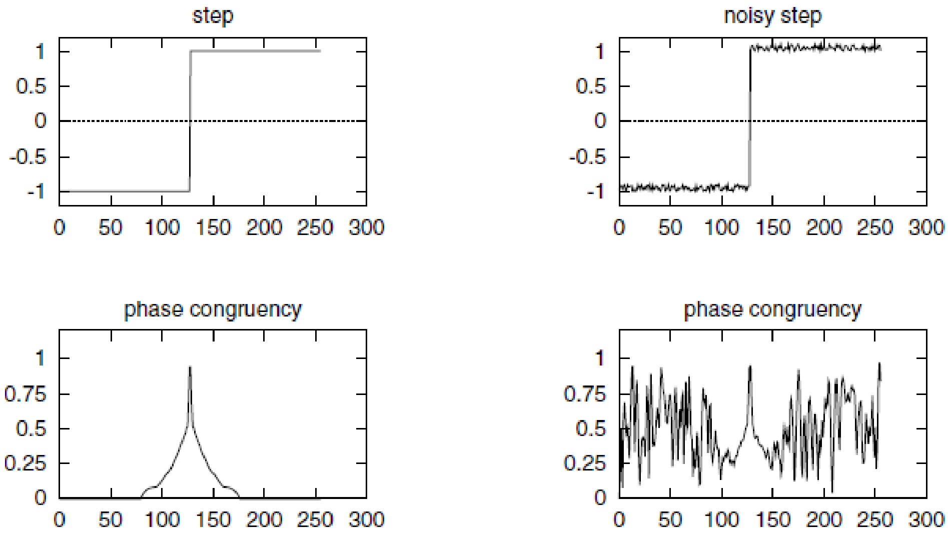

Figure 2.16: Phase congruency of a set function with and without noise.

It should be noted that features in an image such as edges occur at isolated locations. Due to the points that image noise is additive and power spectrum of the noise is constant, a value for the noise circle radius is calculated by $T=\mu_R+k\,.\,\sigma_R$, where the parameter k controls the amount of noise and in practice can be vary up to 20. For a noisy image this factor can be vary up to 20. μ_R is the mean and σ_R is the standard deviation of noise which has Rayleigh distribution with form of

$$R(x)=\frac{x}{\sigma_G^2}e^{\frac{-x^2}{2\sigma_G^2}},$$

where σ_G^2 is the variance of the Gaussian distribution .

Mean (μ_R) and standard deviation (σ_R) of a Rayleigh distribution with variance σ_G^2 are calculated respectively by:

$$\mu_R = \sigma_G \sqrt{\frac{\pi}{2}} \text{ and } \sigma_R^2 = \frac{4-\pi}{2}\sigma_G^2 .$$

where σ_G^2 is second moment of noise energy (expected value of squared noise energy) where noise energy is calculated by:

$$E(x) = \sqrt{\left(\sum_n e_n(x)\right)^2 + \left(\sum_n o_n(x)\right)^2} ,$$

where $e_n(x)$ and $o_n(x)$ are even and odd filter component of noise at scale n respectively.

The expected value for squared noise energy based on even and odd filter components calculated by:

$$\mathrm{E}\left(E^2(x)\right) = \mathrm{E}\left[\left(\sum_n e_n(x)\right)^2 + \left(\sum_n o_n(x)\right)^2\right]$$

$$= \mathrm{E}\left[\sum_n (e_n(x))^2\right] + \mathrm{E}\left[\sum_n (o_n(x))^2\right] + \mathrm{E}\left[2\sum_{i<j}\left(e_i(x)\, e_j(x) + o_i(x)\, o_j(x)\right)\right].$$

Since $e_n(x)$ and $o_n(x)$ are identical and independent, therefore ,

$$\mathrm{E}\left(E^2(x)\right) = 2\mathrm{E}\left[\sum_n (e_n(x))^2\right] + 4\mathrm{E}\left[2\sum_{i<j}\left(e_i(x)\, e_j(x)\right)\right].$$

Let g is noise signal and $\hat{g}$ is its Fourier transform where $|\hat{g}|$ is constant. $|\hat{g}|^2$ is estimated by $|\hat{g}|^2 \approx \frac{\mathrm{E}\left(A_N^2\right)}{\mathrm{E}(F(M_n)^2)}$ where N is the index of the smallest scale filter, and $\mathrm{E}\left(A_N^2\right) = \frac{-\,median\,\left(A_N^2\right)}{\ln(1/2)}$.

With assumption of $e_n(x) = g * M_n$ where M_n is the even filter component with zero mean then we have

$$\mathrm{E}\left(E^2\right) = 2\mathrm{E}\left(\sum_n (M_n * g)^2\right) + 4\mathrm{E}\left(\sum_{i<j} (M_i * g).(M_j * g)\right)$$

$$= 2\mathrm{E}\left(\sum_n \left(\hat{M}_n * \hat{g}\right)^2\right) + 4\mathrm{E}\left(\sum_{i<j} F^{-1}\left(\hat{M}_i.\hat{g}\right) * \left(\hat{M}_j.\hat{g}\right)\right)$$

$$= 2|\hat{g}|^2\ \mathrm{E}\left(\sum_n \hat{M}_n{}^2\right) + 4\mathrm{E}\left(\sum_{i<j} F^{-1}\left(|\hat{g}|^2 . \left(\hat{M}_n * \hat{M}_n\right)\right)\right)$$

$$= 2|\hat{g}|^2\ \mathrm{E}\left(\sum_n (F(M_n))^2\right) + 4\,|\hat{g}|^2\ \mathrm{E}\left(\sum_{i<j} M_i \,.\, M_j\right).$$

2.6 Literature Review on Discriminant Analysis

Pair-wise discrimination of two diseases is conducted with two well-known discrimination procedures, namely, nearest neighbour method and so-called normal discriminant functions. In this section we give a brief literature review on both parametric and non-parametric discriminant procedures.

2.6.1 Non-Parametric Discriminant Function

Nearest neighbour method is a simple non parametric discrimination method which is widely used in statistics for allocating or labeling a given observation. Suppose we have two different multivariate populations namely π_1 and π_2. Let $\underline{X}_1, \underline{X}_2, ..., \underline{X}_{n1}$ are random samples from π_1 and similarly $\underline{Y}_1, \underline{Y}_2, ..., \underline{Y}_{n2}$ represent random samples from

π_2. Let $\overline{\underline{X}}$ and $\overline{\underline{Y}}$ be the centre of gravity for population π_1 and π_2 respectively. $\overline{\underline{X}}$ and $\overline{\underline{Y}}$ may be calculated by mean, median or even mode. For a given new observation $\underline{V}$, if $d(\underline{V},\overline{\underline{X}}) < d(\underline{V},\overline{\underline{Y}})$ then we say $\underline{V} \in \pi_1$ otherwise, $\underline{V} \in \pi_2$. Here *d* is a distance measure such as the Euclidean distance, Minkowski distance or the Mahalanobis distance.

2.6.2 Parametric Discriminant function

In this section, we discuss two well-known parametric discriminant functions, called, Linear Discriminant Function (LDF) and Quadratic Discriminant Function (QDF). It should be noted that LDF and QDF are valid if random variables are normally distributed (Johnson & Wichern, 2002).

The normal distribution is widely in used in statistics. A given univariate random variable, *X*, is normally distributed say $X : X \sim N(\mu, \sigma^2)$, when the probability density function (PDF) has the form of

$$f(x) = \frac{1}{\sigma\sqrt{2\pi}} e^{\frac{-(x-\mu)^2}{2\sigma^2}} \quad , \ -\infty < x < \infty ,$$

where μ and σ^2 are the mean and variance respectively.

The normal probability density function for p-dimension random vector is defined by:

$$f(\underline{X}) = \frac{1}{(2\pi)^{p/2} |\Sigma|^{1/2}} e^{\frac{-(\underline{X}-\underline{\mu})^T \Sigma^{-1} (\underline{X}-\underline{\mu})}{2}} \quad , \ \underline{X} \in \Re^p ,$$

where $\underline{\mu}$ is the mean vector and $\sum$ is the covariance matrix assumed positive definite (Johnson & Wichern, 2002).

In statistics two populations may be discriminated using LDF or QDF with relatively high efficiency when their random variables are normally distributed (Johnson & Wichern, 2002).

Let $f_j(\underline{X})$ denotes the PDF of population π_j, namely, $\pi_j : \underline{X} \sim N_p(\underline{\mu}_j, \Sigma_j)$,

where, $f_j(\underline{X}) = \dfrac{1}{(2\pi)^{p/2} \left|\Sigma_j\right|^{1/2}} e^{\frac{-(\underline{X}-\underline{\mu}_j)^T \Sigma_i^{-1} (\underline{X}-\underline{\mu}_j)}{2}} \quad j = 1,2$.

A discrimination procedure that minimizes the expected costs of misclassifications (ECM) is given as follows:

Let $D(\underline{X}) = \ln\left(\dfrac{f_1(\underline{X})}{f_2(\underline{X})}\right)$. A given $\underline{X}_0$, is allocated to population π_1 if $D(\underline{X}_0) \geq \ln(C)$, and alternatively $D(\underline{X}_0)$ implies $\underline{X}_0 \in \pi_2$ when $D(\underline{X}_0) < \ln(C)$,

where $C = \left(\dfrac{c(1\,|\,2)}{c(2\,|\,1)}\right)\left(\dfrac{p_2}{p_1}\right)$, p_1 and p_2 are the prior probability corresponding to population π_1 and π_2 respectively. $c\,(1\,|\,2)$ is the cost of misclassification when $\underline{X}_0$ is wrongly labelled as π_1 and $c\,(2\,|\,1)$ is the cost of misclassification corresponding to population π_2.

For two populations with equal prior probabilities and equal costs of misclassification (C = 1), $\underline{X}_0$ is allocated to π_1 if $D(\underline{X}_0) > 0$ and alternatively $D(\underline{X}_0) < 0$ implies that $\underline{X}_0 \in \pi_2$.

In particular for the case of equal covariance matrices for population π_1 and π_2 $(\Sigma_1 = \Sigma_2 = \Sigma)$, The LDF is defined by:

$$L(\underline{X}) = \left(\underline{\mu}_1 - \underline{\mu}_2\right)^T \Sigma^{-1} \underline{X} - \frac{1}{2}\left(\underline{\mu}_1 - \underline{\mu}_2\right)^T \Sigma^{-1}\left(\underline{\mu}_1 + \underline{\mu}_2\right),$$

where $\underline{\mu}_1$, $\underline{\mu}_2$ and Σ are known. In practice usually $\underline{\mu}_1$, $\underline{\mu}_2$ and Σ are unknown and the parameters must be estimated.

Let $X = \begin{bmatrix} \underline{X}_1 \\ \underline{X}_2 \\ \vdots \\ \underline{X}_{n_1} \end{bmatrix}$ from π_1 and $Y = \begin{bmatrix} \underline{Y}_1 \\ \underline{Y}_2 \\ \vdots \\ \underline{Y}_{n_2} \end{bmatrix}$ from π_2. The parameters $\underline{\mu}_1$, $\underline{\mu}_2$ and Σ are then estimated as follows,

$$\hat{\underline{\mu}}_1 = \frac{1}{n_1}\sum_{j=1}^{n_1} \underline{X}_j \ ,$$

$$\hat{\underline{\mu}}_2 = \frac{1}{n_2}\sum_{j=1}^{n_2} \underline{Y}_j \text{ and}$$

$$S = \left[\frac{n_1 - 1}{(n_1 - 1) + (n_2 - 1)}\right]\hat{\Sigma}_1 + \left[\frac{n_2 - 1}{(n_1 - 1) + (n_2 - 1)}\right]\hat{\Sigma}_2, \text{ where}$$

$$\hat{\Sigma}_1 = \frac{1}{n_1 - 1}\sum_{j=1}^{n_1}\left(\underline{X}_j - \hat{\underline{\mu}}_1\right)\left(\underline{X}_j - \hat{\underline{\mu}}_1\right)^T \text{ and } \hat{\Sigma}_2 = \frac{1}{n_2 - 1}\sum_{j=1}^{n_2}\left(\underline{Y}_j - \hat{\underline{\mu}}_2\right)\left(\underline{Y}_j - \hat{\underline{\mu}}_2\right)^T .$$

A given $\underline{X}_0$ is allocated to π_1 if

$$\hat{L}(\underline{X}_0) = \left(\hat{\underline{\mu}}_1 - \hat{\underline{\mu}}_2\right)^T S^{-1} \underline{X}_0 - \frac{1}{2}\left(\hat{\underline{\mu}}_1 - \hat{\underline{\mu}}_2\right)^T S^{-1}\left(\hat{\underline{\mu}}_1 + \hat{\underline{\mu}}_2\right) \geq \ln(C),$$

Alternatively $\underline{X}_0$ is allocated to π_2 when $\hat{L}(\underline{X}_0) < \ln(C)$, where $C = \left(\frac{c(1\,|\,2)}{c(2\,|\,1)}\right)\left(\frac{p_2}{p_1}\right)$.

In the case of non-equal covariance matrices for population π_1 and π_2, $\Sigma_1 \neq \Sigma_2$, the quadratic discriminant function (QDF) allocates a given $\underline{X}_0$ to π_1 if

$$Q(\underline{X}_0) = -\frac{1}{2}\underline{X}_0^T\left(\hat{\Sigma}_1^{-1} - \hat{\Sigma}_2^{-1}\right)\underline{X}_0 + \left(\hat{\mu}_1^T\hat{\Sigma}_1^{-1} - \hat{\mu}_2^T\hat{\Sigma}_2^{-1}\right)\underline{X}_0 - k \geq \ln(C),$$

otherwise $\underline{X}_0$ is allocated to π_2, where

$$k = \frac{1}{2}\ln\left(\frac{|\hat{\Sigma}_1|}{|\hat{\Sigma}_2|}\right) + \frac{1}{2}\left(\underline{\hat{\mu}}_1^T\hat{\Sigma}_1^{-1}\hat{\mu}_1 - \underline{\hat{\mu}}_2^T\hat{\Sigma}_2^{-1}\hat{\mu}_2\right) \text{ and } C = \left[\left(\frac{c(1\,|\,2)}{c(2\,|\,1)}\right)\cdot\left(\frac{p_2}{p_1}\right)\right].$$

The parameters $\underline{\mu}_1$, $\underline{\mu}_2$, Σ_1 and Σ_2 are estimated as follows:

$$\underline{\hat{\mu}}_1 = \frac{1}{n_1}\sum_{j=1}^{n_1}\underline{X}_j \ ,$$

$$\underline{\hat{\mu}}_2 = \frac{1}{n_2}\sum_{j=1}^{n_2}\underline{Y}_j \ ,$$

$$\hat{\Sigma}_1 = \frac{1}{n_1 - 1}\sum_{j=1}^{n_1}\left(\underline{X}_j - \underline{\hat{\mu}}_1\right)\left(\underline{X}_j - \underline{\hat{\mu}}_1\right)^T \text{ and}$$

$$\hat{\Sigma}_2 = \frac{1}{n_2 - 1}\sum_{j=1}^{n_{21}}\left(\underline{Y}_j - \underline{\hat{\mu}}_2\right)\left(\underline{Y}_j - \underline{\hat{\mu}}_2\right)^T .$$

CHAPTER 3

SIMULATION STUDIES

3.1 Introduction

The main challenge of this study is discriminating two populations when they are similar or close to each other. Therefore an appropriate feature may help to have well discriminated populations. In this chapter, two simulation studies were carried out. Firstly, the special case of discriminating two similar multivariate normal (MVN) populations was studied. The second simulation study, investigates the choice of phase congruency model parameters which will determine the appropriate feature for discrimination.

3.2 Simulation Study on Discrimination Two Similar Populations

Consider two MVN populations in their canonical form. $\pi_1 : \underline{X} \sim N_p(\underline{0}, I)$ where I is the identity matrix of size p x p, and $\pi_2 : \underline{X} \sim N_p(\underline{\mu}, D)$ where $\underline{\mu}^T = (\mu_1, \mu_2, ..., \mu_p)$ and $D = diag(d_1, d_2, ..., d_p)$. The procedure of simulation study for discriminating two populations π_1 and π_2 is as follows:

- **Step 1: Sample Generation**

Since both covariance matrices are diagonal, each element of $\underline{X} = (x_1, x_2, ..., x_p)$ from both population π_1 and π_2 may be generated independently as univariate normal variables.

For population π_1, samples are generated with $x_i \sim N(0,1)$ $i = 1,2,...,p$. Let $\underline{v}_j^T = (x_1, x_2, ..., x_p)$, repeat the process which will then generate $\underline{v}_j^T$, $j = 1,2,...,n_1$.

For population π_2, generate $w_i \sim N(0,1)$ $i = 1,2,...,p$ and calculate $z_i = (\sqrt{d_i})w_i + \mu_i$ which is a $N(\mu_i, d_i)$ random variable. Repeat the process and obtain $\underline{u}_j^T = (z_1, z_2, ..., z_p)$. Finally generate $\underline{u}_j^T$, $j = 1,2,...,n_2$.

- **Step 2: Calculation of Sample Mean and Sample Covariance**

For the control data from π_1, let $m_1 = \frac{n_1}{2}$ and calculate

$$\underline{\bar{v}} = \frac{1}{m_1}\sum_{j=1}^{m_1} \underline{v}_j \quad , \; S_v = \frac{1}{m_1 - 1}\sum_{j=1}^{m_1}[\underline{v}_j - \underline{\bar{v}}]\,[\underline{v}_j - \underline{\bar{v}}]^T \,.$$

For the control data from π_2, let $m_2 = \frac{n_2}{2}$ and calculate

$$\underline{\bar{u}} = \frac{1}{m_2}\sum_{j=1}^{m_2} \underline{u}_j \quad , \; S_u = \frac{1}{m_2 - 1}\sum_{j=1}^{m_2}[\underline{u}_j - \underline{\bar{u}}]\,[\underline{u}_j - \underline{\bar{u}}]^T \,.$$

- **Step 3: Estimation of QDF or LDF**

For the case $D \neq I$, the generated data was used to calculate the quadratic discriminant function (QDF). The QDF allocates a given observation, $\underline{x}_0$, to π_1 if

$$\hat{Q}(\underline{x}_0) = -\frac{1}{2}\underline{x}_0^T \left(S_v^{-1} - S_u^{-1}\right) \underline{x}_0 + \left(\underline{\overline{v}}^T S_v^{-1} - \underline{\overline{u}}^T S_u^{-1}\right) \underline{x}_0 - k \geq 0,$$

otherwise $\underline{x}_0$ is allocated to π_2, where $k = \frac{1}{2}\ln\left(\frac{|S_v|}{|S_u|}\right) + \frac{1}{2}\left(\underline{\overline{v}}^T S_v^{-1} \underline{\overline{v}} - \underline{\overline{u}}^T S_u^{-1} \underline{\overline{u}}\right)$.

For the case $D = I$, the data generated was used to calculate the linear discriminant function (LDF). The LDF allocates a given observation, $\underline{x}_0$, to π_1 if $\hat{L}(\underline{x}_0)>0$ where $\hat{L}(\underline{x}_0) = (\underline{\overline{v}} - \underline{\overline{u}})^T S^{-1} \underline{x}_0 - \frac{1}{2}(\underline{\overline{v}} - \underline{\overline{u}})^T S^{-1} (\underline{\overline{v}} + \underline{\overline{u}})$,

otherwise $\underline{x}_0$ is allocated to π_2, where

$$S = \left[\frac{m_1 - 1}{(m_1 - 1) + (m_2 - 1)}\right] S_v + \left[\frac{m_2 - 1}{(m_1 - 1) + (m_2 - 1)}\right] S_u .$$

The problem of using the wrong discrimination function for a given set of generated data was not considered. For example, when population co-variances are not equal we do not use the LDF to estimate misclassification probabilities.

- **Step 4: Calculation of Misclassification Probability**

Read $\underline{v}_{m_1+1},.....,\underline{v}_{n_1}$ from population π_1 and read $\underline{u}_{m_2+1},.....,\underline{u}_{n_2}$ from population π_2.

For $r = m_1 + 1,...,n_1$, calculate the number of times when $D(\underline{v}_r) < 0$, and this total when divided by $n_1 - m_1$ estimates the proportion (p$_1$) of observations from π_1 that were misclassified. Note that $D(\underline{v}) = \ln\left(\frac{f_{\pi 1}(\underline{v})}{f_{\pi 2}(\underline{v})}\right)$. For $w = m_2 + 1,...,n_2$, calculate the number of times when $D(\underline{u}_w) > 0$, and this total when divided by $n_2 - m_2$ estimates the proportion (p$_2$) of observations from π_2 that were misclassified.

3.2.1 Selection of Parameter Values

Without loss of generality, we assume the generated sample size from π_1 and π_2 are equal ($n_1 = n_2 = n$), with assumption of equal cost of misclassifications and equal prior probabilities, for population π_2 the mean vector is defined as $\underline{\mu}^T = (\mu, \mu, \ldots, \mu)_{1\times p}$, and the covariance matrix is defined as $D = (d, d, \ldots, d)_{p\times p}$. The values of *p*, *n*, *d* and μ together with estimates of the misclassification probabilities is summarized in Table 3.1.

Table 3.1: Probability misclassification of discrimination between canonical normal distribution and vary of multivariate normal distributions.

p	*N*	*d*	*μ*	p_1	p_2		*p*	*n*	*d*	*μ*	p_1	p_2		*p*	*n*	*d*	*μ*	p_1	p_2
2	50	1	0.5	0.56	0.48		3	50	1	0.5	0.68	0.48		4	50	1	0.5	0.48	0.48
2	50	1	1.0	0.52	0.32		3	50	1	1.0	0.36	0.20		4	50	1	1.0	0.28	0.20
2	50	1	1.5	0.16	0.16		3	50	1	1.5	0.28	0.20		4	50	1	1.5	0.12	0.16
2	50	1	2.0	0.16	0.16		3	50	1	2.0	0.12	0.14		4	50	1	2.0	0.08	0.04
2	50	1	2.5	0.08	0.04		3	50	1	2.5	0.04	0.00		4	50	1	2.5	0.04	0.00
2	50	1	5.0	0.00	0.00		3	50	1	5.0	0.00	0.00		4	50	1	5.0	0.00	0.00
2	50	1	10.0	0.00	0.00		3	50	1	10.0	0.00	0.00		4	50	1	10.0	0.00	0.00
2	50	2	0.5	0.48	0.44		3	50	2	0.5	0.52	0.62		4	50	2	0.5	0.56	0.60
2	50	2	1.0	0.40	0.48		3	50	2	1.0	0.40	0.48		4	50	2	1.0	0.40	0.20
2	50	2	1.5	0.18	0.16		3	50	2	1.5	0.22	0.20		4	50	2	1.5	0.16	0.16
2	50	2	2.0	0.16	0.08		3	50	2	2.0	0.12	0.18		4	50	2	2.0	0.10	0.12
2	50	2	2.5	0.04	0.00		3	50	2	2.5	0.00	0.04		4	50	2	2.5	0.04	0.00
2	50	2	5.0	0.00	0.00		3	50	2	5.0	0.00	0.00		4	50	2	5.0	0.00	0.00
2	50	2	10.0	0.00	0.00		3	50	2	10.0	0.00	0.00		4	50	2	10.0	0.00	0.00
2	50	5	0.5	0.16	0.32		3	50	5	0.5	0.32	0.32		4	50	5	0.5	0.42	0.44
2	50	5	1.0	0.48	0.48		3	50	5	1.0	0.22	0.26		4	50	5	1.0	0.36	0.42
2	50	5	1.5	0.24	0.24		3	50	5	1.5	0.12	0.16		4	50	5	1.5	0.28	0.22
2	50	5	2.0	0.12	0.16		3	50	5	2.0	0.14	0.12		4	50	5	2.0	0.10	0.18
2	50	5	2.5	0.00	0.04		3	50	5	2.5	0.02	0.04		4	50	5	2.5	0.04	0.00
2	50	5	5.0	0.00	0.04		3	50	5	5.0	0.00	0.04		4	50	5	5.0	0.00	0.00
2	50	5	10.0	0.00	0.00		3	50	5	10.0	0.00	0.00		4	50	5	10.0	0.00	0.00
2	100	1	0.5	0.40	0.50		3	100	1	0.5	0.46	0.40		4	100	1	0.5	0.68	0.52
2	100	1	1.0	0.38	0.44		3	100	1	1.0	0.40	0.30		4	100	1	1.0	0.54	0.46
2	100	1	1.5	0.18	0.12		3	100	1	1.5	0.12	0.16		4	100	1	1.5	0.16	0.12
2	100	1	2.0	0.12	0.12		3	100	1	2.0	0.04	0.04		4	100	1	2.0	0.00	0.06
2	100	1	2.5	0.00	0.02		3	100	1	2.5	0.02	0.02		4	100	1	2.5	0.02	0.00

2	100	1	5.0	0.00	0.00		3	100	1	5.0	0.00	0.00		4	100	1	5.0	0.00	0.00
2	100	1	10.0	0.00	0.00		3	100	1	10.0	0.00	0.00		4	100	1	10.0	0.00	0.00
2	100	2	0.5	0.40	0.50		3	100	2	0.5	0.38	0.34		4	100	2	0.5	0.46	0.58
2	100	2	1.0	0.30	0.50		3	100	2	1.0	0.32	0.34		4	100	2	1.0	0.44	0.48
2	100	2	1.5	0.12	0.32		3	100	2	1.5	0.18	0.24		4	100	2	1.5	0.22	0.22
2	100	2	2.0	0.20	0.12		3	100	2	2.0	0.04	0.02		4	100	2	2.0	0.14	0.16
2	100	2	2.5	0.04	0.06		3	100	2	2.5	0.02	0.02		4	100	2	2.5	0.02	0.02
2	100	2	5.0	0.00	0.00		3	100	2	5.0	0.00	0.00		4	100	2	5.0	0.00	0.00
2	100	2	10.0	0.00	0.00		3	100	2	10.0	0.00	0.00		4	100	2	10.0	0.00	0.00
2	100	5	0.5	0.36	0.44		3	100	5	0.5	0.38	0.34		4	100	5	0.5	0.44	0.32
2	100	5	1.0	0.24	0.38		3	100	5	1.0	0.24	0.24		4	100	5	1.0	0.18	0.12
2	100	5	1.5	0.10	0.28		3	100	5	1.5	0.16	0.16		4	100	5	1.5	0.12	0.12
2	100	5	2.0	0.04	0.16		3	100	5	2.0	0.10	0.12		4	100	5	2.0	0.02	0.08
2	100	5	2.5	0.04	0.10		3	100	5	2.5	0.02	0.04		4	100	5	2.5	0.04	0.02
2	100	5	5.0	0.00	0.02		3	100	5	5.0	0.00	0.00		4	100	5	5.0	0.00	0.00
2	100	5	10.0	0.00	0.00		3	100	5	10.0	0.00	0.00		4	100	5	10.0	0.00	0.00
2	200	1	0.5	0.58	0.40		3	200	1	0.5	0.55	0.53		4	200	1	0.5	0.60	0.48
2	200	1	1.0	0.35	0.42		3	200	1	1.0	0.35	0.30		4	200	1	1.0	0.37	0.29
2	200	1	1.5	0.17	0.12		3	200	1	1.5	0.21	0.01		4	200	1	1.5	0.06	0.07
2	200	1	2.0	0.06	0.08		3	200	1	2.0	0.06	0.04		4	200	1	2.0	0.04	0.04
2	200	1	2.5	0.04	0.07		3	200	1	2.5	0.01	0.03		4	200	1	2.5	0.00	0.00
2	200	1	5.0	0.00	0.00		3	200	1	5.0	0.00	0.00		4	200	1	5.0	0.00	0.00
2	200	1	10.0	0.00	0.00		3	200	1	10.0	0.00	0.00		4	200	1	10.0	0.00	0.00
2	200	2	0.5	0.55	0.43		3	200	2	0.5	0.46	0.52		4	200	2	0.5	0.53	0.53
2	200	2	1.0	0.42	0.46		3	200	2	1.0	0.35	0.39		4	200	2	1.0	0.29	0.31
2	200	2	1.5	0.27	0.26		3	200	2	1.5	0.21	0.22		4	200	2	1.5	0.11	0.08
2	200	2	2.0	0.07	0.12		3	200	2	2.0	0.15	0.10		4	200	2	2.0	0.03	0.03
2	200	2	2.5	0.03	0.03		3	200	2	2.5	0.03	0.04		4	200	2	2.5	0.02	0.03
2	200	2	5.0	0.00	0.01		3	200	2	5.0	0.00	0.00		4	200	2	5.0	0.00	0.00
2	200	2	10.0	0.00	0.00		3	200	2	10.0	0.00	0.00		4	200	2	10.0	0.00	0.00
2	200	5	0.5	0.13	0.32		3	200	5	0.5	0.44	0.44		4	200	5	0.5	0.52	0.62
2	200	5	1.0	0.10	0.35		3	200	5	1.0	0.23	0.23		4	200	5	1.0	0.33	0.29
2	200	5	1.5	0.09	0.23		3	200	5	1.5	0.14	0.12		4	200	5	1.5	0.17	0.12
2	200	5	2.0	0.04	0.22		3	200	5	2.0	0.18	0.12		4	200	5	2.0	0.13	0.18
2	200	5	2.5	0.01	0.17		3	200	5	2.5	0.02	0.04		4	200	5	2.5	0.02	0.05
2	200	5	5.0	0.00	0.02		3	200	5	5.0	0.00	0.00		4	200	5	5.0	0.00	0.00
2	200	5	10.0	0.00	0.00		3	200	5	10.0	0.00	0.00		4	200	5	10.0	0.00	0.00

3.2.2 Conclusion

Misclassification probabilities are mainly determined by the separation of means, namely the value of μ. When μ is less than 2.5 it is not safe to perform discrimination.

The effect of the other parameters considered are less noticeable. As an illustration considered Figure 3.1.

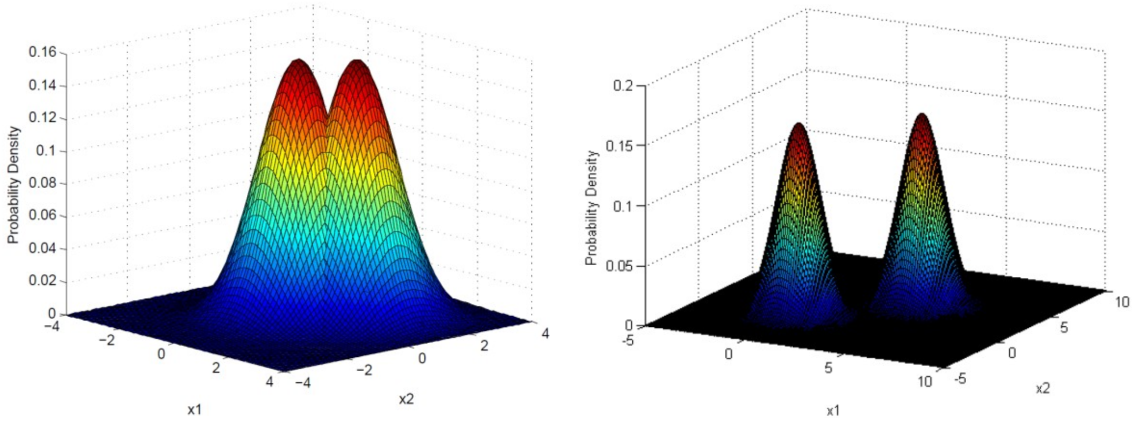

(a) (b)

Figure 3.1: Illustration of overlapping canonical normal distribution with a normal distribution when (a) $\mu = 1$, d = 1 and (b) $\mu = 5$, d = 1.

3.3 Simulation Study on the Phase Congruency Parameters

Phase congruency measures transition between adjacent pixels. Phase congruency value in terms of log-Gabor function is calculated based on nine different parameters. A big challenge on the use of phase congruency the selection of parameter values for a particular application. The correct choices of parameter values will highlight important features, for example, differentiating rib-bone from lung tissue. Phase congruency model is given by (Kovesi, 1999),

$$PC(x) = \frac{\sum_{o}\sum_{n} W_o(x) \lfloor A_{no}(x)\Delta\Phi_{no}(x) - T_o \rfloor}{\sum_{o}\sum_{n} A_{no}(x) + \varepsilon}.$$

Experiments done by Kovesi, recommend the default set parameters, namely, $n = 4$, $o = 6$, $\lambda_{\min} = 3$, $\alpha = 2.1$, $\sigma = 0.55$, $d = 1.2$, $\gamma = 10$, $c = 0.5$ and $k = 2$. where index o and index n determine the number of filter orientations and the number of wavelet scales respectively. Local phase congruency at pixel x is calculated on each orientation. PC(x)-value then calculated with summation of all local values. For a given orientation, $A_n(x)$ is the amplitude of the transform at given wavelet scale n. Amplitude, is computed by convolving the image into a filter. The filter bank is designed in terms of log-Gabor transform in two radial and angular components. Log-Gabor function is obtain while defining a value for $\lambda_{\min}$, α and σ where $\lambda_{\min}$ is determines the minimum wavelength, α is the scaling between the centre frequency of successive filters and σ controls the filter bandwidth.

Parameter d in angular filter component is the ratio between the angular spacing of the filters and angular standard deviation of the Gaussians, in the angular direction.

For calculating the weighting function in PC(x) equation, $W(x)$, two parameters c and γ is used where c is the filter cut-off and γ is the gain factor that controls the sharpness of the cut-off.

Parameter k is a coefficient and is used for the calculation of noise radius circle. T in PC(x) formula is an estimated value for noise radius circle and is added to compensate the effect of noise. Parameter k can vary up to 20 depending on the amount of noise in image. Parameters in PC(x) formula are summarized in Table 3.2.

Table 3.2: Parameters in phase congruency model.

parameter	Description	Used in
n	Number of wavelet scales	Index in PC(x) formula
o	Number of orientation	Index in PC(x) formula
$\lambda_{\min}$	Wavelength of smallest scale	Radial filter component
α	Scaling between the centre frequency of successive filters	Radial filter component
σ	Filter bandwidth factor	Radial filter component
d	The ratio between the angular spacing of the filters and angular standard deviation of the Gaussians, in the angular direction	Angular filter component
γ	Gain factor to control the sharpness of cut-off filter	Weighting phase congruency
c	Filter cut –off	Weighting phase congruency
k	Noise influence factor	Noise radius circle estimation

The default set of parameter values as suggested by Kovesi is used as initial values in our algorithms found in our second simulation exercise. In subsequent simulations only one (say *n*) of the parameter values is varied whilst keeping all other parameter values equal to those recommended by Kovesi. When a new value for this parameter (*n*) is selected the process is repeated by varying the values of a second parameter (say *o*) while all other parameters retain their values except *n* which keeps its new value. The process is repeated until all parameters are investigated. The results are given in Figure 3.2 to Figure 3.9. As an illustration consider Figure 3.2 which shows that when the wavelet scale number, *n*, has a value six the rib-bones and tissues are most clearly seen visually.

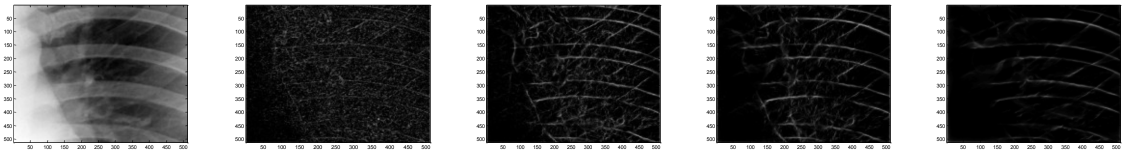

Original of NL $n = 3$ $n = 5$ $n = 6$ $n = 7$

Figure 3.2: Vary of wavelet scale numbers, $n = 6$ is selected.

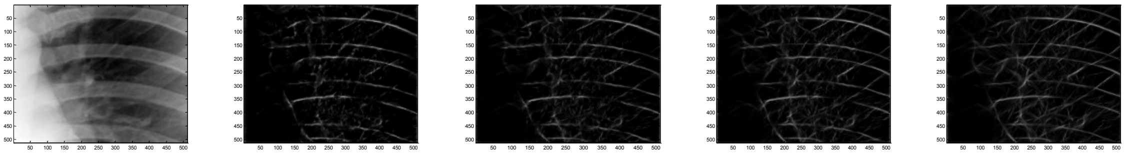

Original of NL $o = 4$ $o = 6$ $o = 8$ $o = 12$

Figure 3.3: Vary of number of orientations, $o = 6$ is selected.

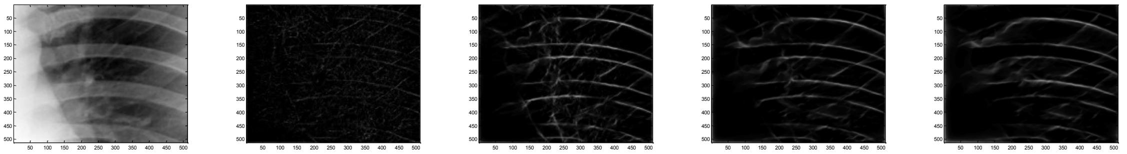

Original of NL $\lambda_{\min} = 1$ $\lambda_{\min} = 4$ $\lambda_{\min} = 6$ $\lambda_{\min} = 8$

Figure 3.4: Changing the wavelength of smallest scale using $n = 6$, $o = 6$.

.

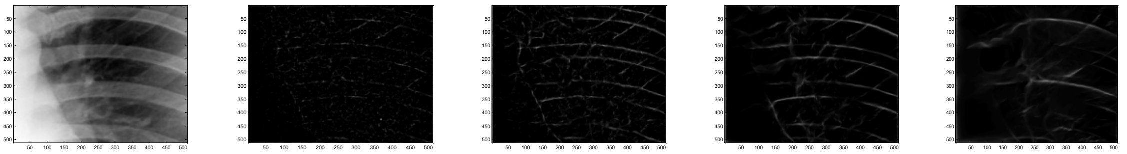

Original of NL $\alpha = 1.3, \sigma = 0.85$ $\alpha = 1.6, \sigma = 0.75$ $\alpha = 2.1, \sigma = 0.65$ $\alpha = 3.0, \sigma = 0.55$

Figure 3.5: Changing the frequency bandwidth using $n = 6$, $o = 6$ and $\lambda_{\min} = 4$.

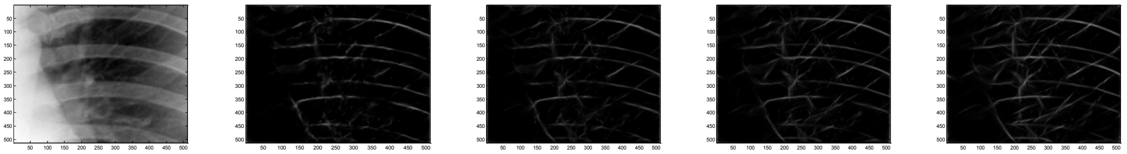

Original of NL $d = 1.0$ $d = 1.5$ $d = 2.0$ $d = 2.5$

Figure 3.6: Changing the angular filter parameter using $n = 6$, $o = 6$, $\lambda_{\min} = 4$, $\alpha = 2.1$ and $\sigma = 0.65$.

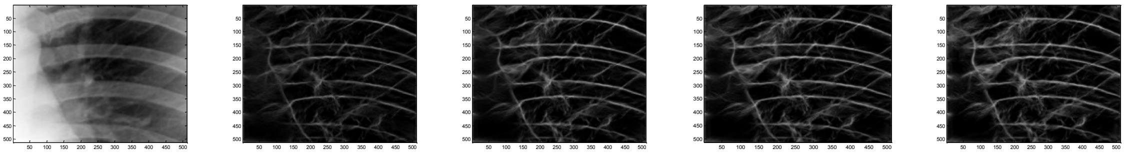

Original of NL $\gamma = 5$ $\gamma = 15$ $\gamma = 25$ $\gamma = 50$

Figure 3.7: Changing the value for sharpness of cut-off filter using $n = 6$, $o = 6$, $\lambda_{\min} = 4$, $\alpha = 2.1$, $\sigma = 0.65$, and $d = 1.5$.

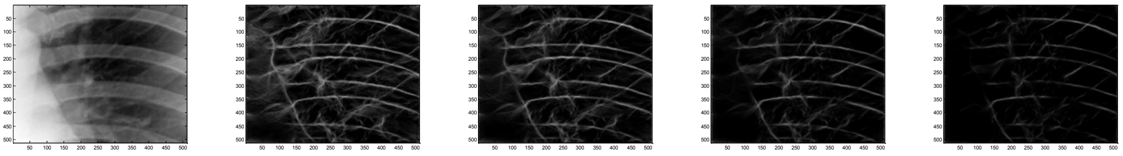

Original of NL $c = 0.2$ $c = 0.3$ $c = 0.4$ $c = 0.5$

Figure 3.8: Changing the filter cut-off value using $n = 6$, $o = 6$, $\lambda_{\min} = 4$, $\alpha = 2.1$, $\sigma = 0.65$, $d = 1.5$ and $\gamma = 15$.

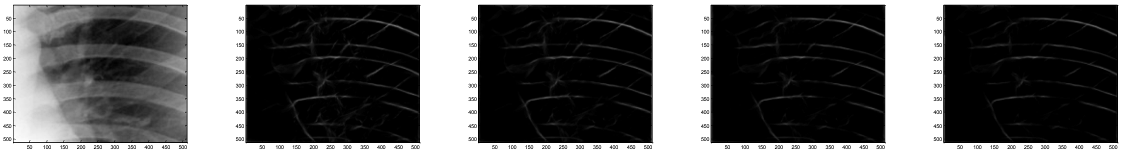

Original of NL $k = 2$ $k = 10$ $k = 15$ $k = 20$

Figure 3.9: Changing the noise controller parameter using $n = 6$, $o = 6$, $\lambda_{\min} = 4$, $\alpha = 2.1$, $\sigma = 0.65$, $d = 1.5$, $\gamma = 15$ and $c = 0.3$.

Finally the selected set parameters for our images are

$n = 6$, $o = 6$, $\lambda_{\min} = 4$, $\alpha = 2.1$, $\sigma = 0.65$, $d = 1.5$, $\gamma = 15$, $c = 0.3$ and $k = 2$.

Using our set of parameter values, the PC(x) transformation were applied to ten NL images, ten LC images, ten PNEU images and ten PTB images (see Figure 3.2 to Figure 3.9). Results visually show that selected set parameters are generally capable of highlighting rib-bone boundaries as well as the ROI.

NL
1

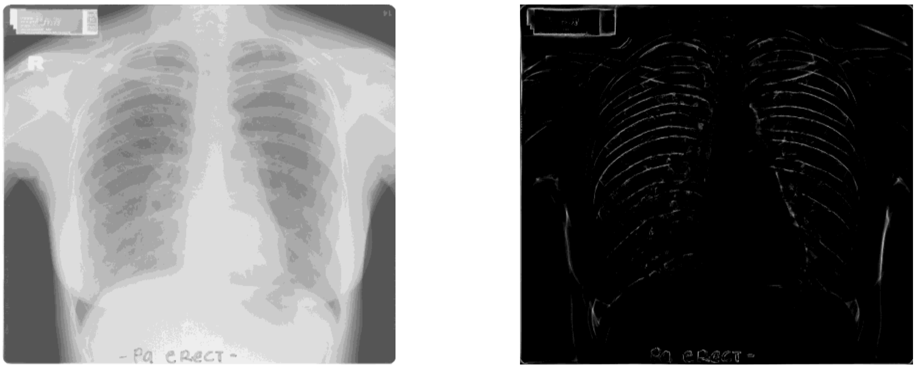

NL
2

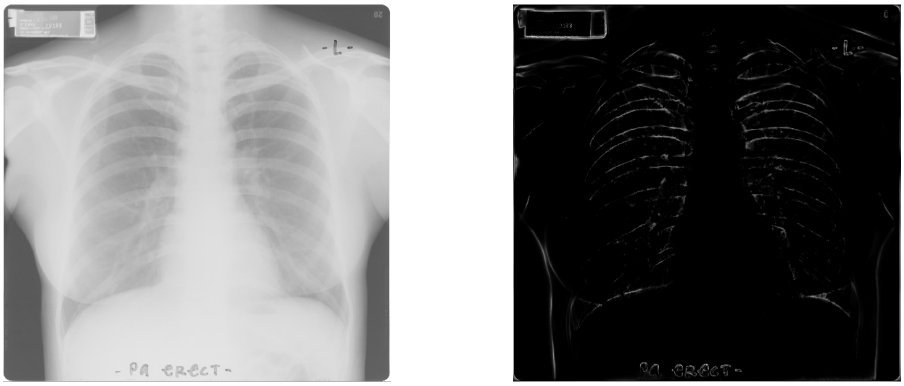

NL
3

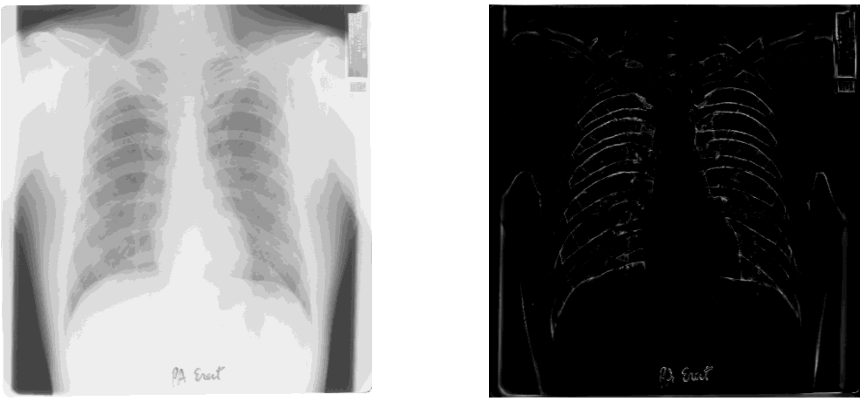

NL
4

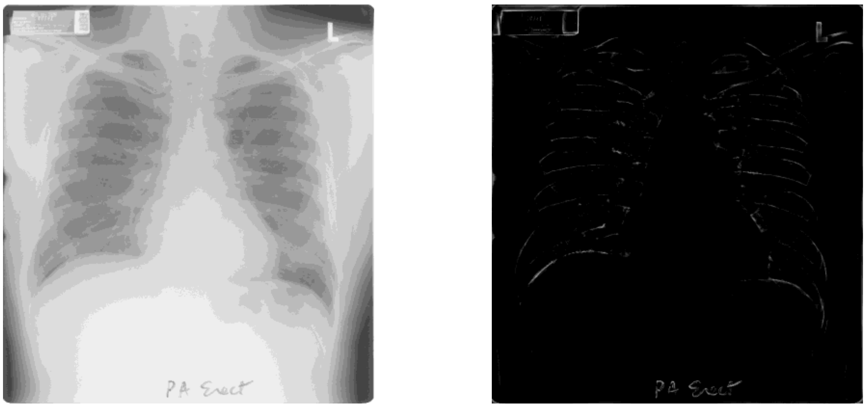

NL
5

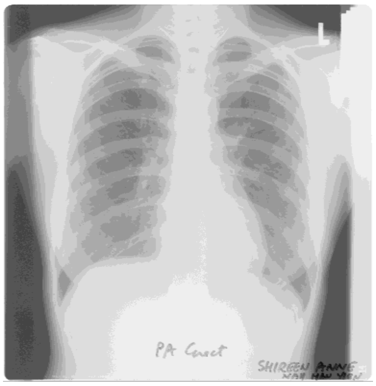

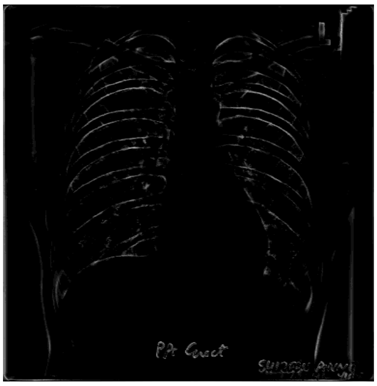

NL
6

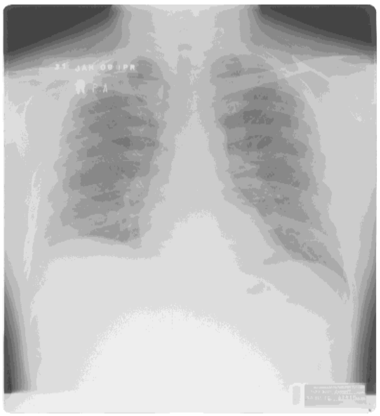

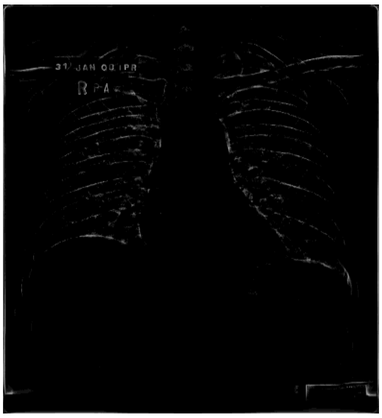

NL
7

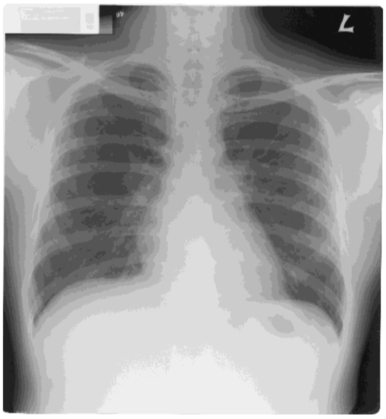

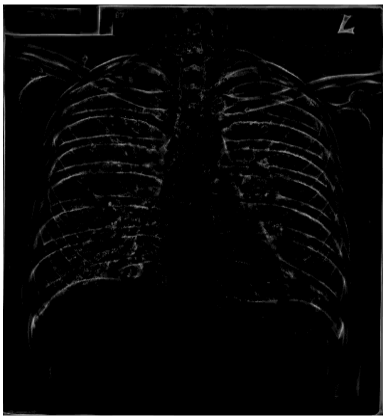

NL
8

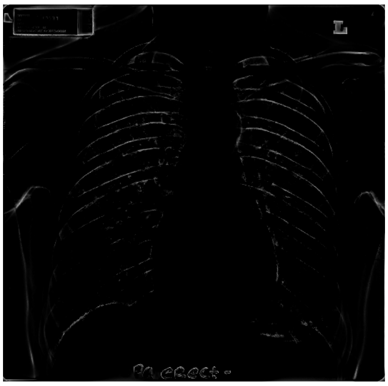

NL
9

NL
10

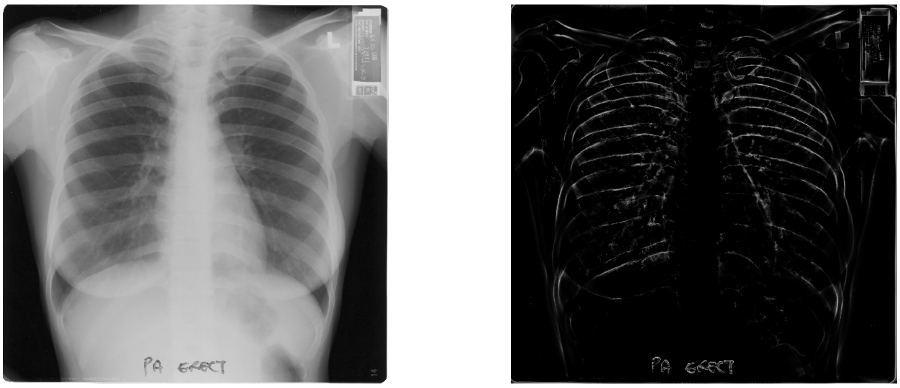

Figure 3.10: Normal lungs and in original gray scale image and phase congruency image.

LC
1

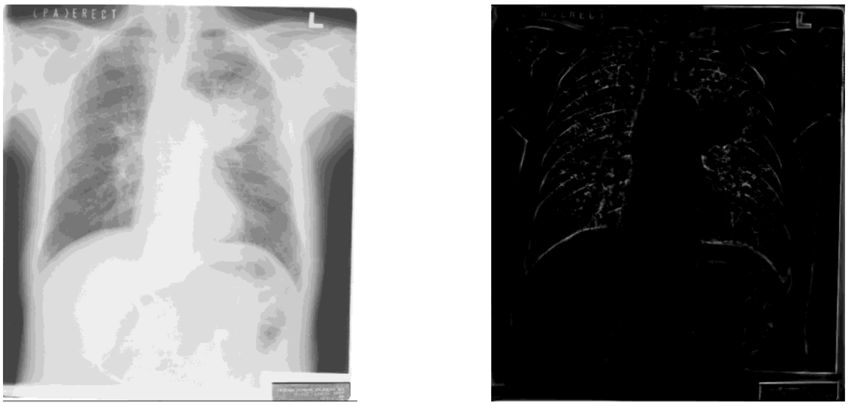

LC
2

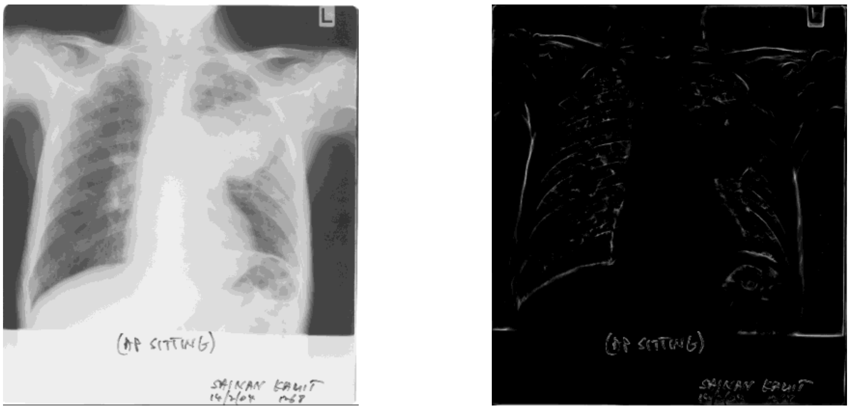

LC
3

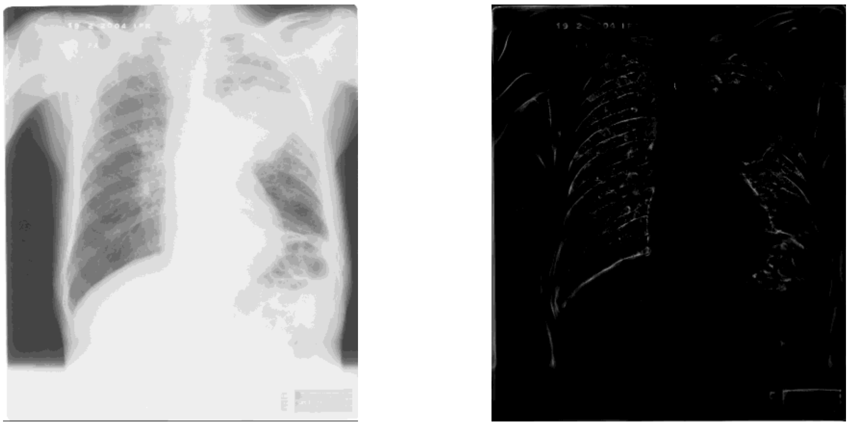

LC
4

LC
5

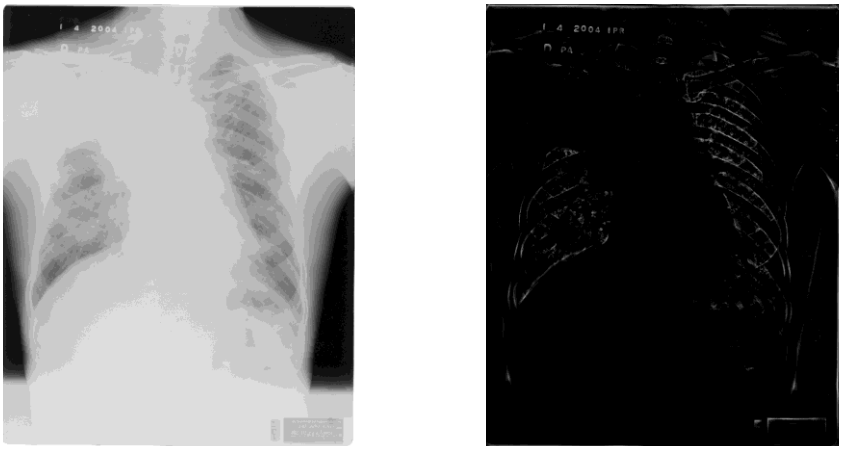

LC
6

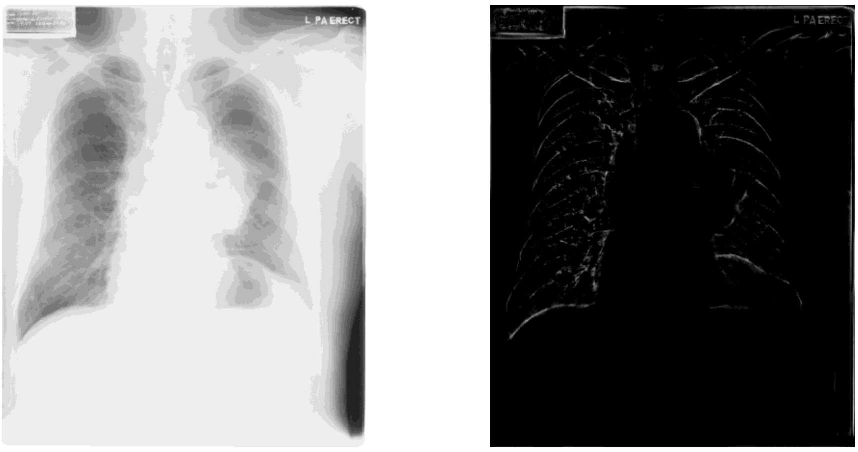

LC
7

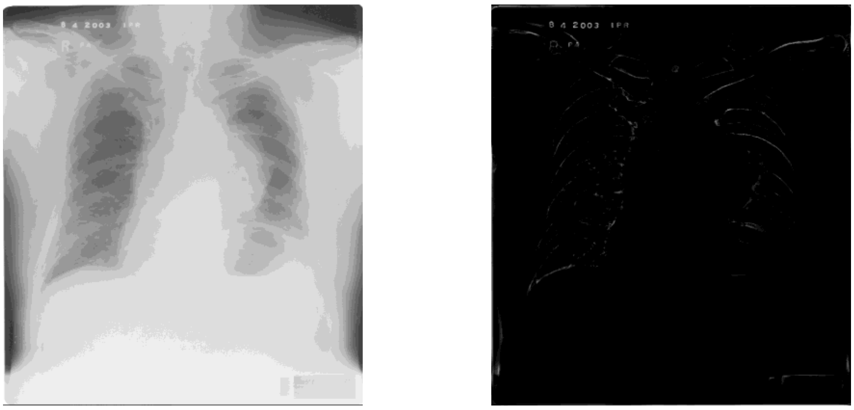

LC
8

LC
9

LC
10

Figure 3.11: Lung cancer cases in original gray scale image and phase congruency image.

PNEU
1

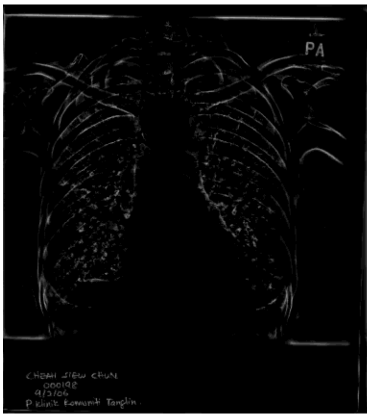

PNEU
2

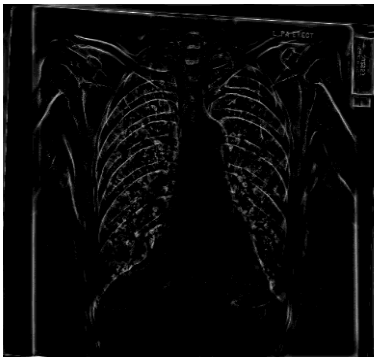

PNEU
3

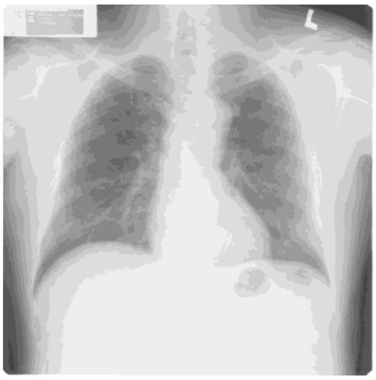

PNEU
4

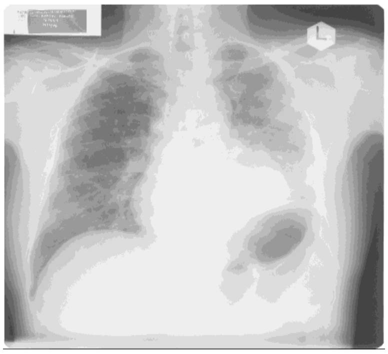

PNEU
5

PNEU
6

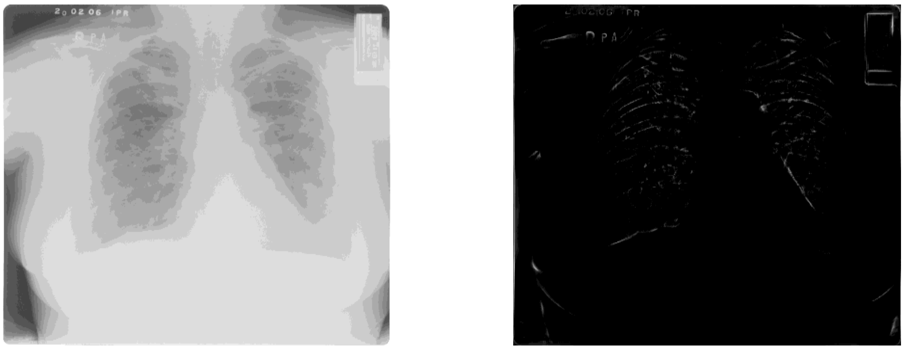

PNEU
7

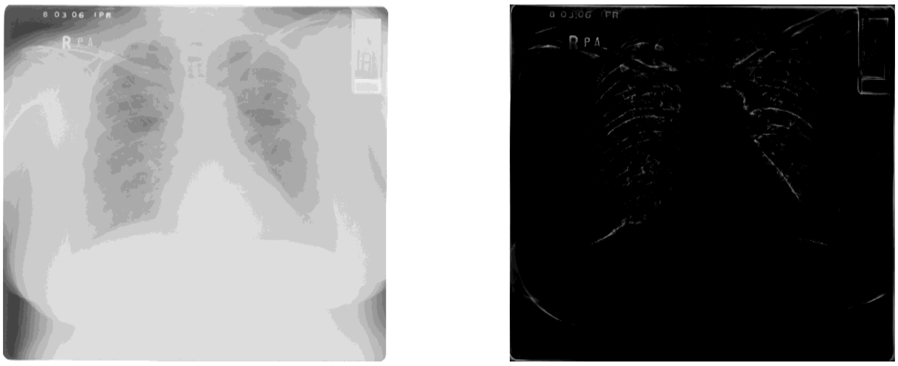

PNEU
8

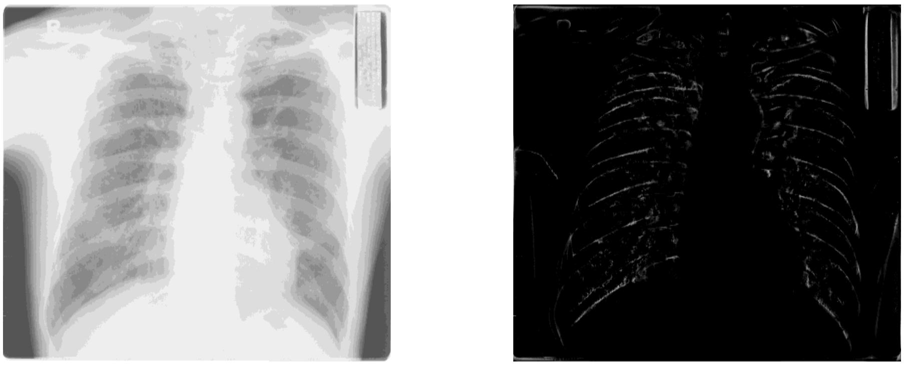

PNEU
9

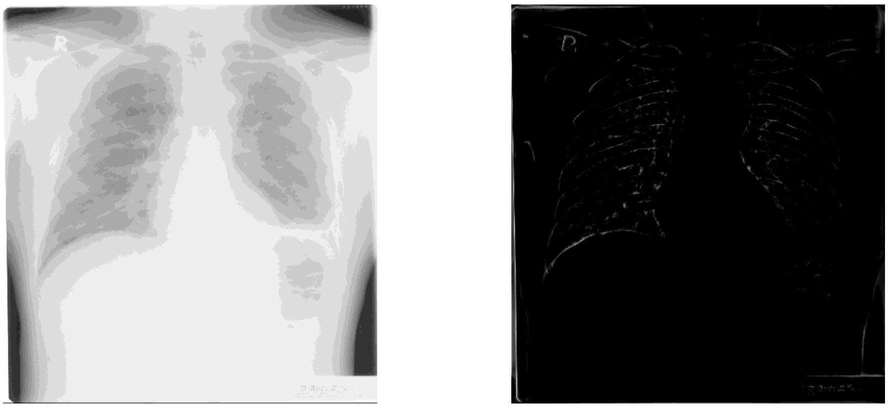

PNEU
10

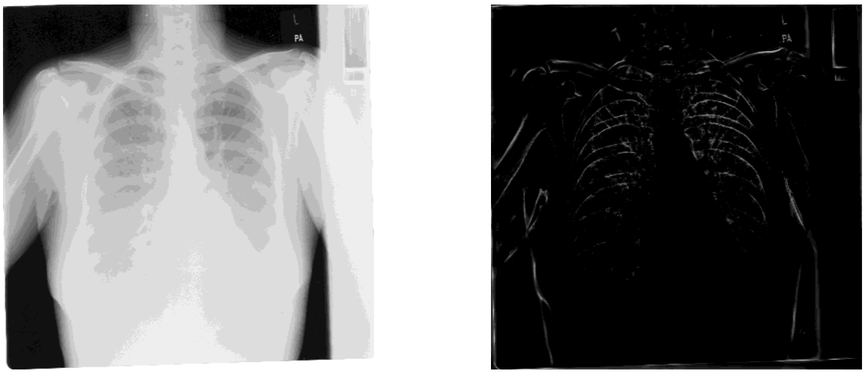

Figure 3.12: Lobar pneumonia cases in original gray scale image and phase congruency image.

PTB
1

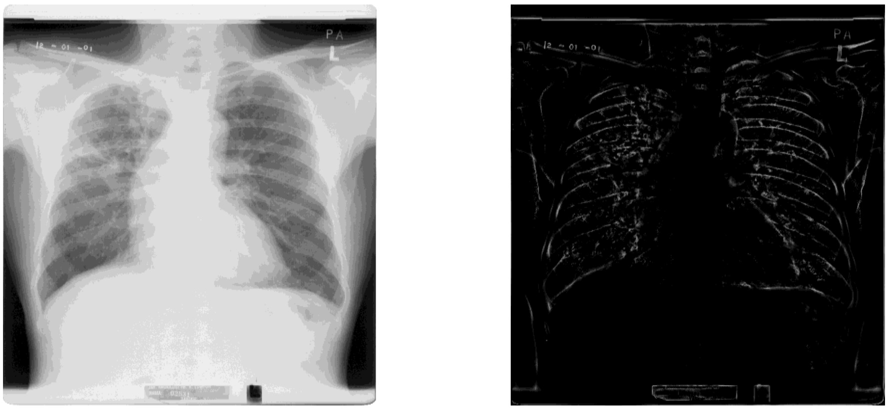

PTB
2

PTB
3

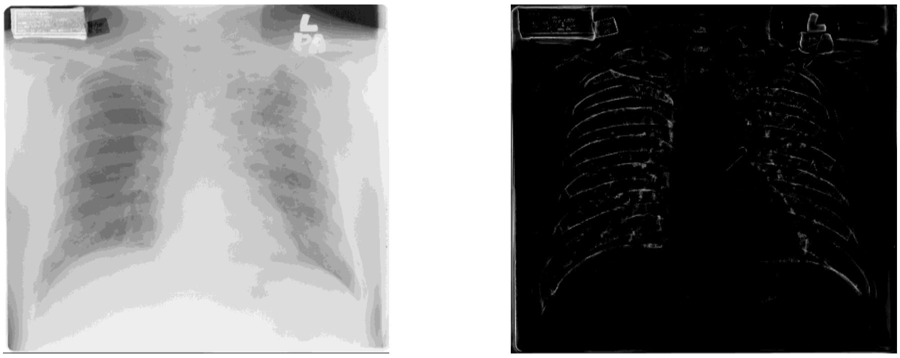

PTB
4

PTB
5

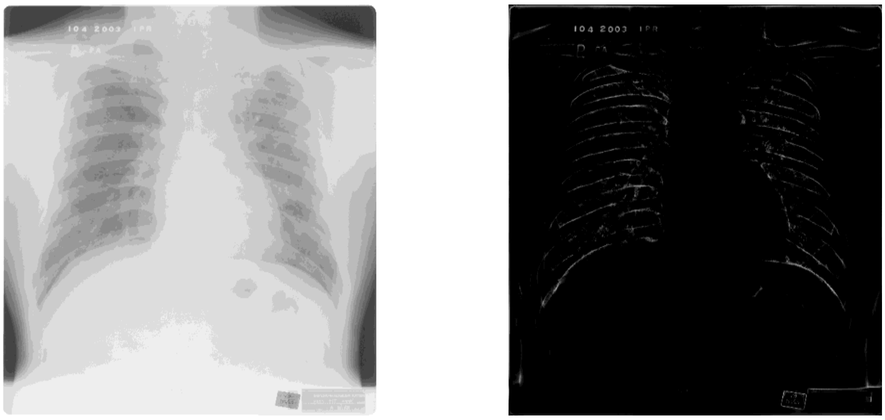

PTB
6

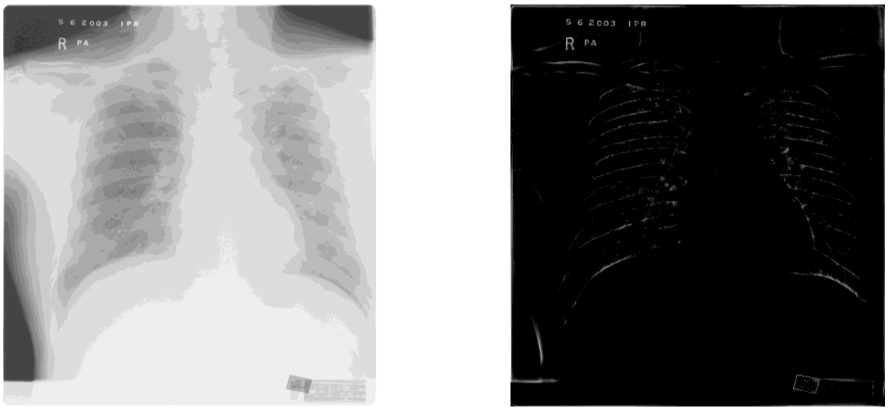

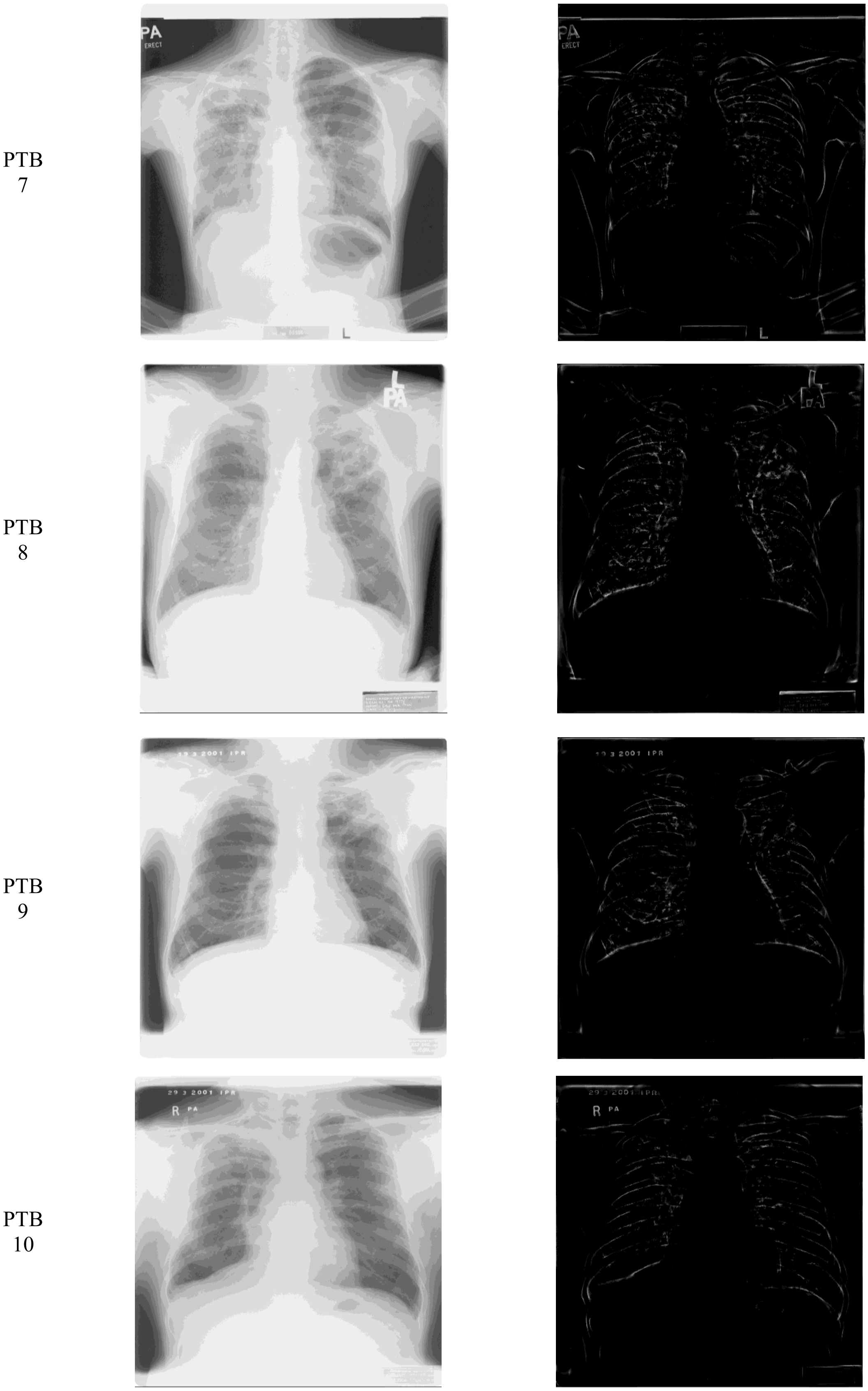

Figure 3.13: Pulmonary tuberculosis cases and in original gray scale image and phase congruency image.

CHAPTER 4

SELECTION OF CASE STUDY

Chest X-ray films were randomly collected from the Institute of Respiratory Medicine (IPR) in Kuala Lumpur. IPR is the national referral center for respiratory diseases. There is a comprehensive database including chest X-ray films and medical information of patients whom treated in the IPR.

Chest X-ray films were captured with Phillips dignost 55/super 50CP machine. To decrease the effect of beam divergence and magnification of structures closer to the X-ray tube, the distance between object and X-ray cassette was fixed at 180 centimetres. Features of X-ray machine is adjusted depending on the patient's sex and weight. The structure of capturing chest X-ray is given in Table 4.1.

Table 4.1: The used details for capturing chest X-ray in IPR

	Normal weight			Under weight		
	Voltage	Ampere	Cassette size	Voltage	Ampere	Cassette size
Male	70 kV	5.0 mA	35 cm × 34cm	64 kV	4.0 mA	35 cm × 34cm
Female	70 kV	5.0 mA	35 cm × 35 cm	64 kV	4.0 mA	35 cm × 35 cm

Chest X-ray films were collected from four different types of diseases namely normal healthy lungs (NL), lung cancer (LC), pulmonary tuberculosis (PTB) and lobar pneumonia (PNEU). To avoid to get any unexpected result, over exposed films and patient's chest X-ray films who have another systemic diseases such as diabetes, hypertension and heart disease were excluded.

Finally, one hundred ninety films were collected in which forty NL X-ray films from patients who come for general check-up or cure after treatments, fifty LC X-ray films, fifty PTB X-ray films and fifty PNEU X-ray films. The X-ray films were collected under direct supervision of a radiologist and confirmed by a pulmonologist.

The chest X-ray films were then digitized into DICOM format using the Kodak LS 75 X-ray Film Scanner with the specifications of pixel spot size of 100 μm, 12 bit per pixel and image size of 2016 × 2048 pixels. Digitized images then confirmed again by the radiologist in IPR.

The collected data set then equally divided into two groups namely control group and test group. Control data set is used to develop a semi automatic procedure to discriminate lung disease and test data set is used to identify probability of misclassification.

CHAPTER 5

DETECTION THE REGION OF INFECTION

5.1 Introduction

Lung diseases such as LC, PNEU and PTB effect lung tissue for either or both right and left lungs. In this chapter, a novel semi-automatic procedure is introduced to remove redundant information from X-ray images which include the diaphragm and heart.

The whole image is segmented into two parts firstly, the lung field (LG) and secondly the non-lung field. The non-lung area includes the diaphragm, heart, spine and every other region outside the lungs, which is simply referred to as the background area (BG). This approach allows the whole image to be converted to a binary image.

Area moments provide information about the distribution of pixel values. The binary image can be found if the area moments for LG is different from BG. Ten area moments are investigated in its ability to discriminate LG from BG, and five distance measures were compared to show or highlight differences between vectors of area moments.

For all images studied the infected area was initially identified and confirmed by two consultant pulmonologists. Henceforth the proposed segmentation method attempts to capture the infected area as defined by these medical experts.

5.2 Methods

Lung field segmentation using statistical moments is explained in this section. The ratio of white pixels over black pixels is used as indicator to detect the ROI. This indicator was validated by testing on existing data set. The procedure of ROI detection is given in Section 5.2.1 to Section 5.2.4. A discussion on binary images is given is Section 5.2.5.

5.2.1 Image Cropping

It is important that the whole lung area is captured by the segmentation method. Initially image cropping was done by selecting three landmarks, the midpoint of the seventh cervical vertebra (C7) and the extreme end points of the left and right lungs. The rectangle passing through these three points constitute the image to be studied.

5.2.2 Feature Vector Acquisition

Let $I(x,y)$ be the pixel intensity at the point (x,y). The first ten area moments are defined as follows (see also Section 2.4.3). Firstly,

$$\hat{\mu}_{pq}(I)=\sum_{x=0}^{N-1}\sum_{y=0}^{M-1}\left(\frac{x-\bar{x}}{\sigma_x}\right)^p\cdot\left(\frac{y-\bar{y}}{\sigma_y}\right)^q.\,I(x,y),$$

where $\sigma_x = \sqrt{\frac{\mu_{20}}{m_{00}}}$ and $\sigma_y = \sqrt{\frac{\mu_{02}}{m_{00}}}$. Finally, $\eta_{pq}(I) = \frac{\hat{\mu}_{pq}(I)}{\mu_{00}^{\alpha}(I)}$, where $\alpha = \frac{p+q}{2}+1$, are the area moments of interest. Note that these moments simultaneously perform translation, scaling and smoothing (Barbu et al., 2010).

The proposed feature vector for segmenting the whole image into a binary image is $V = (\eta_{00}, \eta_{01}, \eta_{10}, \eta_{02}, \eta_{11}, \eta_{20}, \eta_{03}, \eta_{12}, \eta_{21}, \eta_{30})$. Preliminary experiments have shown that the feature vector V is not sensitive enough to capture the ROI directly; henceforth V will be used to capture LG and BG only.

5.2.3 Extraction of Feature Vectors

Images of ten individuals, k = 1,2,…,10, were randomly selected from the NL data set. For each image, one hundred regions of size 16 x 16 pixels were selected randomly in which 50 regions were from the lungs (LG) and another 50 regions from the background area (BG). An illustration of selected regions is shown in Figure 5.1.

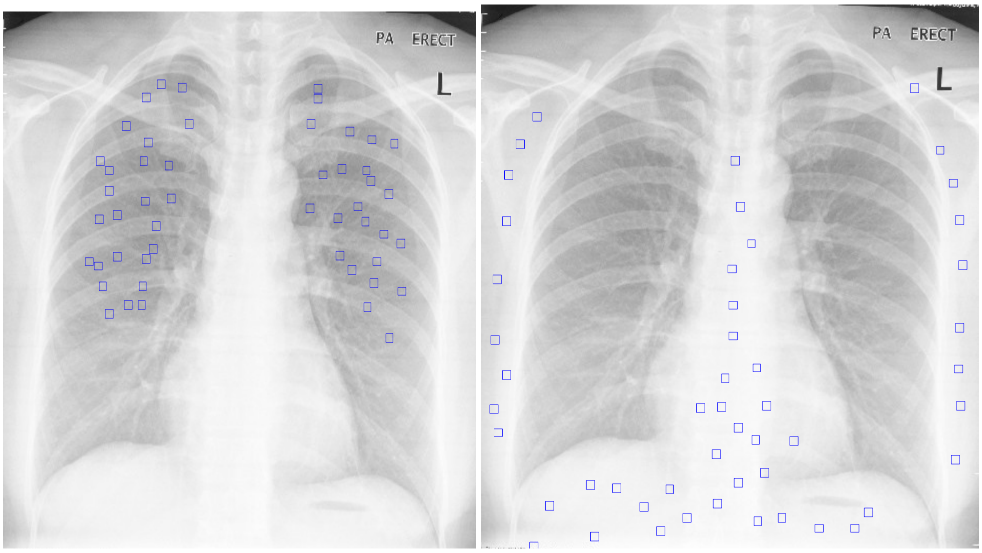

(a) (b)

Figure 5.1: Example of random selection sub-regions from (a) lung field, (b) non-lung field.

Given the i^{th} region (of size 16 x 16) in LG, the vector $V_i^{(LG)}$ is calculated. The average of these vectors is given by $\overline{V}_{LG(k)} = \frac{\sum_{i=1}^{50} V_i^{(LG)}}{50}$. Similarly the feature vector for the i^{th} region in BG, denoted by $V_i^{(BG)}$ is calculated and the corresponding average given by $\overline{V}_{BG(k)} = \frac{\sum_{i=1}^{50} V_i^{(BG)}}{50}$.

Averaging $\overline{V}_{LG(k)}$ and $\overline{V}_{BG(k)}$ over the ten individuals (k = 1,2,…,10), gives the feature vectors representing LG and BG, in particular, $\overline{\overline{V}}_{LG} = \frac{\sum_{k=1}^{10} V_{LG(k)}}{10}$ and $\overline{\overline{V}}_{BG} = \frac{\sum_{k=1}^{10} V_{BG(k)}}{10}$. These feature vectors are listed in Table 5.1.

Table 5.1: The feature vectors representing lung area and background.

	$\overline{\overline{V}}_{LG}$	$\overline{\overline{V}}_{BG}$
η_{00}	1.00	1.00
η_{10}	6.01E-05	6.58E-05
η_{10}	6.01E-05	6.50E-05
η_{02}	6.30E-09	4.35E-09
η_{11}	1.50E-08	1.16E-08
η_{20}	6.22E-09	4.34E-09
η_{03}	3.06E-12	2.86E-12
η_{12}	2.30E-12	1.87E-12
η_{21}	2.36E-12	1.96E-12
η_{30}	3.05E-12	2.90E-12

5.2.4 Binary Image

The chest radiograph for the eleven-th healthy individual was subdivided into a series of adjacent non-overlapping 16 x 16 regions. For the i^{th} region the vector of moments V_i was calculated. A nearest neighbour classification procedure was performed on the V_i (i = 1,2,..,w) such that if V_i is closest to $\overline{\overline{V}}_{LG}$ the i^{th} region is regarded as being within LG and the whole i^{th} region is assigned the pixel value one (white area). The value w depends on the size of the image. Similarly the BG region (black area) is identified when V_i is closest to $\overline{\overline{V}}_{BG}$.

An approximate method of investigating segmentation quality was carried out by overlaying the binary image with the original image and then a visual comparison was done. This exercise showed that for the majority of the cases the white region representing LG captured the whole lung area.

Five distance measures were investigated when the nearest neighbour procedure was conducted. These distance measures are,

1) Euclidean distance, $d_E(V,T) = \sqrt{\sum_{i=1}^{10} (v_i - t_i)^2}$,
2) City-block distance, $d_{CB}(V,T) = \sum_{i=1}^{10} |v_i - t_i|$,
3) Minkowski distance of order 3, $d_{M3}(V,T) = \sqrt[3]{\sum_{i=1}^{10} |v_i - t_i|^3}$,
4) Minkowski distance of order 4, $d_{M4}(V,T) = \sqrt[4]{\sum_{i=1}^{10} |v_i - t_i|^4}$,
5) Minkowski distance of order 5, $d_{M5}(V,T) = \sqrt[5]{\sum_{i=1}^{10} |v_i - t_i|^5}$.

where $V = \left(v_1, v_2, v_3, v_4, v_5, v_6, v_7, v_8, v_9, v_{10}\right)$ and $T = (t_1, t_2, t_3, t_4, t_5, t_6, t_7, t_8, t_9, t_{10})$.

An example of lung segmentation using these five distance measures is shown in Figure 5.2. Although the performance of lung segmentation using different distance measures on 10 normal lungs is look similar, however, visual segmentation evaluation generally obtains that the performance of the lung segmentation procedure using the Minkowski distance of order 3 shows better consistency in segmenting the lungs. All computational work was done in MATLAB environment.

(a) Original image (b) Euclidean distance (c) City-block distance

(d) Minkowski distance of order 3 (e) Minkowski distance of order 3 (f) Minkowski distance of order 3

Figure 5.2: Example of normal lung field segmentation using different distance measures.

The procedure of obtaining the binary image was repeated for 40 NL, 50 LC, 50 PNEU and 50 PTB cases using Minkowski distance of order 3. Figure 5.3 gives illustrations for ten NL cases. Similarly Figure 5.4, Figure 5.5 and Figure 5.6 illustrate ten LC cases, ten PNEU cases and ten PTB cases respectively.

No	Original image	Binary image
NL 1	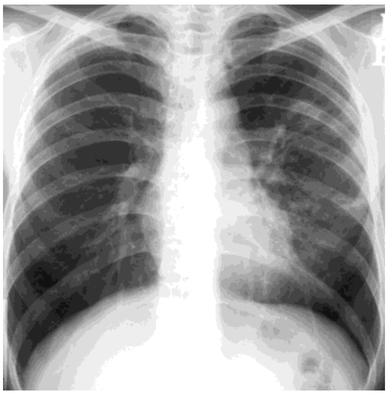	
NL 2	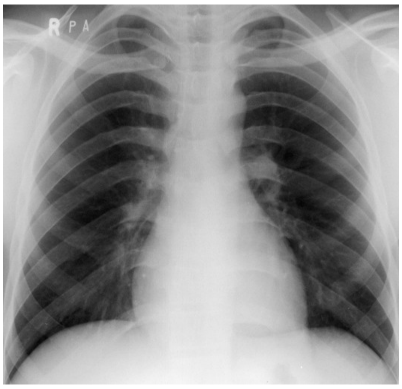	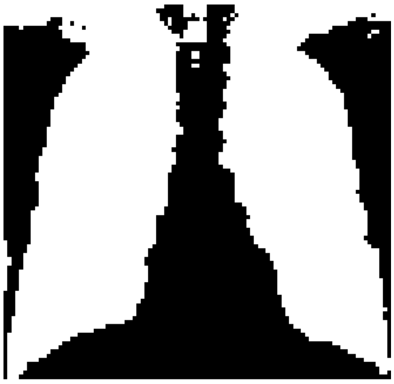
NL 3	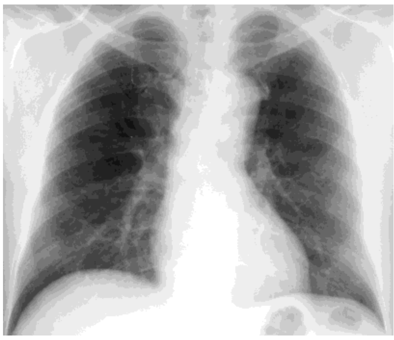	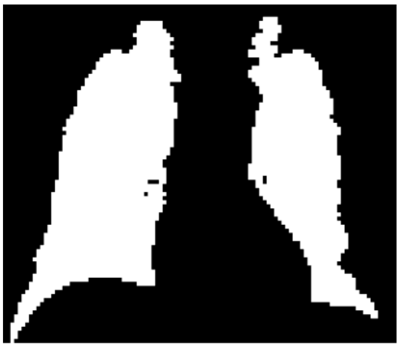
NL 4	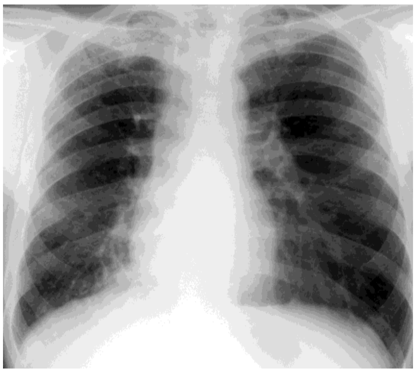	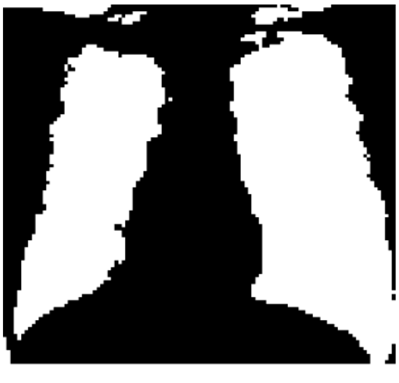

NL
5

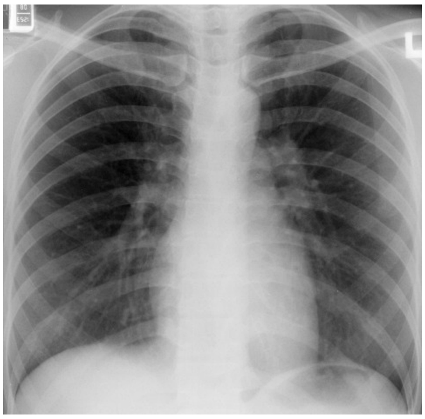

NL
6

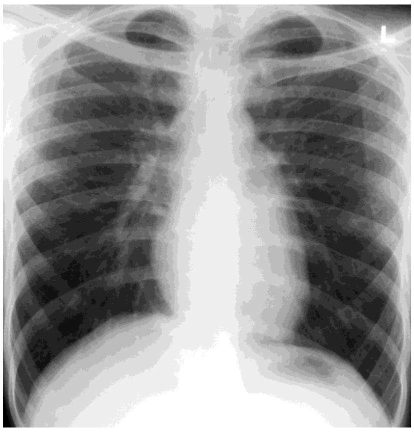

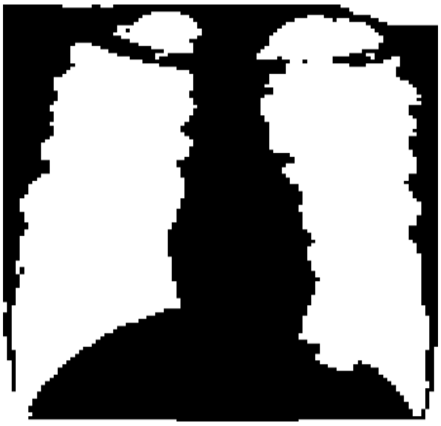

NL
7

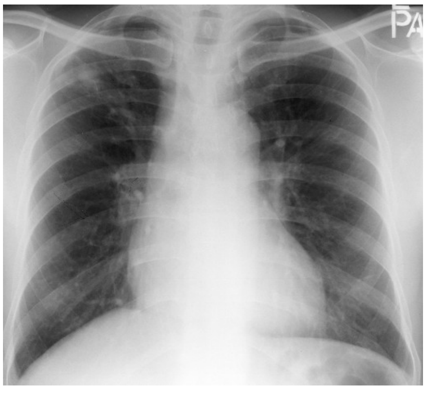

NL
8

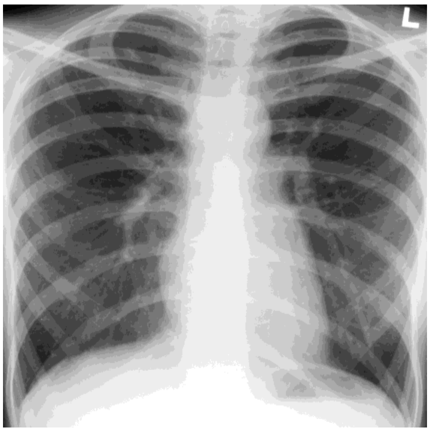

NL
9

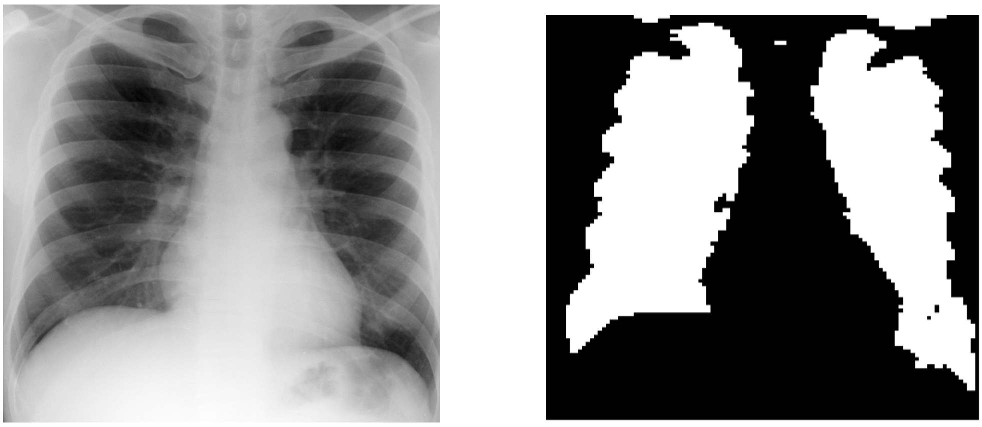

NL
10

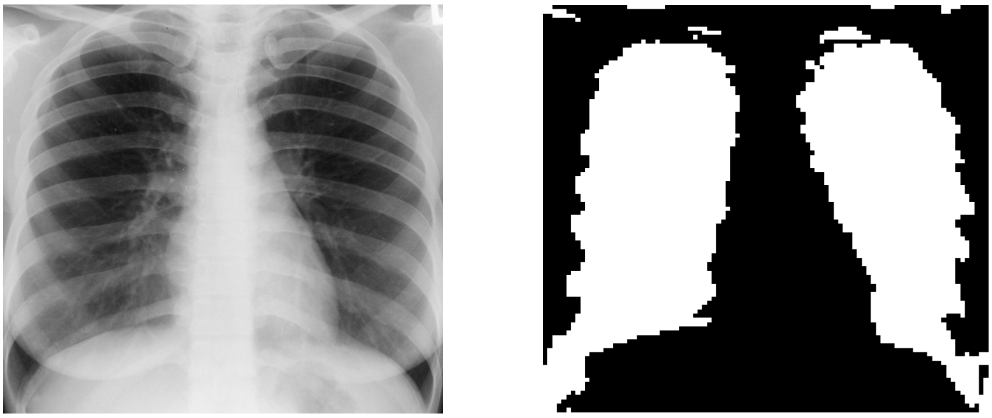

Figure 5.3: NL binary images.

Original image

Binary image

LC
1

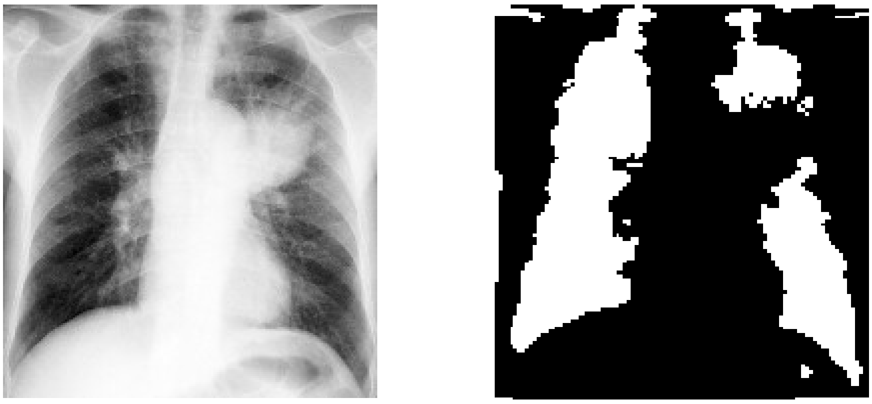

LC
2

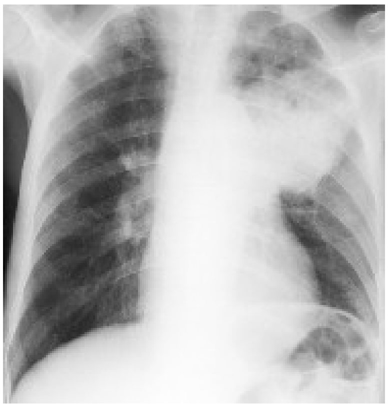

LC
3

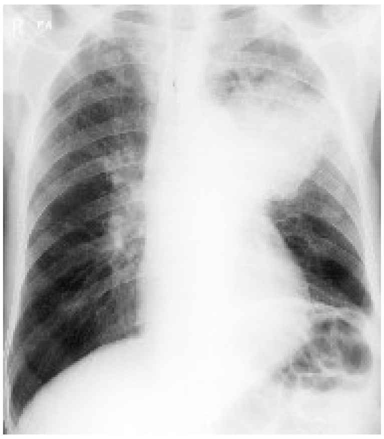

LC
4

LC
5

LC
6

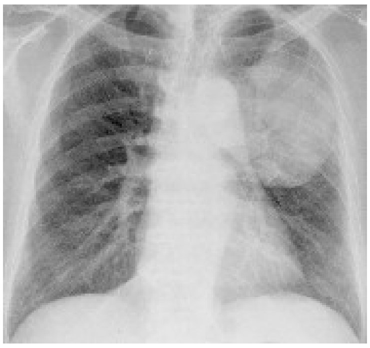

LC
7

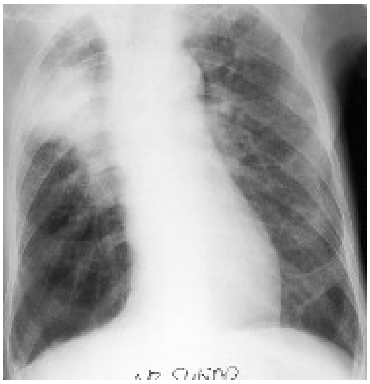

LC
8

LC
9

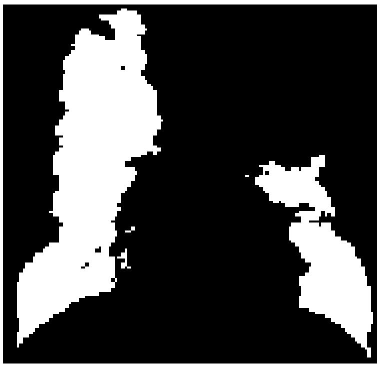

LC
10

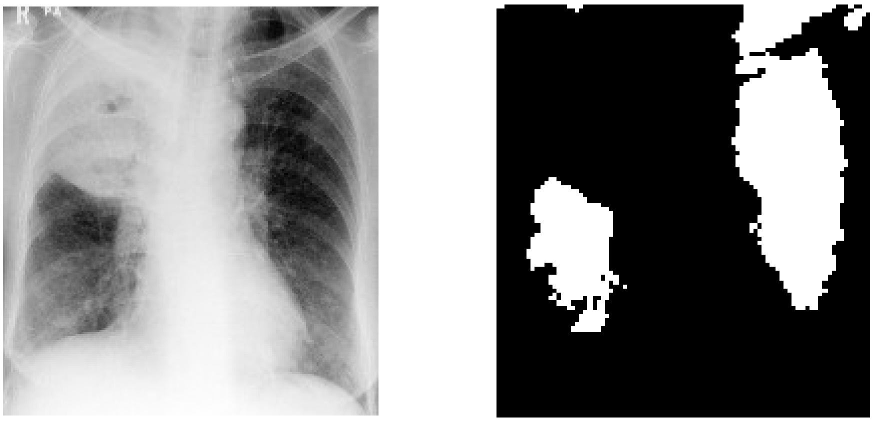

Figure 5.4: LC binary images.

Original image

Binary image

PNEU
1

PNEU
2

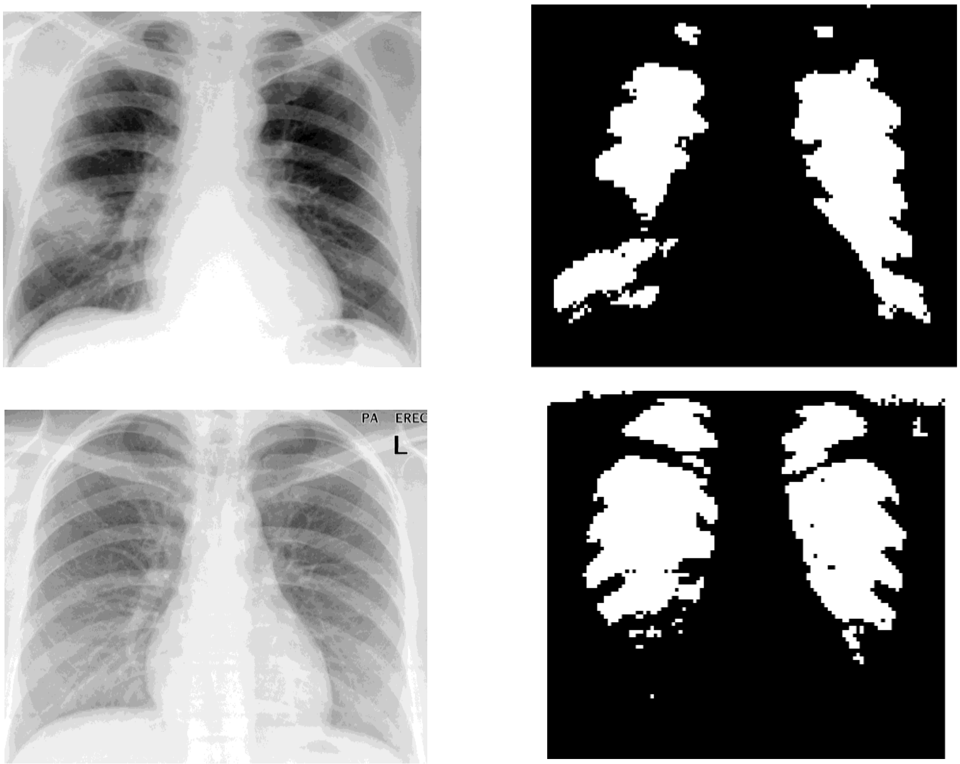

PNEU
3

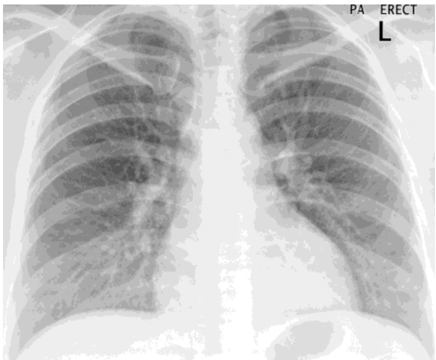

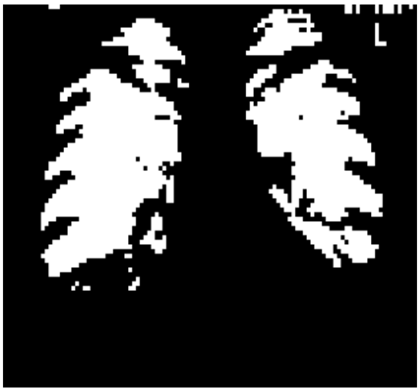

PNEU
4

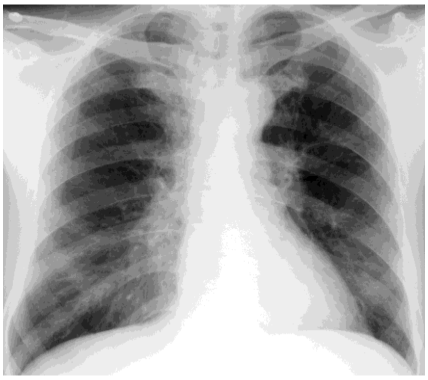

PNEU
5

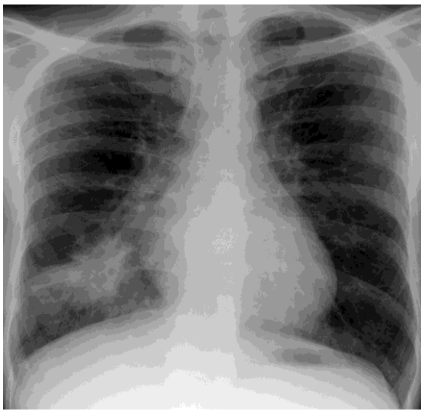

PNEU
6

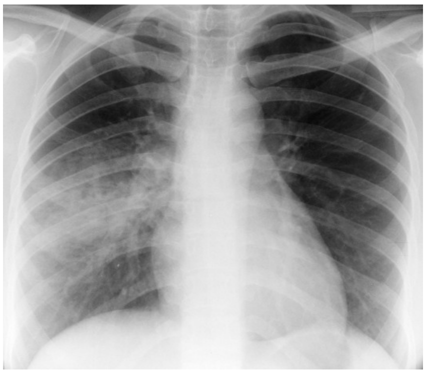

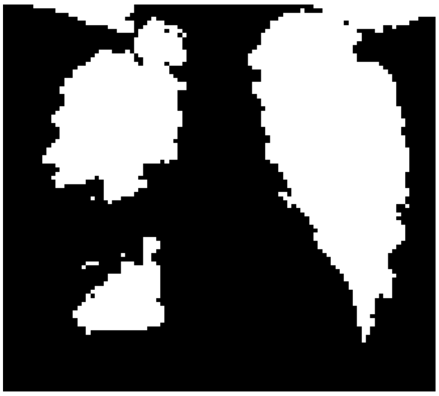

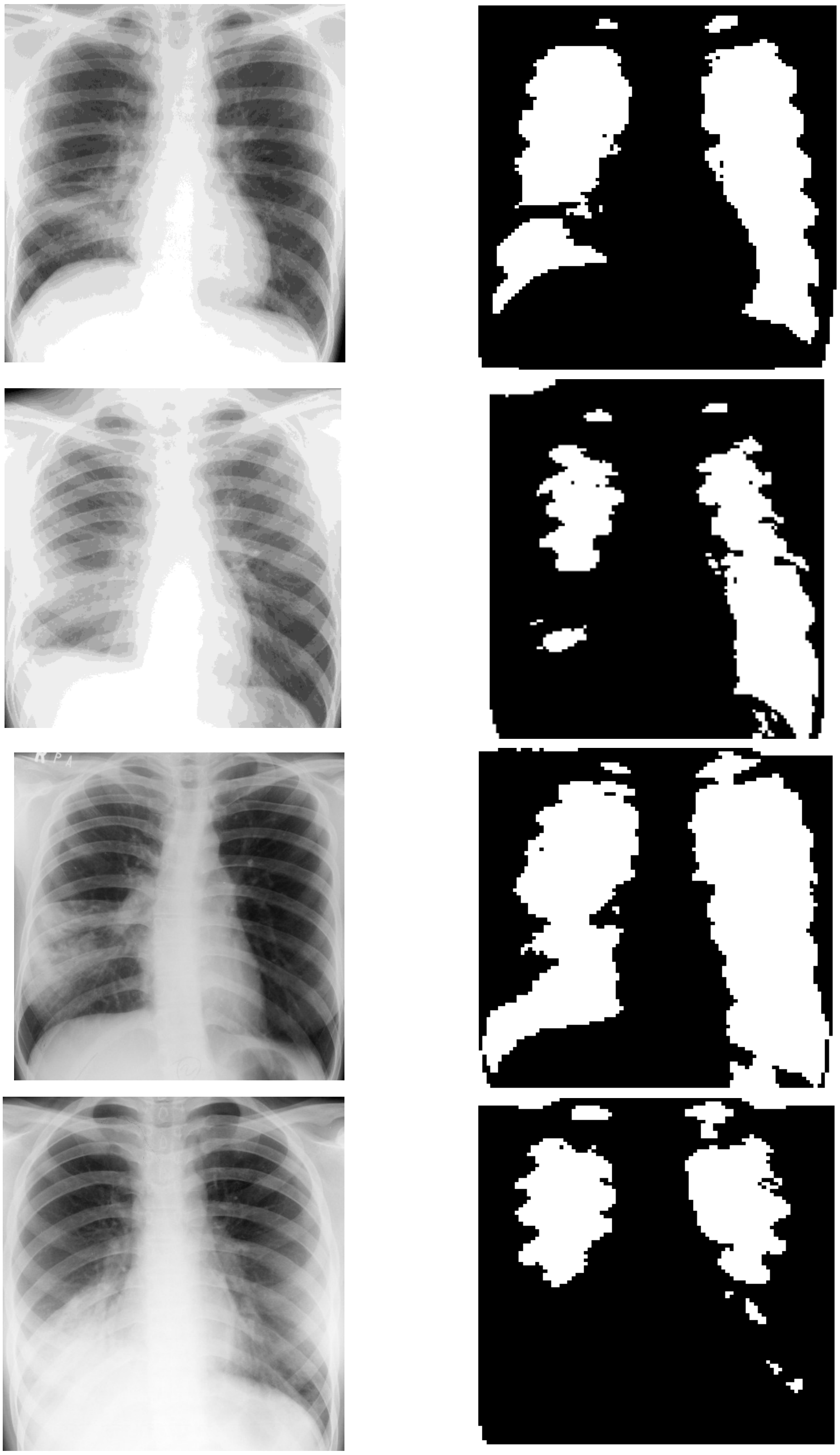

PNEU
7

PNEU
8

PNEU
9

PNEU
10

Figure 5.5: PNEU binary images.

No.	Original image	Binary image
PTB 1	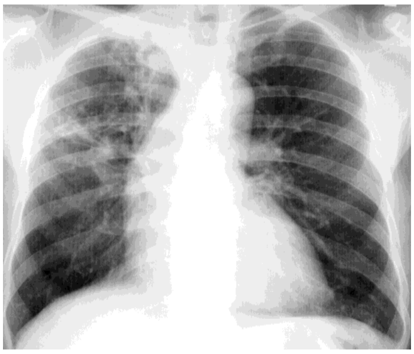	
PTB 2	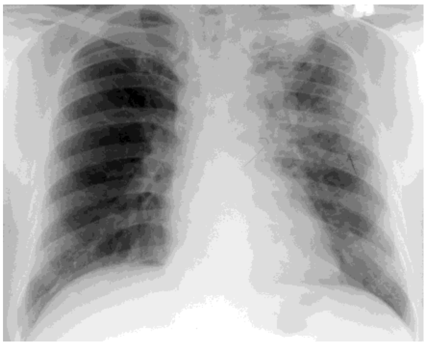	
PTB 3	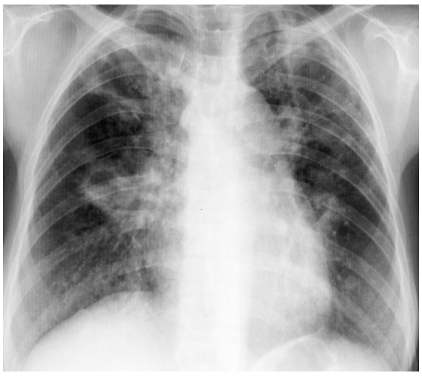	
PTB 4		

PTB
5

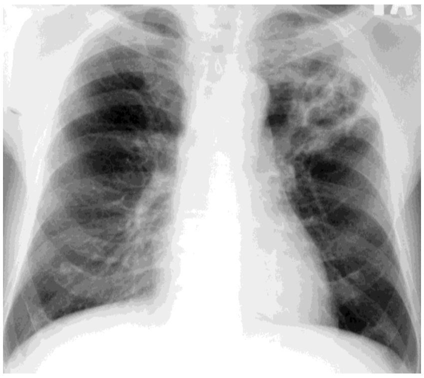

PTB
6

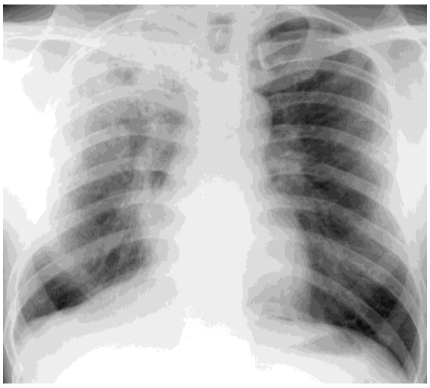

PTB
7

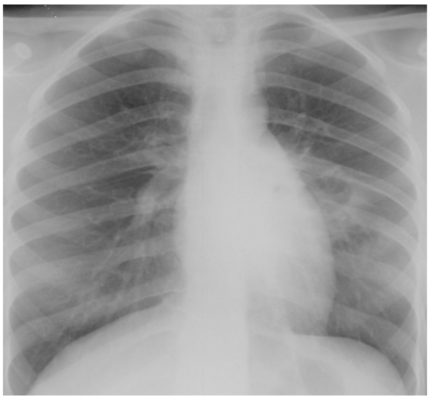

PTB
8

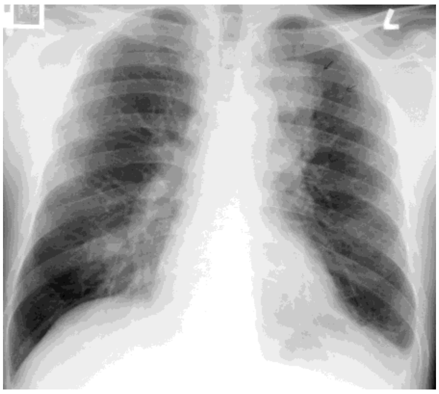

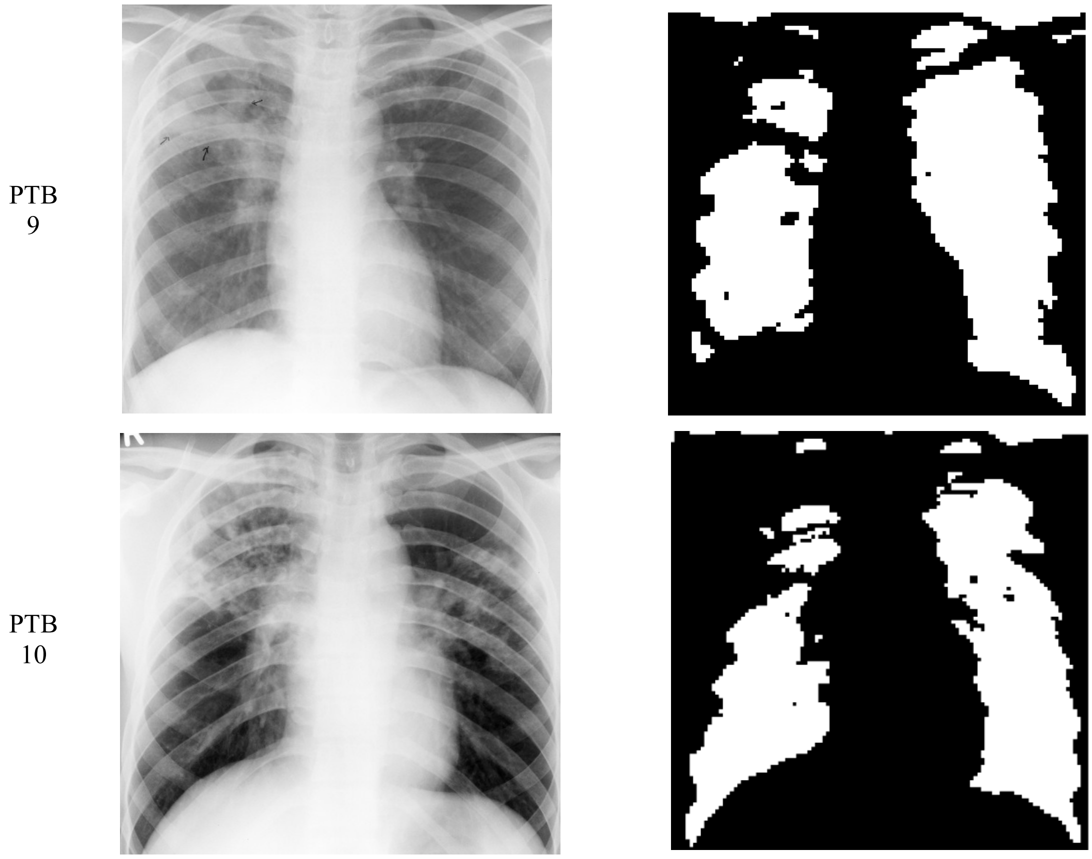

Figure 5.6: PTB binary images.

Binary images in Figure 5.4, Figure 5.5 and Figure 5.6 show that the ROI can be represented by the black region in LG. The ROI for lung cancer is usually located in the middle of LG and appears as a dense mass. The ROI for PNEU generally may be found in the lower parts of LG and is normally more dispersed. The ROI for PTB appears as snowflakes and usually affects the upper zones.

5.2.5 ROI Detection

Each binary image was divided into six rectangular regions, namely, left upper zone (LU), right upper zone (RU), left middle zone (LM), right middle zone (RM), left lower zone (LL) and right lower zone (RL). For a given pair of rectangular regions, say LU and RU, the ratio (R_1) of the number of white pixels in RU (N_{RU}) divided by the corresponding number of white pixels in LU (N_{LU}) should be close to one as is strongly suggested by the binary images for NL (see Figure 5.3). In the case of LG being infected, as seen by black spots in LG, the ratios R_2 and R_3 (see Table 5.2) will tend to be different from one. From a simulation study the range of R_1 , R_2 and R_3 was investigated and results are listed in Table 5.2. These ranges were validated by testing on the existing case studies

Table 5.2: The ratios R_1, R_2 and R_3 of the number of white pixels on right side upon left side of the lung.

	$R_1 = \frac{N_{RU}}{N_{LU}}$	$R_2 = \frac{N_{RM}}{N_{LM}}$	$R_3 = \frac{N_{RL}}{N_{LL}}$
Normal	$0.8 \leq R_1 \leq 1.4$	$0.8 \leq R_2 \leq 1.4$	$0.8 \leq R_3 \leq 1.4$
Infection on right side	$R_1 > 1.4$	$R_2 > 1.4$	$R_3 > 1.4$
Infection on left side	$R_1 < 0.8$	$R_2 < 0.8$	$R_3 < 0.8$

As an illustration in the selection of ROI, we consider using R_1. If $R_1 > 1.4$ then RU is infected, if $R_1 < 0.8$ then LU is infected. When $0.8 \leq R_1 \leq 1.4$, two situations occur, either both RU and LU are clear (healthy) or both are infected, as such the choice of ROI is done visually. In the case where R_1 is greater than 1.4 and R_2 is less than 0.8 either RU or LM may be chosen. This is done so that only one ROI is selected for every image.

CHAPTER 6

DISCRIMINATION OF LUNG DISEASES

6.1 Introduction

The detection of lung diseases such as lung cancer (LC), lobar pneumonia (PNEU) and pulmonary tuberculosis (PTB) using chest radiograph largely depends on visual interpretation. Since appearance of lung diseases on the chest X-ray does not conform to any standard shape, pattern, size and configuration, inexperience on the part of medical practitioner may lead to a wrong or delayed diagnosis. The problem is further complicated when signs and symptoms in initial stages can lead to incorrect diagnosis. However the chest radiograph is still widely used because of economic considerations and the fact that X-ray facilities are affordable.

There is a need to develop efficient discrimination procedures that could differentiate patients with a disease (disease-present) from individuals without the disease (disease-absent). For example, it is important to differentiate PNEU cases from NL cases.

An immediate problem is the choice of feature suitable for discrimination because the ROI for different diseases may appear to be similar. The large amount of information in the chest radiograph, for example, rib-bones, spine and organs strongly suggest creating features for discrimination that can extract meaningful information from adjacent pixels within a small region of the image. As such phase congruency will be explored as a possible candidate for a discrimination feature. Since phase congruency describes or provides information from adjacent pixels, ideas involving texture measures will also be applied as a global measure of information.

Optimal discriminant functions may be derived if the features have a normal probability distribution. In particular the well known linear discriminant function (LDF) and the quadratic discriminant function (QDF) will provide the best way of discriminating two categories of patients.

The traditional use of the LDF and QDF requires knowledge about misclassification costs and a prior probabilities which are usually unknown. This creates a problem concerning the choice of feature for discrimination. By considering all possible values of misclassification costs and a prior probabilities a receiver operating characteristics (ROC) analysis was carried out to help select the appropriate feature.

6.2 Phase Congruency Detects Rib-bones

Rib-bones in a given chest X-ray is brighter than other organs since X-rays do not penetrate into the rib-bones. Based on this property the boundaries of the rib-bones are clearly seen which results in a large transition of pixel values on rib-bone boundaries and their adjacent pixels. This result strongly motivates the use of phase congruency model to provide features for discrimination.

A one dimension line profile (1D-LP) was investigated to illustrate the PC-values on rib-bone boundaries. Ten randomly selected NL images were initially studied. For each image only one lung was cropped and the phase congruency transformation was carried out. One vertical column of pixels was studied for each of the ten NL cases where for each pixel position in the line profile, the PC-value was plotted (see Figure

6.1). Large transitions in PC-values are clearly seen at the boundaries of the rib-bones. Smaller but noticeable transitions in PC-values are seen for the lung tissue areas such that different tissue areas show different amounts of transitions.

NL
1

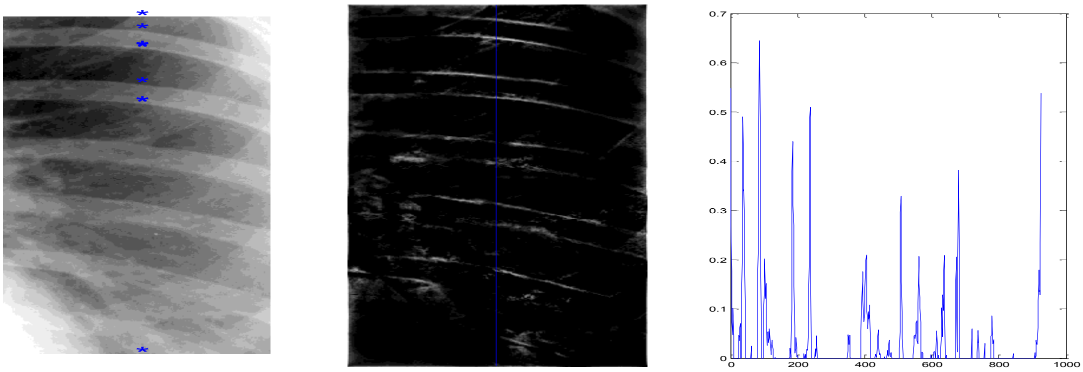

NL
2

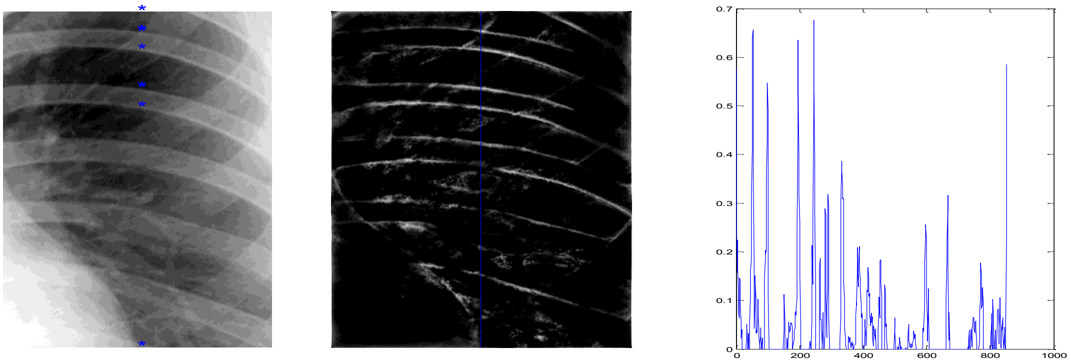

NL
3

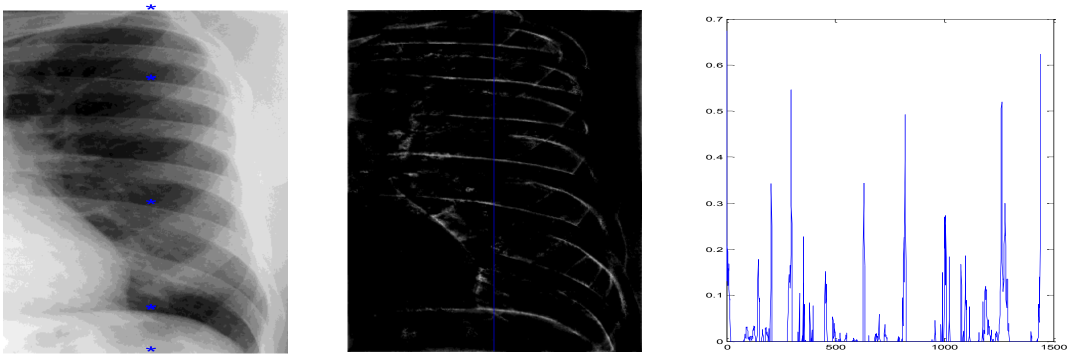

NL
4

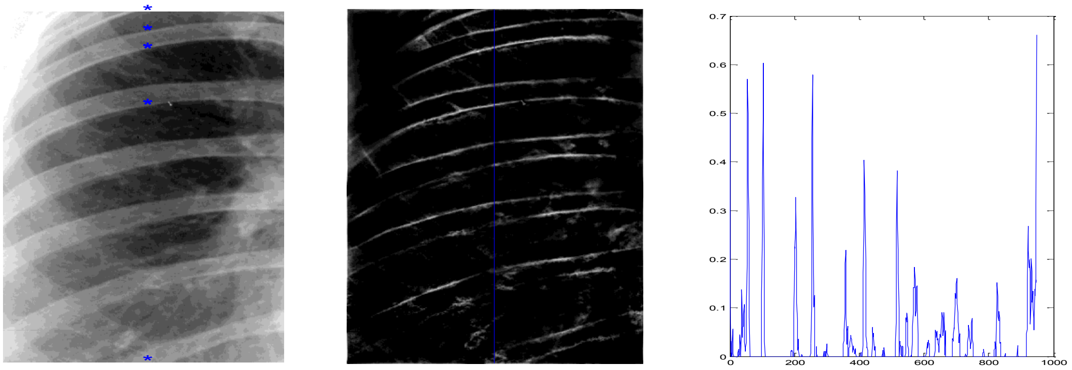

NL
5

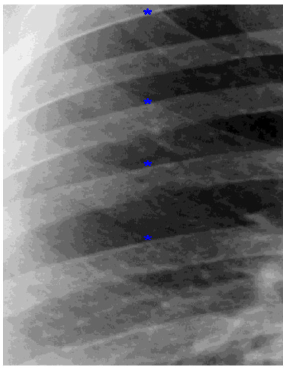

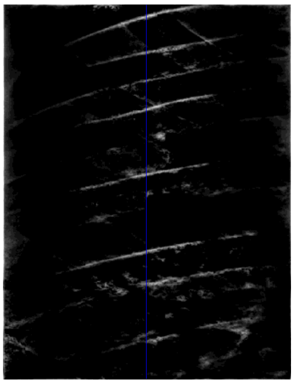

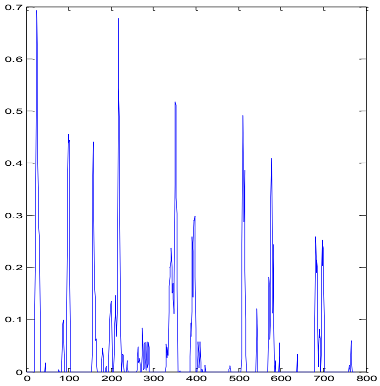

NL
6

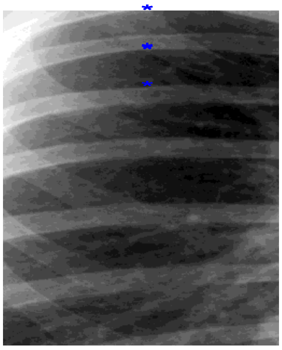

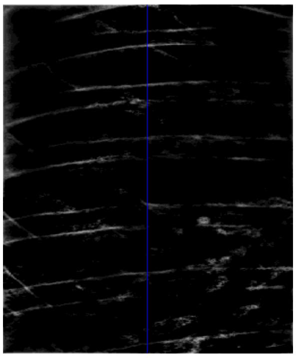

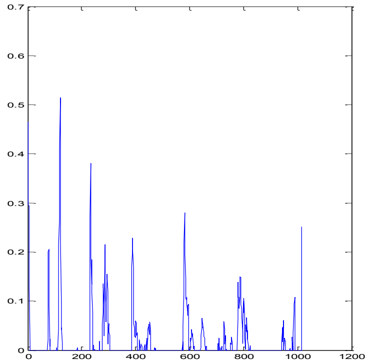

NL
7

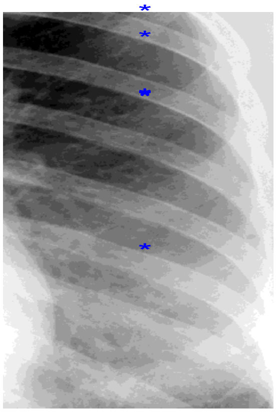

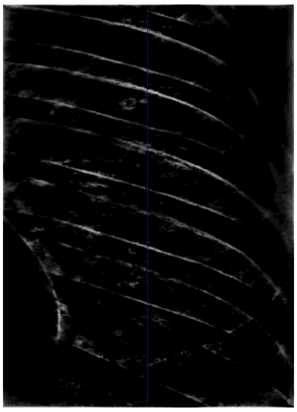

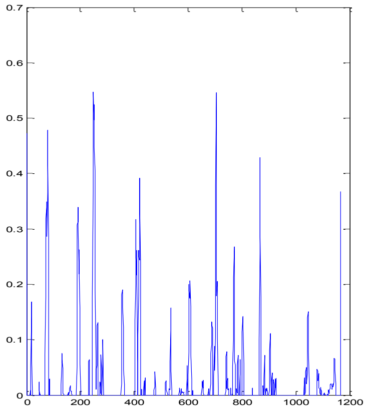

NL
8

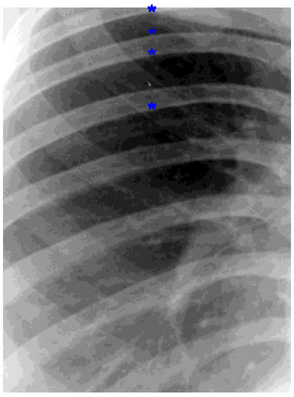

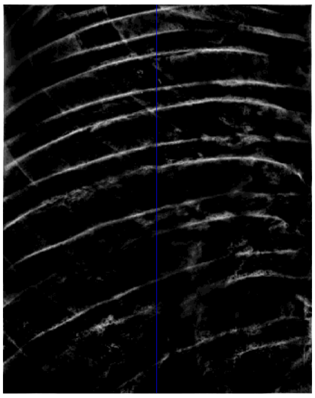

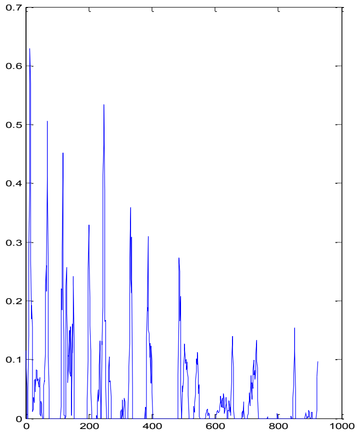

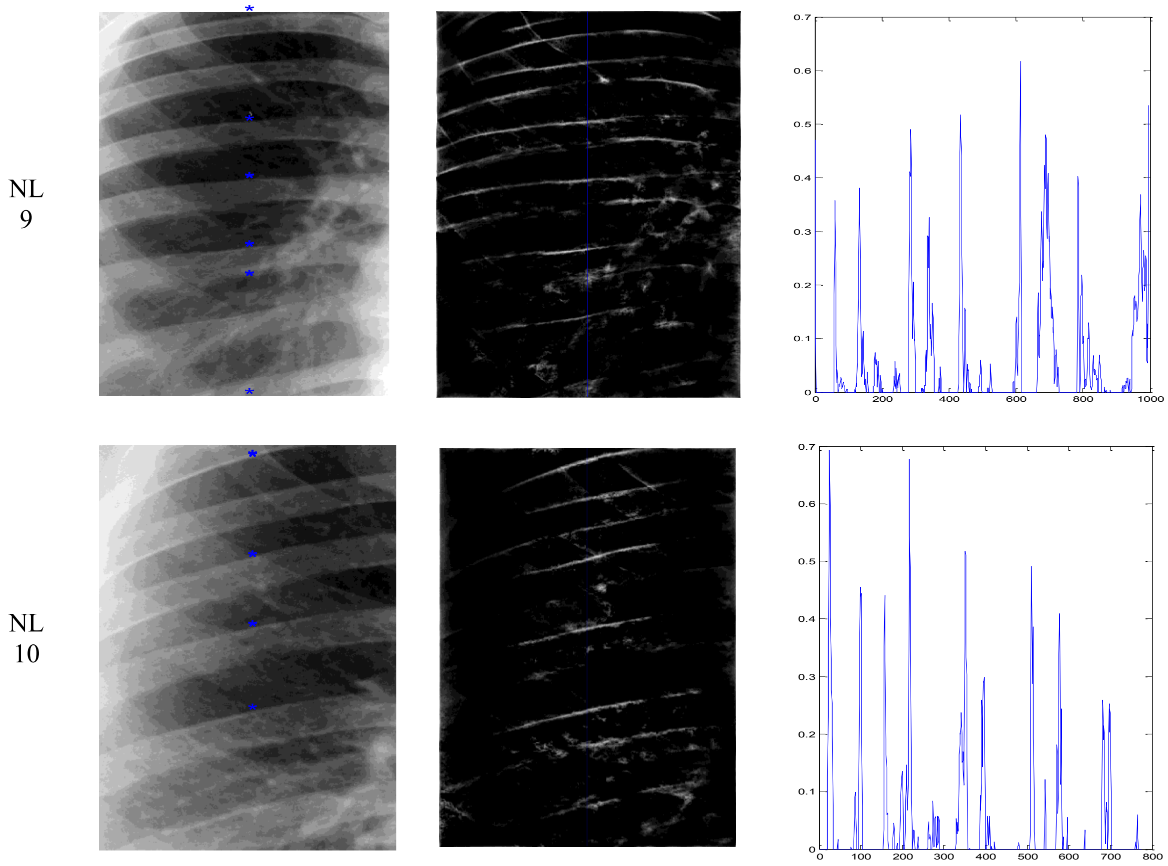

(a) (b) (c)

Figure 6.1: Region of interests in (a) original image, (b) phase congruency image and (c) 1-D line profiles of PC-values.

6.3 Using the Phase Congruency Values to Discriminate Lung Disease

The experiments in Section 6.1 was repeated by investigating ten random images were selected from each of the NL, LC, PNEU and PTB data sets. Results (Figure 6.2) show that PC-values in a given NL image is distinctly distributed from a given lung disease. The peaks of the LC one dimensional line profile appear to be sparse whilst the corresponding peaks for PNEU seems to be more spread out. Further the one dimensional line profile for PNEU and PTB appear similar. The 2D-line profile was also considered, but differences are harder to interpret. Examples of 1D-line profile and 2D-line profile for NL, LC, PNEU and PTB are given in Figure 6.2.

Type of image	Original image	Transformed image	1D-line profile	2D-line profile
NL	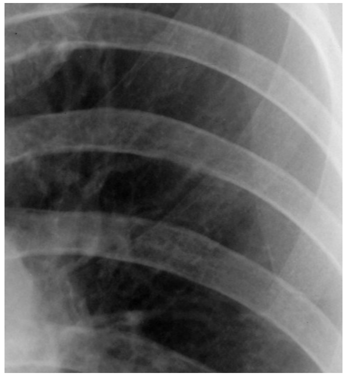	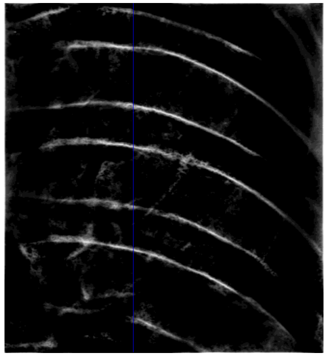	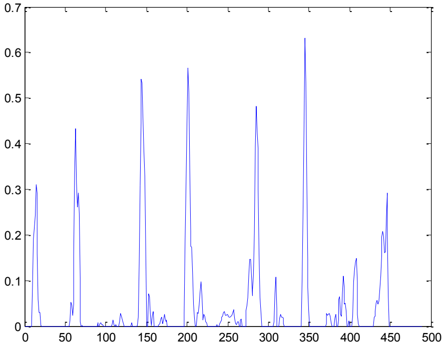	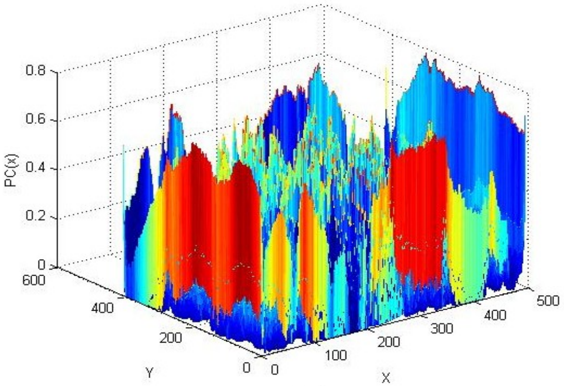
LC			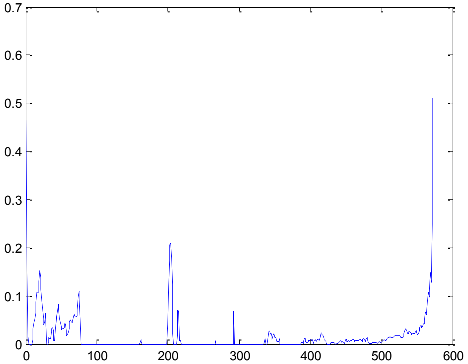	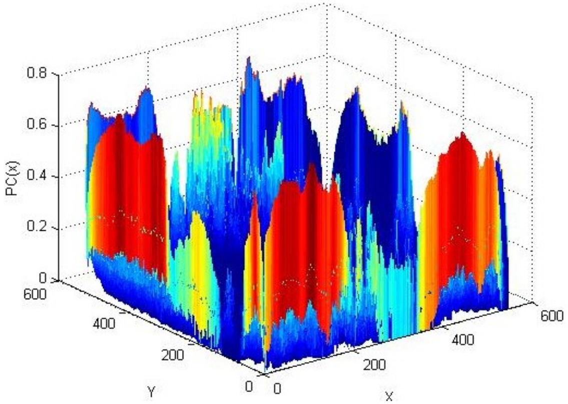

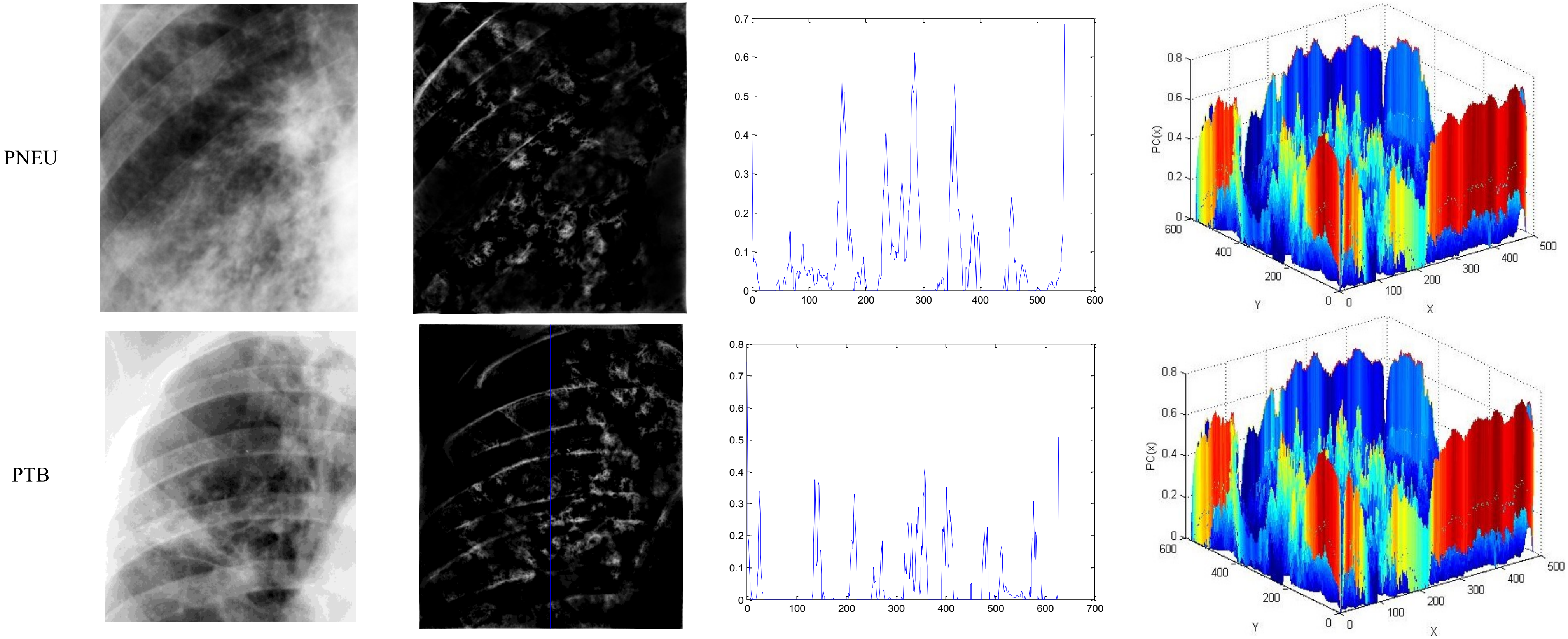

(a) (b) (c) (d)

Figure 6.2: Example of (a) original image, (b) phase congruency image, (c) 1D-line profile and (d) 2D-line profile for NL, LC, PNEU and PTB cases.

6.4 Image Features from Phase Congruency

For discriminating lung diseases using chest X-ray, PC-values alone are not sufficient to obtain meaningful image features since PC is carrying local information (information between adjacent pixels). To achieve good discrimination a global feature should be constructed and therefore summary statistics of PC-values and texture measures of PC-values are investigated.

6.4.1 Summary Statistics of Phase Congruency Values

Four summary statistics, namely, mean (μ), variance (σ^2), coefficient of variation (cv) and maximum value (M) were investigated where,

$$\mu = \frac{1}{N}\sum_i \sum_j \mathrm{PC}(x_{i,j}),$$

$$\sigma^2 = \frac{1}{N-1}\sum_i \sum_j (PC(x_{i,j}) - \mu)^2 \text{ , and}$$

$cv = \dfrac{\sigma}{\mu}$, where $\mathrm{PC}(x_{i,j})$ is the phase congruency value at the (*i*,*j*) pixel position and *N* obtains the number of pixels.

The use of maximum value (*M*) is motivated from the previous section whereby the *M* values for NL cases is generally larger than the diseases cases. The average of summary statistics for control group (20 NL, 25 LC, 25 PNEU and 25 PTB) is listed in Table 6.1.

Table 6.1: Summary statistics of PC-values for NL, LC, PNEU and PTB cases.

Summary statistics	NL	LC	PNEU	PTB
μ	0.04635	0.0306	0.0290	0.0385
σ^2	0.0094	0.0059	0.0058	0.0070
cv	2.1262	2.7109	2.6894	2.2591
M	0.8007	0.8011	0.7828	0.7901

6.4.2 Testing the Features

Let $C^T = \left(\mu, \sigma^2, cv, M\right) = (c_1, c_2, c_3, c_4)$ be the feature vector from the control group taken from Table 6.1. From the test group (20 NL, 25 LC, 25 PNEU and 25 PTB) the corresponding feature vector $T^T = \left(\mu, \sigma^2, cv, M\right) = (t_1, t_2, t_3, t_4)$ was calculated.

Seven distance measures investigate the similarity between the *C*-vector and the *T*-vector, namely,

1) Euclidean distance $d_E(C,T) = \sqrt{\sum_{i=1}^{4} \left(c_i - t_i\right)^2}$,

2) Minkowski distance of order 3 $d_{M3}(C,T) = \sqrt[3]{\sum_{i=1}^{4} \left|c_i - t_i\right|^3}$,

3) Minkowski distance of order 4 $d_{M4}(C,T) = \sqrt[4]{\sum_{i=1}^{4} \left|c_i - t_i\right|^4}$,

4) Minkowski distance of order 5 $d_{M5}(C,T) = \sqrt[5]{\sum_{i=1}^{4} \left|c_i - t_i\right|^5}$,

5) Chebyshev distance $d_{CH}(C,T) = \max_i \left\{\left|c_i - t_i\right|\right\}$,

6) City-block distance $d_{CB}(C,T) = \sum_{i=1}^{4} \left|c_i - t_i\right|$ and

7) Mahalanobis distance $d_{Mahal}(C,T)=\sqrt{(C-T)S^{-1}(C-T)^{T}}$ where S is covariance matrix.

A nearest neighbour classification method assigns the observation, *T*, to the NL group if the distance between *T* and $C_{(NL)}$ is smallest compared to the distance between *T* and the other *C*-vectors. Results are given in Table 6.2.

Table 6.2: The probability of misclassifications using nearest neighbour method .

	Euclidean	**Minkowski of order 3**	**Minkowski of order 4**	**Minkowski of order 5**	**Chebyshev**	**City-block**	**Mahalanobis**
NL, LC	0.2400	0.2400	0.2400	0.2400	0.2800	0.2200	0.1800
NL, PNEU	0.2200	0.2200	0.2200	0.2200	0.2200	0.2000	0.2000
NL, PTB	0.4000	0.4000	0.4000	0.4000	0.4400	0.3800	0.2200
LC, PNEU	0.5000	0.5000	0.5000	0.5000	0.5200	0.4600	0.3200
LC, PTB	0.3400	0.3400	0.3400	0.3400	0.3400	0.3400	0.2600
PNEU, PTB	0.3200	0.3200	0.3200	0.3200	0.3400	0.3000	0.2600

Results in Table 6.2 show that the Mahalanobis distance gives the smallest misclassification rates. However, this misclassification rates are relatively large suggesting that the summary statistics of PC-values are not suitable features for discrimination.

6.4.3 Texture Measures from Phase Congruency

Since the summary statistics of PC-values does not seem to have good discrimination properties another global measure, namely texture measures of PC-values, will be explored. This section considers eight different texture measures, namely, energy (*E*), mean-energy $(\overline{E})$, entropy (*En*), contrast (*C*), homogeneity (*H*), standard deviation of value (*STDV*), standard deviation of energy (*STDE*) and correlation (*Corr*) where,

1) $E = \sum_j \sum_k \left|P_{jk}\right|^2$,

2) $\overline{E} = \frac{1}{N} \sum_j \sum_k \left|P_{jk}\right|^2$,

3) $En = -\frac{1}{N^2} \sum_j \sum_k \left|P_{jk}\right|^2 \log\left|P_{jk}\right|^2$,

4) $C = \sum_j \sum_k (j-k)^2 P_{jk}$,

5) $H = \sum_j \sum_k \frac{P_{jk}}{1+|j-k|}$,

6) $STDV = \sqrt{\frac{1}{N^2} \sum_j \sum_k \left(P_{jk} - \mu\right)^2}$ where $\mu = \frac{1}{N^2} \sum_j \sum_k P_{jk}$,

7) $STDE = \sqrt{\frac{1}{N^2} \sum_j \sum_k \left(P_{jk}^2 - \mu^{(2)}\right)^2}$ where $\mu^{(2)} = \frac{1}{N^2} \sum_j \sum_k \left|P_{jk}\right|^2$, and

8) $Corr = \sum_j \sum_k \frac{\left(j-\mu_j\right)\left(k-\xi_k\right)P_{jk}}{\sigma_j \tau_k}$,

where P_{jk} indicates the PC-value of pixel x in j^{th}-row and k^{th}-column, μ_j and σ_j denote mean and variance of PC-values along the j^{th}-row; ξ_k and τ_k denote mean and variance along the k^{th}-column.

The texture measures for 20 NL, 25 LC, 25 PNEU and 25 PTB cases are given in Table 6.3 to Table 6.6.

Table 6.3: Texture measures of images from normal lung control group.

	E	$\overline{E}$	E_n	C	H	*STDV*	*STDE*	*Corr*
NL1	2478.79	0.0111	4.0143	421600773	229.1276	0.0005	0.0005	1
NL2	2793.88	0.0132	3.7225	372678518	235.806	0.0005	0.0005	1
NL3	1670.52	0.0066	3.2483	368510204	156.964	0.0003	0.0003	1
NL4	2890.79	0.0119	4.0878	513240914	246.6743	0.0004	0.0004	1
NL5	2258.15	0.0121	3.7689	297894453	205.7436	0.0005	0.0005	1
NL6	2169.06	0.0099	3.4259	333826873	193.3132	0.0004	0.0004	1
NL7	3112.1	0.0138	3.9831	478488065	256.0414	0.0005	0.0005	1
NL8	3190.46	0.0126	3.9326	553968772	259.059	0.0004	0.0004	1
NL9	3207.9	0.0138	3.9511	487816227	263.8483	0.0005	0.0005	1
NL10	2907.51	0.0126	3.9855	469385371	243.435	0.0005	0.0005	1
NL11	3491.27	0.0169	4.3207	478900728	299.3897	0.0006	0.0006	1
NL12	2299.43	0.0081	3.5415	551773939	191.2927	0.0004	0.0004	1
NL13	2332.27	0.0093	3.8731	524966018	219.1857	0.0004	0.0004	1
NL14	2572.32	0.0126	3.8231	335406902	232.2943	0.0005	0.0005	1
NL15	2891.37	0.0125	3.9577	472088656	239.0308	0.0005	0.0005	1
NL16	1793.88	0.0074	2.9247	362908147	137.7493	0.0003	0.0003	1
NL17	1646.93	0.0062	3.3781	543208513	125.4001	0.0003	0.0003	1
NL18	2946.92	0.0106	3.7722	598952614	235.6558	0.0004	0.0004	1
NL19	3482.42	0.0146	4.0639	563583497	273.5938	0.0005	0.0005	1
NL20	1651.44	0.0072	2.9281	357912970	131.2023	0.0004	0.0004	1

Table 6.4: Texture measures of images from lung cancer control group.

	E	$\overline{E}$	E_n	C	H	$STDV$	$STDE$	$Corr$
LC1	561.47	0.0028	0.8671	93501769	39.8743	0.0002	0.0002	1
LC2	612.84	0.0049	2.4667	61747390	79.3585	0.0004	0.0004	1
LC3	852.96	0.0041	1.7908	154450076	59.5266	0.0003	0.0003	1
LC4	962.8	0.003	1.87	283784018	86.3467	0.0002	0.0002	1
LC5	789.15	0.0038	2.1925	139139044	81.9455	0.0003	0.0003	1
LC6	993.57	0.0032	1.8944	293431727	86.1227	0.0002	0.0002	1
LC7	371.16	0.0033	1.434	34280477	44.003	0.0004	0.0004	1
LC8	422.99	0.007	3.0713	33066713	31.4466	0.0006	0.0006	1
LC9	396.51	0.0048	1.9346	27272238	49.811	0.0005	0.0005	1
LC10	686.25	0.0073	2.6217	39730147	68.1345	0.0005	0.0005	1
LC11	654.57	0.0072	3.0735	53244998	84.6822	0.0006	0.0006	1
LC12	550.58	0.0059	2.8946	52535170	80.571	0.0006	0.0006	1
LC13	746.72	0.0055	1.7318	74150349	71.8408	0.0004	0.0004	1
LC14	450.49	0.0042	1.8791	42893866	56.0924	0.0004	0.0004	1
LC15	990.06	0.0075	3.3979	117877718	93.9077	0.0005	0.0005	1
LC16	442.81	0.0047	0.9898	27756501	35.2873	0.0004	0.0004	1
LC17	451.53	0.0047	1.1329	23902619	42.5969	0.0004	0.0004	1
LC18	428.5	0.0053	1.4336	18201063	37.4635	0.0004	0.0004	1
LC19	675.46	0.0066	2.4431	54211868	54.3318	0.0005	0.0005	1
LC20	408.38	0.008	2.7121	34984123	25.0989	0.0007	0.0007	1
LC21	543.73	0.0056	2.3269	33052329	55.498	0.0004	0.0004	1
LC22	580.18	0.0064	2.9663	43471206	68.1419	0.0005	0.0005	1
LC23	1038.58	0.009	3.5086	90506629	103.9588	0.0005	0.0005	1
LC24	980.98	0.007	3.4892	119662285	114.7136	0.0005	0.0005	1
LC25	546.64	0.0075	3.1748	51157867	38.8481	0.0006	0.0006	1

Table 6.5: Texture measures of images from lobar pneumonia control group.

	E	$\overline{E}$	E_n	C	H	*STDV*	*STDE*	*Corr*
PNEU1	866.62	0.0079	3.3865	90228239	94.2182	0.0006	0.0006	1
PNEU2	795.25	0.0101	3.7241	62759219	83.5969	0.0007	0.0007	1
PNEU3	802.06	0.0073	3.2703	87687014	87.0323	0.0005	0.0005	1
PNEU4	913.6	0.0051	2.0996	131208418	68.8852	0.0003	0.0003	1
PNEU5	945.31	0.0056	2.4475	131376257	72.1198	0.0004	0.0004	1
PNEU6	1371	0.0114	3.9601	136448791	155.5329	0.0006	0.0006	1
PNEU7	1183.88	0.0098	3.5867	117152673	101.6385	0.0006	0.0006	1
PNEU8	1013.84	0.0076	4.2096	141059482	127.4333	0.0005	0.0005	1
PNEU9	463.95	0.0053	3.3007	34558216	60.9712	0.0005	0.0005	1
PNEU10	802.45	0.0037	1.7459	126576060	63.4957	0.0003	0.0003	1
PNEU11	1049.19	0.0066	2.5874	126777969	118.9385	0.0004	0.0004	1
PNEU12	1056.79	0.0072	3.236	126737117	103.3734	0.0004	0.0004	1
PNEU13	945.98	0.0064	2.7788	130291772	93.9954	0.0004	0.0004	1
PNEU14	557.16	0.0052	2.6398	53070588	78.2882	0.0005	0.0005	1
PNEU15	1135.76	0.0071	2.5595	145583738	121.9111	0.0004	0.0004	1
PNEU16	1292.41	0.0078	3.6261	184571059	131.1874	0.0005	0.0005	1
PNEU17	1226.8	0.0061	3.2772	205472784	122.3775	0.0004	0.0004	1
PNEU18	946.4	0.0099	4.057	73728994	127.0429	0.0007	0.0007	1
PNEU19	846.54	0.0068	2.7848	85721007	90.7847	0.0005	0.0005	1
PNEU20	1388.35	0.0092	4.0661	166901162	144.7077	0.0005	0.0005	1
PNEU21	889.68	0.0069	2.8249	83841524	80.9133	0.0004	0.0004	1
PNEU22	890.4	0.0072	3.4395	98516442	89.8996	0.0005	0.0005	1
PNEU23	635.01	0.005	2.5416	67346652	65.447	0.0004	0.0004	1
PNEU24	767.41	0.0052	2.4719	90440385	65.8973	0.0004	0.0004	1
PNEU25	855.3	0.0096	3.7034	58216798	98.6711	0.0006	0.0006	1

Table 6.6: Texture measures of images from pulmonary tuberculosis control group.

	E	$\overline{E}$	E_n	C	H	$STDV$	$STDE$	$Corr$
PTB1	1096.0809	0.0061	3.296	80325678	125.3171	0.0002	0.0001	1
PTB2	1388.1971	0.0046	2.2709	221028371	106.0734	0.0001	0.0001	1
PTB3	1415.9968	0.0073	3.2526	322837661	162.4253	0.0002	0.0001	1
PTB4	1461.4417	0.0052	2.47	327599395	122.9492	0.0001	0.0001	1
PTB5	1447.2907	0.0092	3.4157	403800612	116.7478	0.0002	0.0001	1
PTB6	1480.4167	0.0086	3.7219	226052811	122.0034	0.0002	0.0001	1
PTB7	1355.5881	0.0104	4.2012	158690739	121.8359	0.0003	0.0001	1
PTB8	1474.4433	0.0067	3.8276	358876890	131.2368	0.0002	0.0001	1
PTB9	1602.4631	0.0069	4.1531	326260063	113.2542	0.0002	0.0001	1
PTB10	1547.4256	0.0084	3.5452	256329412	164.2382	0.0002	0.0001	1
PTB11	1015.3688	0.0081	3.4962	167329621	152.5717	0.0002	0.0001	1
PTB12	1399.8012	0.0084	3.3765	64052649	115.3394	0.0003	0.0001	1
PTB13	1449.9891	0.0064	3.6945	200834261	121.0079	0.0002	0.0001	1
PTB14	1166.5822	0.0097	3.6898	329881758	122.5032	0.0002	0.0001	1
PTB15	1491.4581	0.0051	2.9291	377564937	145.8418	0.0001	0.0001	1
PTB16	1412.9841	0.0043	2.2205	161262935	114.1948	0.0001	0.0001	1
PTB17	1322.8442	0.0075	3.2999	192071178	142.6932	0.0002	0.0001	1
PTB18	1706.1364	0.0071	2.9111	158381897	135.3506	0.0002	0.0001	1
PTB19	1362.1511	0.0068	3.0766	152037083	101.4989	0.0002	0.0001	1
PTB20	1459.5166	0.0099	3.8179	191654383	147.3872	0.0003	0.0001	1
PTB21	1442.3578	0.0102	3.5819	54606746	123.8992	0.0003	0.0001	1
PTB22	2264.6557	0.0081	3.0629	191568893	123.9984	0.0002	0.0001	1
PTB23	1480.4167	0.0086	3.7219	226052811	112.0034	0.0002	0.0001	1
PTB24	1466.5822	0.0097	3.6898	329881758	142.5032	0.0002	0.0001	1
PTB25	1674.4433	0.0067	3.8276	358876890	129.2368	0.0002	0.0001	1

The mean and the standard deviation (STD) of each texture measures for NL, LC, PNEU and PTB is listed in Table 6.7.

Table 6.7: Mean and standard deviation of texture measures of PC-values.

	NL		**LC**		**PNEU**		**PTB**	
	Mean	**STD**	**Mean**	**STD**	**Mean**	**STD**	**Mean**	**STD**
E	2589.3705	597.1459	622.44	209.0627	980.167	244.6032	1455.39	228.44
$\overline{E}$	0.01115	0.002922	0.00519	0.00163	0.007305	0.001975	0.0076	0.0017
E_n	3.735155	0.380289	2.091575	0.728778	3.167185	0.690677	3.3820	0.5212
C	454355608	91011404	83008094	80083330	1.18E+08	43384024	2.3E+08	100818509
H	218.74035	48.96611	60.4221	21.62488	102.3765	27.57205	128.644	16.6215
STDV	0.00044	8.21E-05	0.000425	0.000141	0.000485	0.000114	0.0002	5.7735E-05
STDE	0.00044	8.21E-05	0.000425	0.000141	0.000485	0.000114	0.0001	1.3832E-20
Corr	1	0	1	0	1	0	1	0

To illustrate the capability of a given texture measure to show differences in the different categories of interest, box-plots (one each for NL, LC, PNEU and PTB) for a given texture measures is given in Figure 6.3. One important result is that the texture measures energy, contrast and homogeneity can individually discriminate NL cases from the three diseases categories. Another important result is that the texture measure energy appears to be able to discriminate PTB from LC.

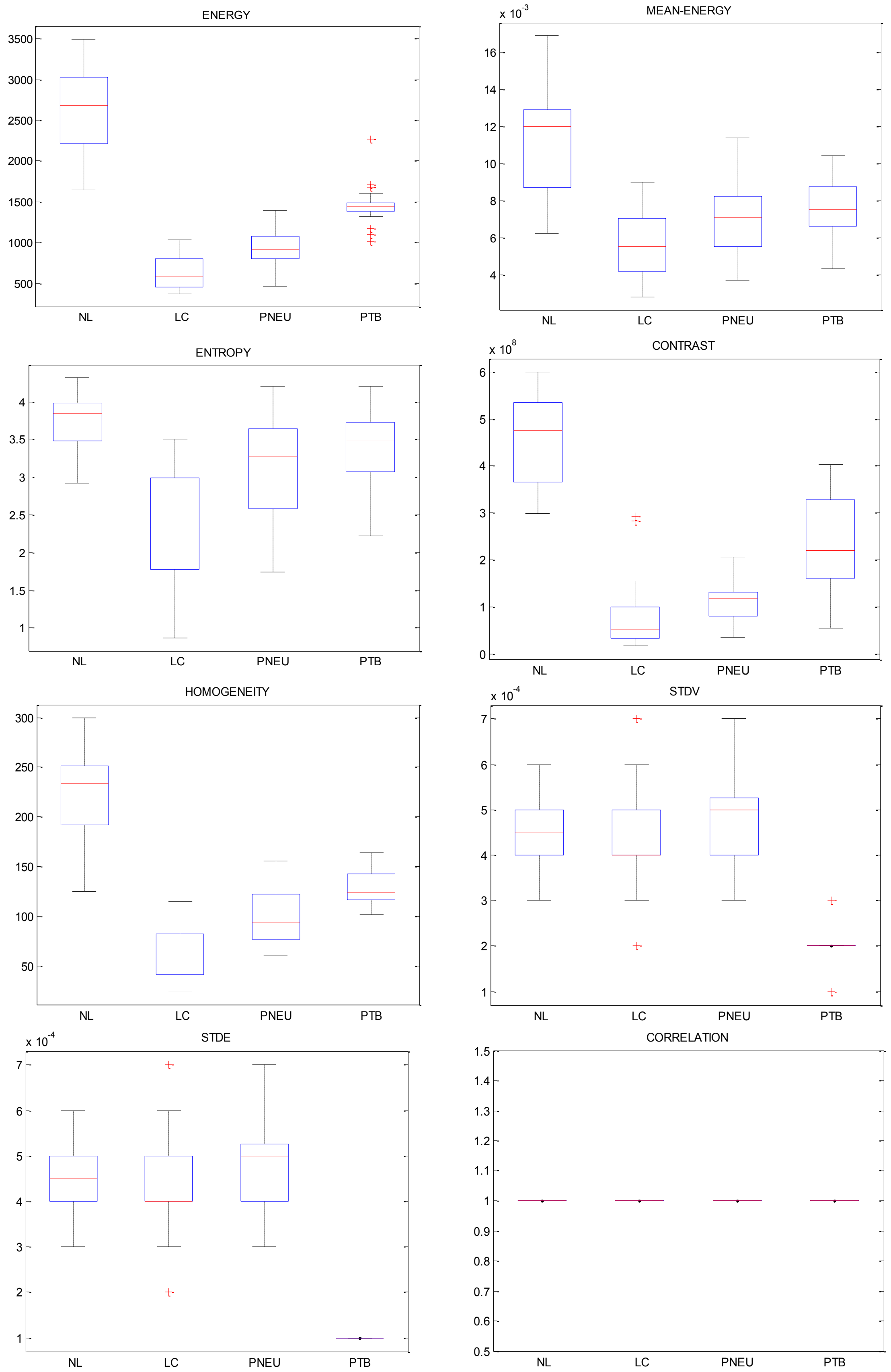

Figure 6.3: Box plots of eight texture measures for NL, LC, PNEU and PTB.

6.5 Testing Normality

Promising results in the Section 6.3 motivated us to develop some parametric discriminant function such as LDF and QDF. It should be noted that LDF and QDF are valid if the variable is normally distributed. In this section testing normality is conducted by Kolmogorov-Smirnov test (KS-test). The results are verified by the Q-Q plot.

6.5.1 Parametric Test

Amongst the many tests for univariate normality (Thode, 2002) the Kolmogorov-Smirnov test (KS-test) is a widely used test for testing goodness of fit due to simplicity and high power even for relatively small sample size (less than 30).

Let $X^T = (x_1, x_2, ..., x_n)$ is a given random variable. The KS-test statistic is the maximum distance between empirical cumulative distribution function, $G(X)$, and assumed standard normal cumulative distribution function, $F(X)$, (Frank & Massey, 1951) where K-stat = max(|$F(X)$-$G(X)$|).

For a given texture measure, say, energy of normal lungs normality is tested at α = 0.05 significance level. Among tested texture measures, the KS-test rejects null hypothesis when standard deviation of value, standard deviation of energy and correlation are tested. However, hypothesis testing shows that energy, mean-energy, entropy, contrast and homogeneity are normally distributed. Results are summarized in Table 6.8 to Table 6.11.

Table 6.8: KS-test on texture measures of NL.

Texture measure	H_0: The given texture measure is normally distributed	K-stat	Critical-value
Energy	H_0 cannot be rejected	0.0904	0.2101
Mean Energy	H_0 cannot be rejected	0.0956	0.2101
Entropy	H_0 cannot be rejected	0.1509	0.2101
Contrast	H_0 cannot be rejected	0.1240	0.2101
Homogeneity	H_0 cannot be rejected	0.1076	0.2101
STD of value	H_0 is rejected	0.2377	0.2101
STD of energy	H_0 is rejected	0.2377	0.2101
Correlation	H_0 is rejected	0.5000	0.2101

Table 6.9: KS-test on texture measures of LC.

Texture measure	H_0: The given texture measure is normally distributed	K-stat	Critical-value
Energy	H_0 cannot be rejected	0.1145	0.1884
Mean Energy	H_0 cannot be rejected	0.1171	0.1884
Entropy	H_0 cannot be rejected	0.1057	0.1884
Contrast	H_0 cannot be rejected	0.1795	0.1884
Homogeneity	H_0 cannot be rejected	0.0839	0.1884
STD of value	H_0 is rejected	0.1892	0.1884
STD of energy	H_0 is rejected	0.1892	0.1884
Correlation	H_0 is rejected	0.5000	0.1884

Table 6.10: KS-test on texture measures of PNEU.

Texture measure	H_0: The given texture measure is normally distributed	K-stat	Critical-value
Energy	H_0 cannot be rejected	0.1025	0.1884
Mean Energy	H_0 cannot be rejected	0.0765	0.1884
Entropy	H_0 cannot be rejected	0.0970	0.1884
Contrast	H_0 cannot be rejected	0.1082	0.1884
Homogeneity	H_0 cannot be rejected	0.1004	0.1884
STD of value	H_0 is rejected	0.2098	0.1884
STD of energy	H_0 is rejected	0.2098	0.1884
Correlation	H_0 is rejected	0.5000	0.1884

Table 6.11: KS-test on texture measures of PTB.

Texture measure	H_0: The given texture measure is normally distributed	K-stat	Critical-value
Energy	H_0 cannot be rejected	0.1186	0.1884
Mean Energy	H_0 cannot be rejected	0.0923	0.1884
Entropy	H_0 cannot be rejected	0.1226	0.1884
Contrast	H_0 cannot be rejected	0.1722	0.1884
Homogeneity	H_0 cannot be rejected	0.1793	0.1884
STD of value	H_0 is rejected	0.3400	0.1884
STD of energy	H_0 is rejected	0.3400	0.1884
Correlation	H_0 is rejected	0.5000	0.1884

6.5.2 Graphical Test

Results of testing normality using KS-test were graphically verified by Q-Q plots. See Figure 6.4 to Figure 6.7.

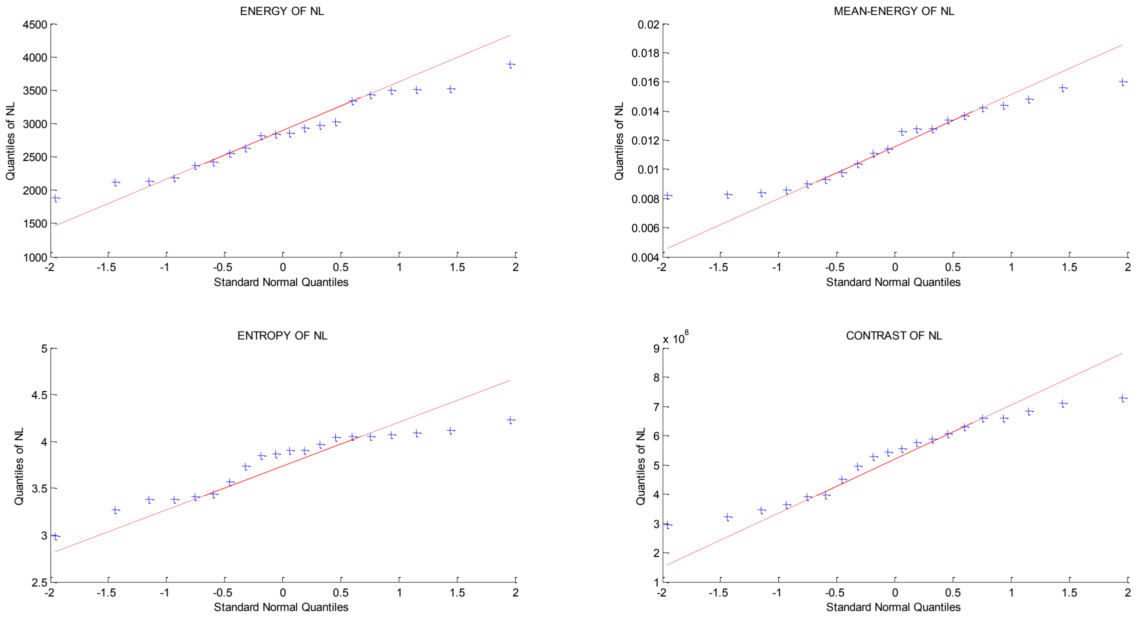

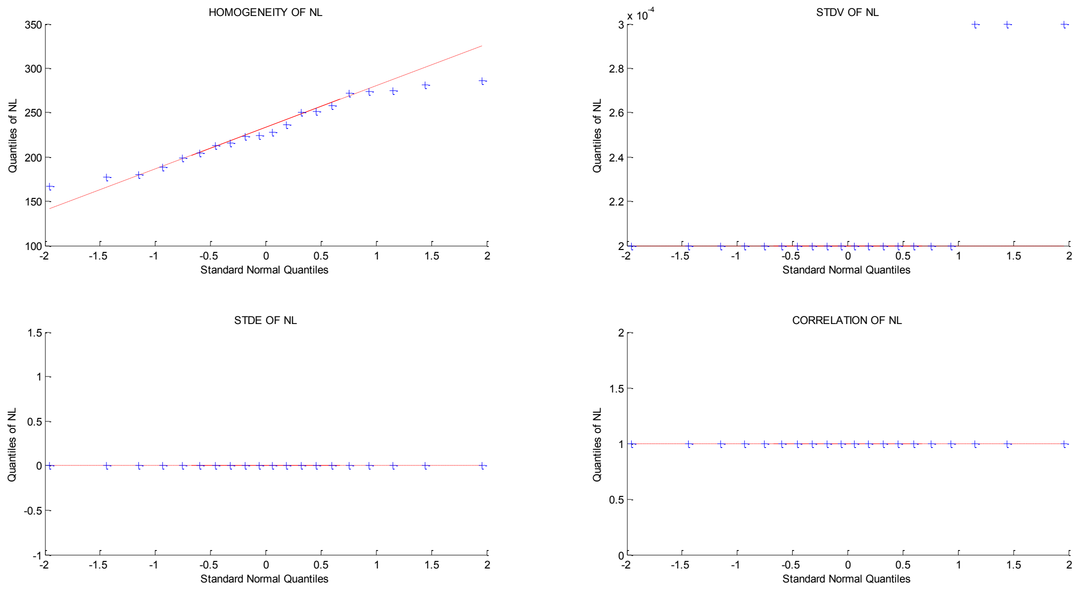

Figure 6.4: QQ-plots of texture measures for NL.

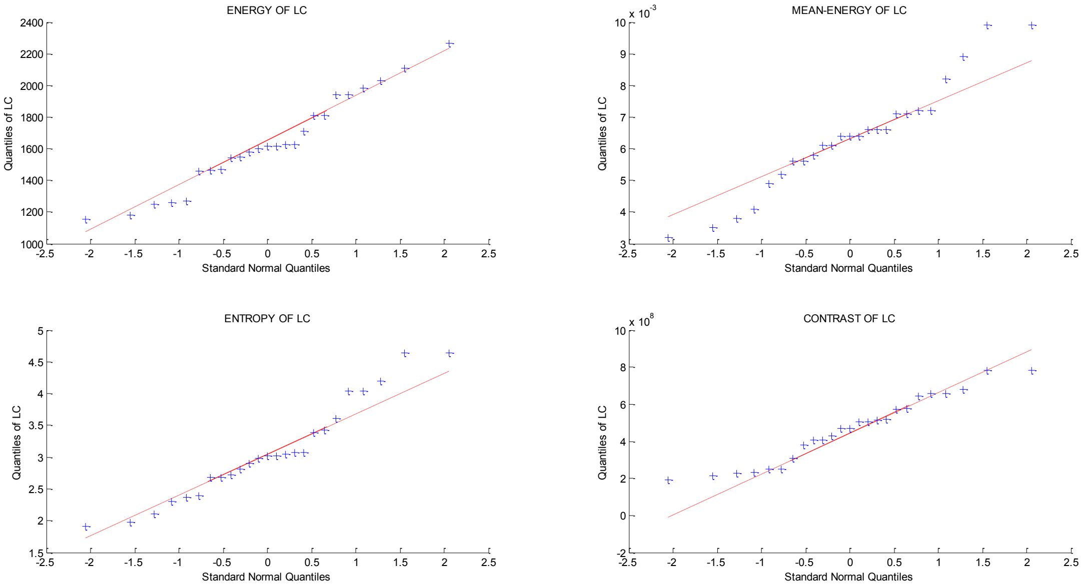

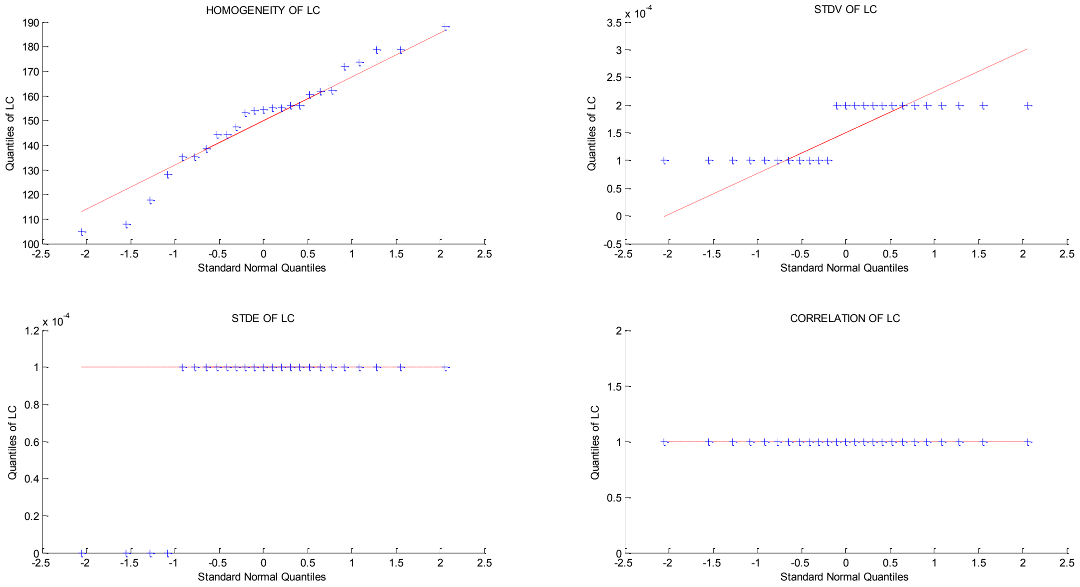

Figure 6.5: QQ-plots of texture measures for LC.

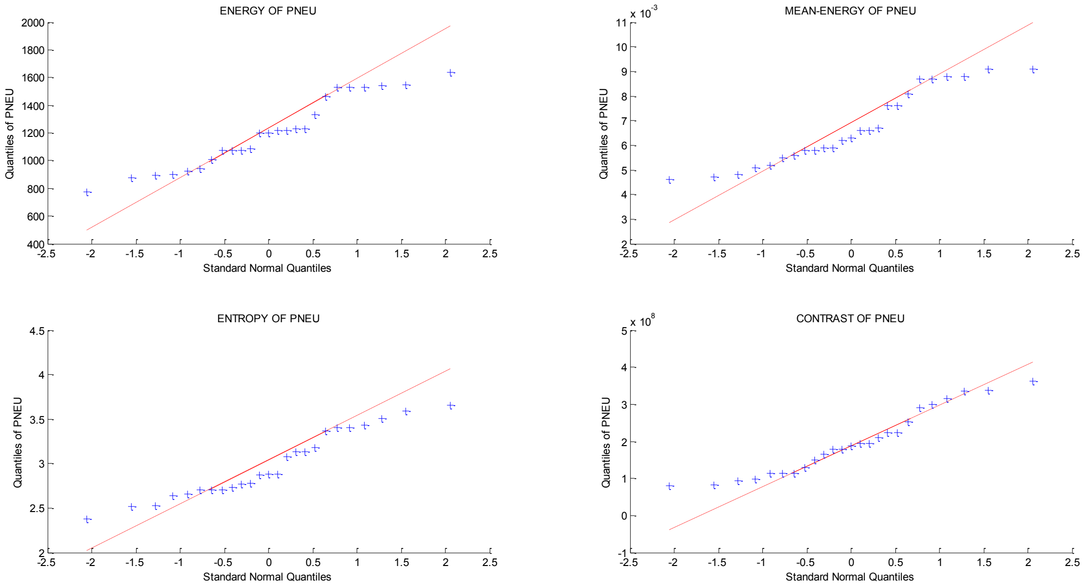

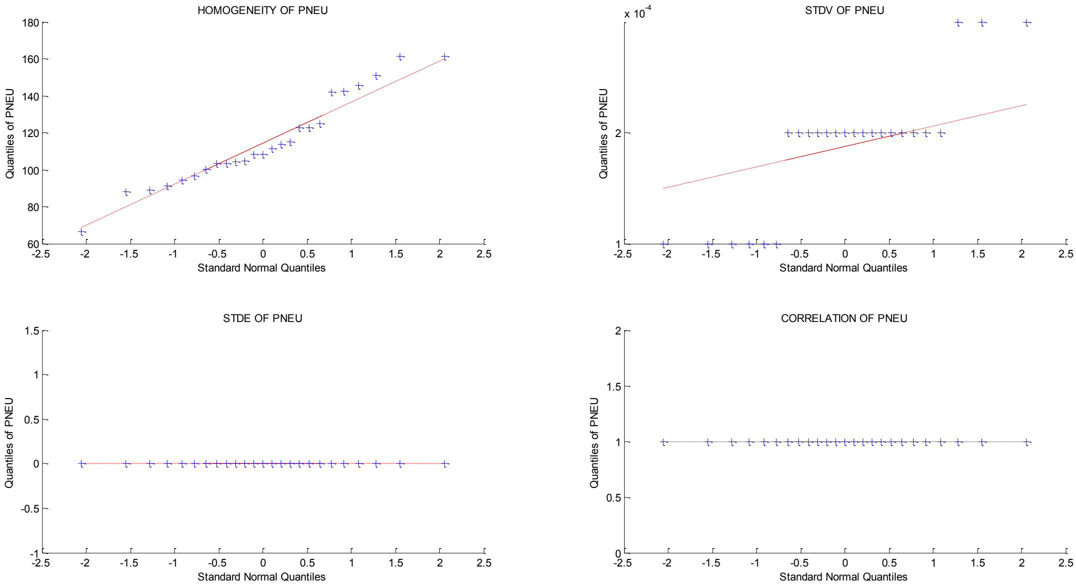

Figure 6.6: QQ-plots of texture measures for PNEU.

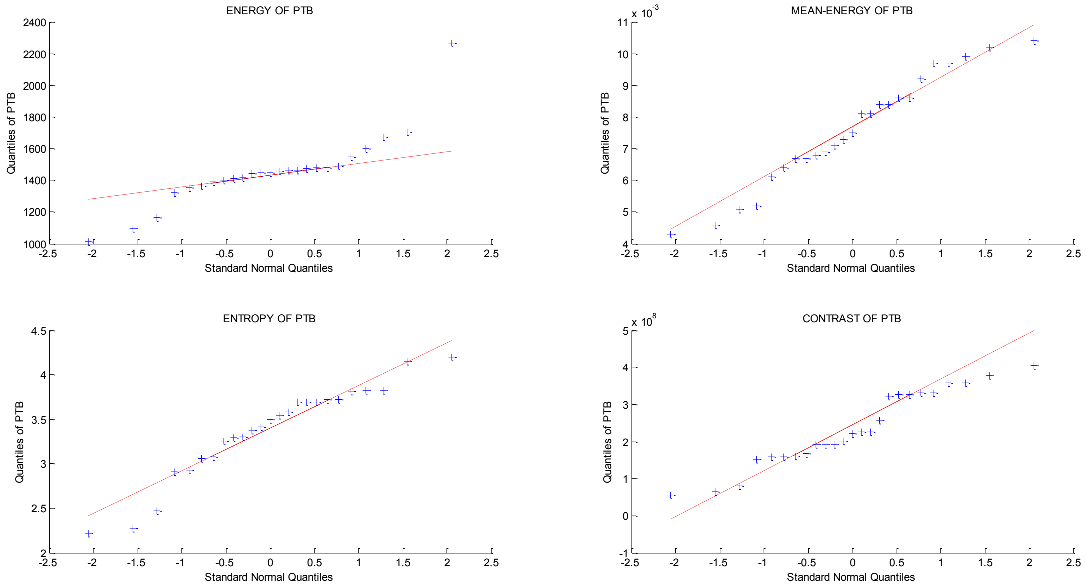

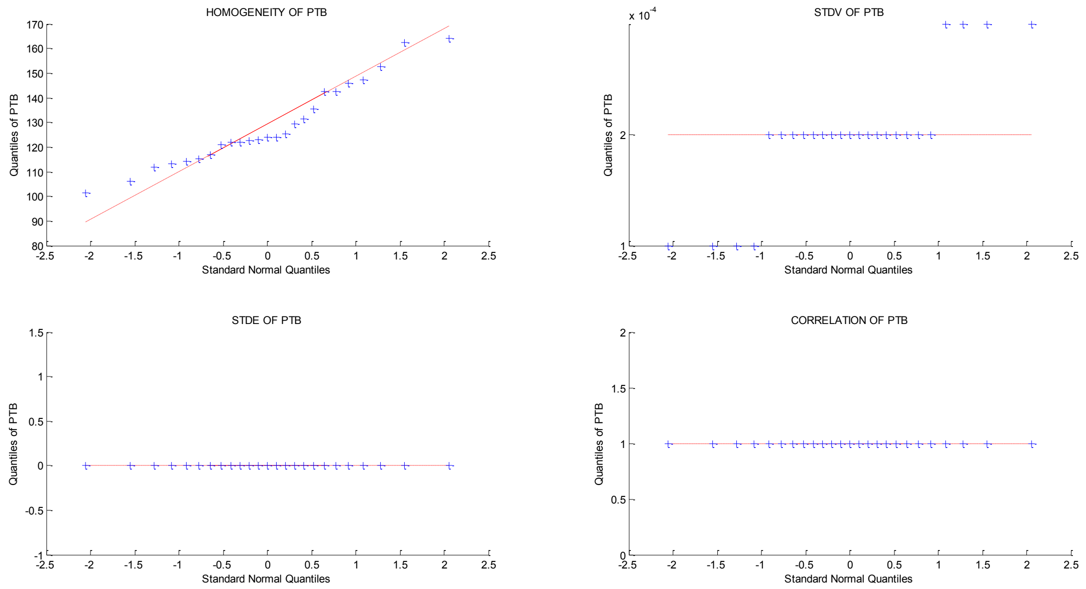

Figure 6.7: QQ-plots of texture measures for PTB.

6.6 An Investigation on Texture Measures

Hypothesis testing in Section 6.5 demonstrate that only five texture measures namely energy, mean energy, entropy, contrast and homogeneity were normally distributed. In this section we graphically study separation of distribution of a given texture measure whose normally distributed for given pair-wise diseases. For example to study how well distinction of energy texture measure distribution when normal lung images and lung cancer images are discriminated, we sketch bell-shaped normal distribution of $N\left(\bar{e}(NL),\sigma_{NL}^2\right)$ and $N\left(\bar{e}(LC),\sigma_{LC}^2\right)$ in a same diagram where, $\bar{e}(NL)$ and $\bar{e}(NL)$ are sample mean of normal lung and lung cancer respectively and σ_{NL}^2 and σ_{LC}^2 are sample variance of normal lung and lung cancer respectively. Distinction between NL and LC using energy texture measure is illustrated in Figure 6.8. Result graphically shows that energy may be is good candidate for NL-LC pair-wise discrimination. The procedure was repeated for all possible pair-wise discriminations for a given texture measure. Results in Figure 6.8 to Figure 6.13 illustrate that texture measures energy, contrast and homogeneity may be provided a good discrimination. However discrimination of lung disease using mean energy and entropy may be applied poorly. Another result is that the misclassification of discrimination between disease-present and disease-absent may be even less than discrimination between two types of lung diseases.

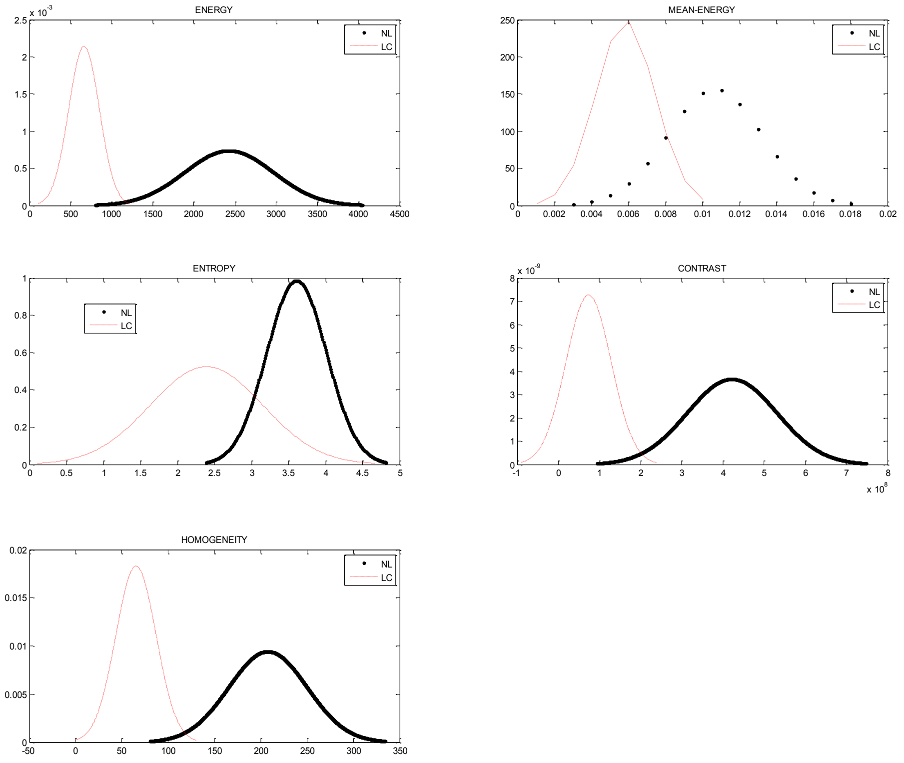

Figure 6.8: Estimated normal distributions of NL and LC.

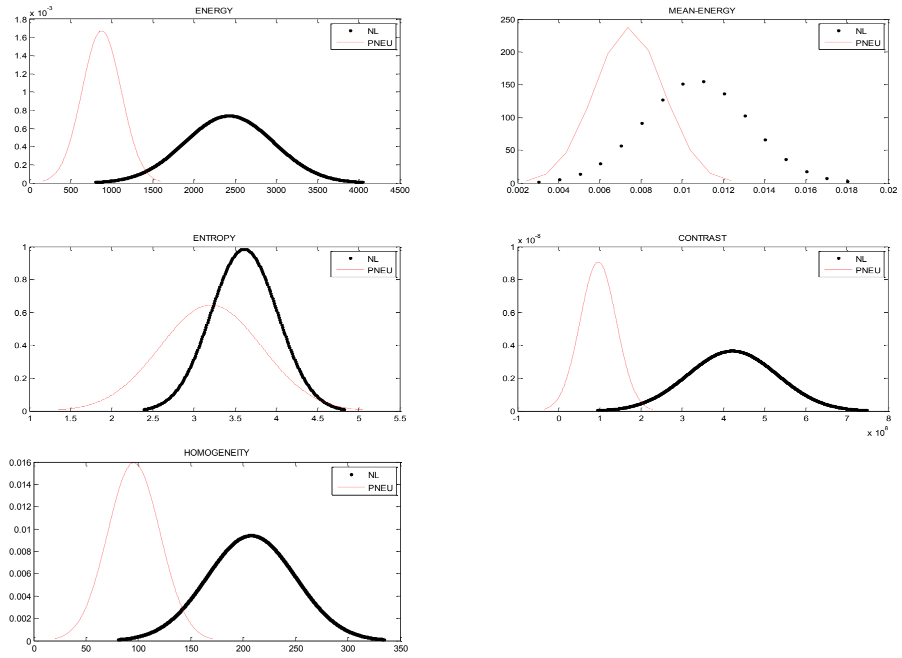

Figure 6.9: Estimated normal distributions of NL and PNEU.

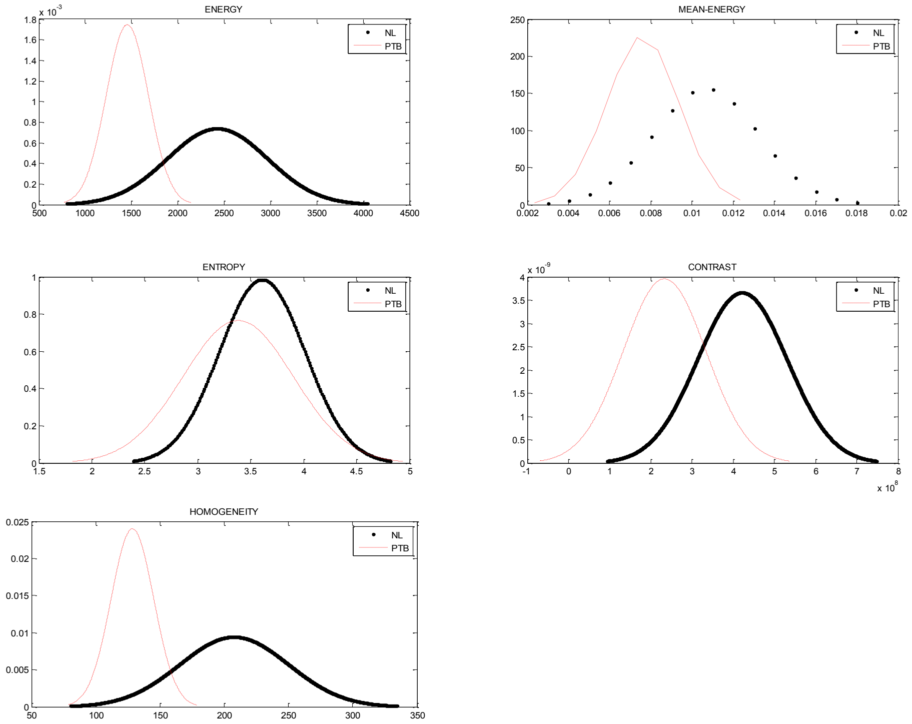

Figure 6.10: Estimated normal distributions of NL and PTB.

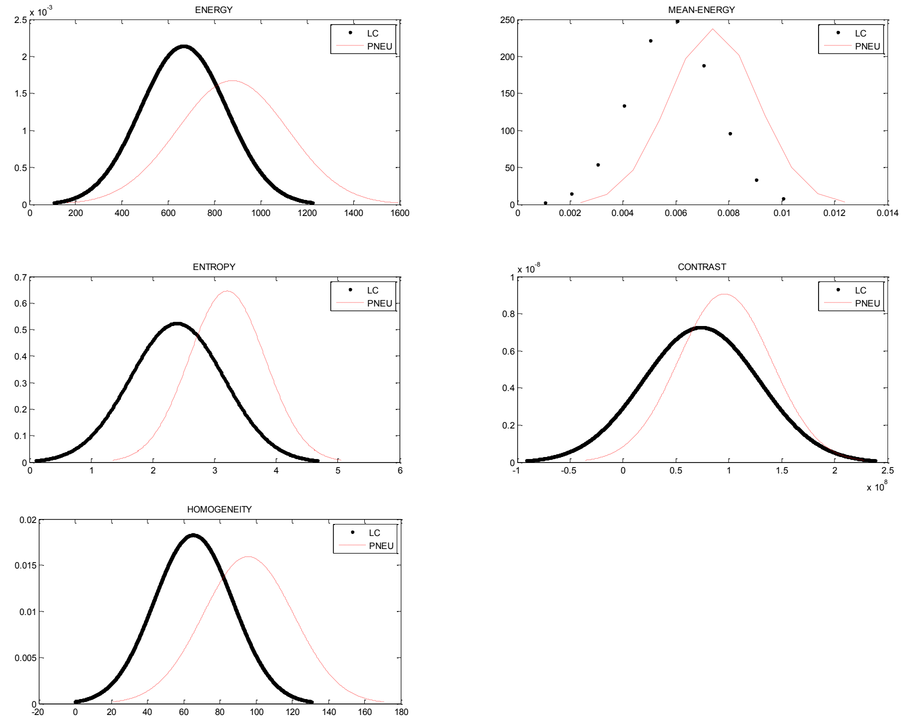

Figure 6.11: Estimated normal distributions of LC and PNEU.

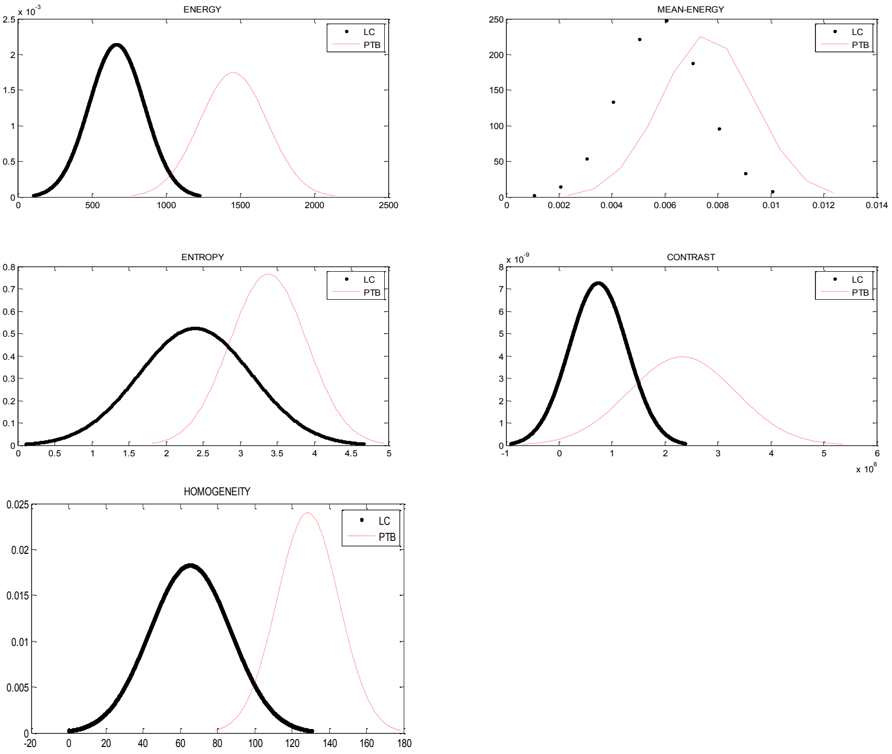

Figure 6.12: Estimated normal distributions of LC and PTB.

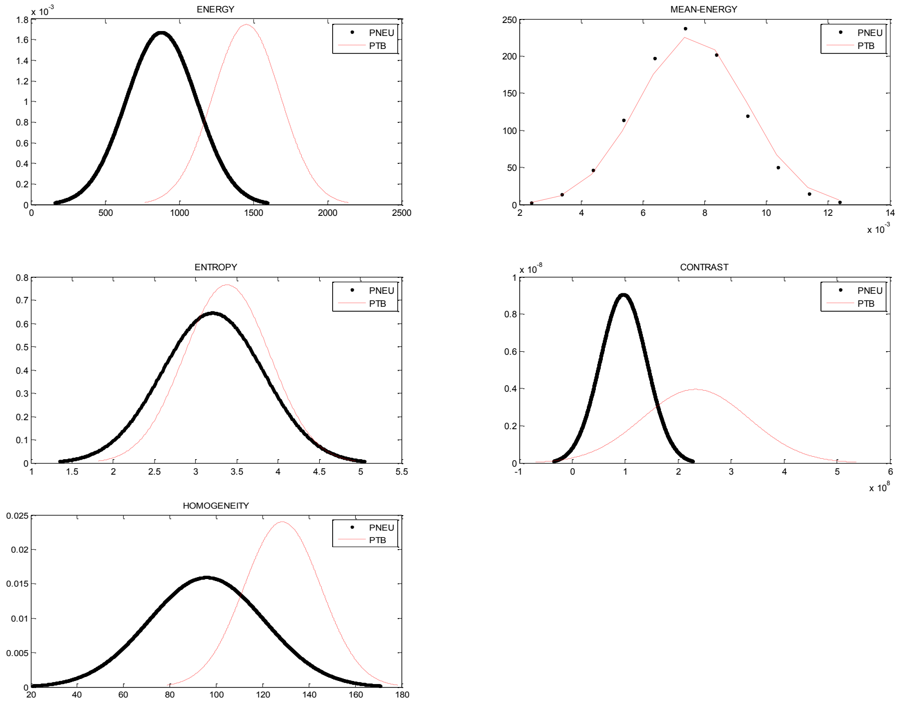

Figure 6.13 : Estimated normal distributions of PNEU and PTB.

It is of interest if discrimination can be improved if the texture measures are considered in pairs. In this section the distribution of all pair-wise combinations of NL, LC, PNEU and PTB were illustrated with two dimensional plot of texture measures.

Elliptic distributions of all pair-wise combinations are given in Figure 6.14 to Figure 6.19. Results generally show that energy and homogeneity gave perfect separation for discrimination of disease-present disease-absent cases while mean-energy and entropy has performed badly. For discrimination between LC and PTB again energy and homogeneity gave better separation compare to other texture measures. Discrimination between PNEU and PTB with these texture measures is hopeless.

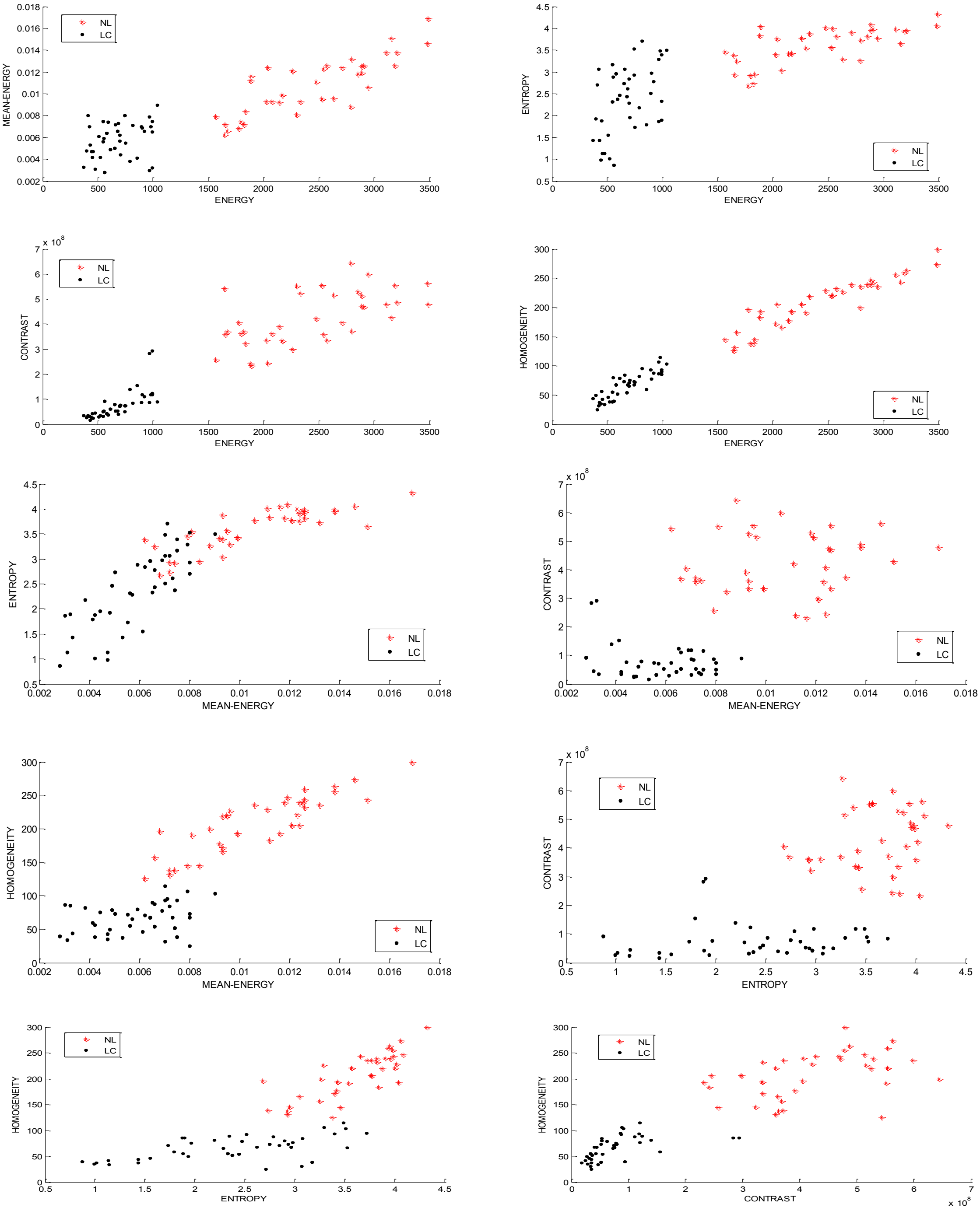

Figure 6.14: Scatter plots of the pairs textures for LC and NL discrimination.

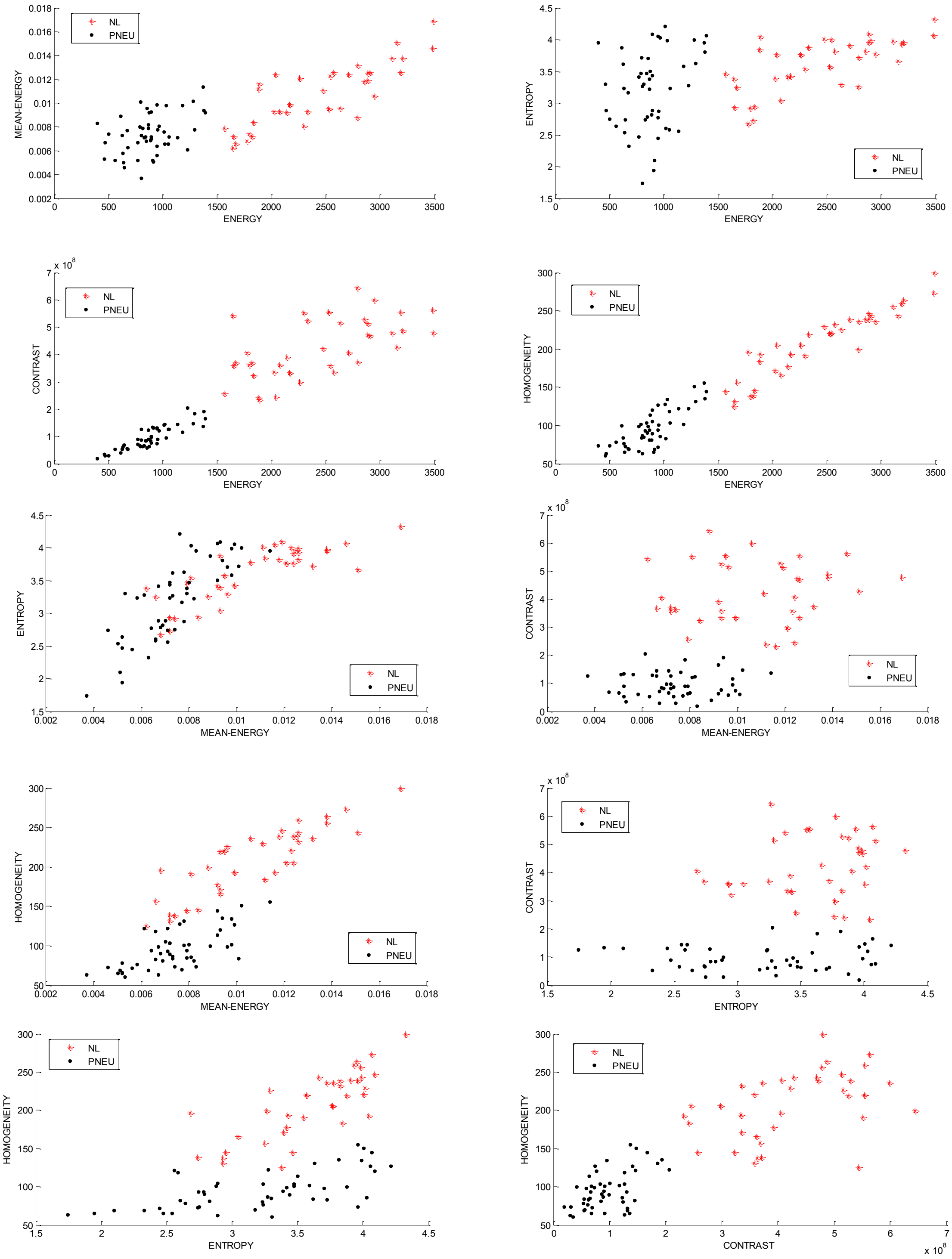

Figure 6.15: Scatter plots of the pairs textures for PNEU and NL discrimination.

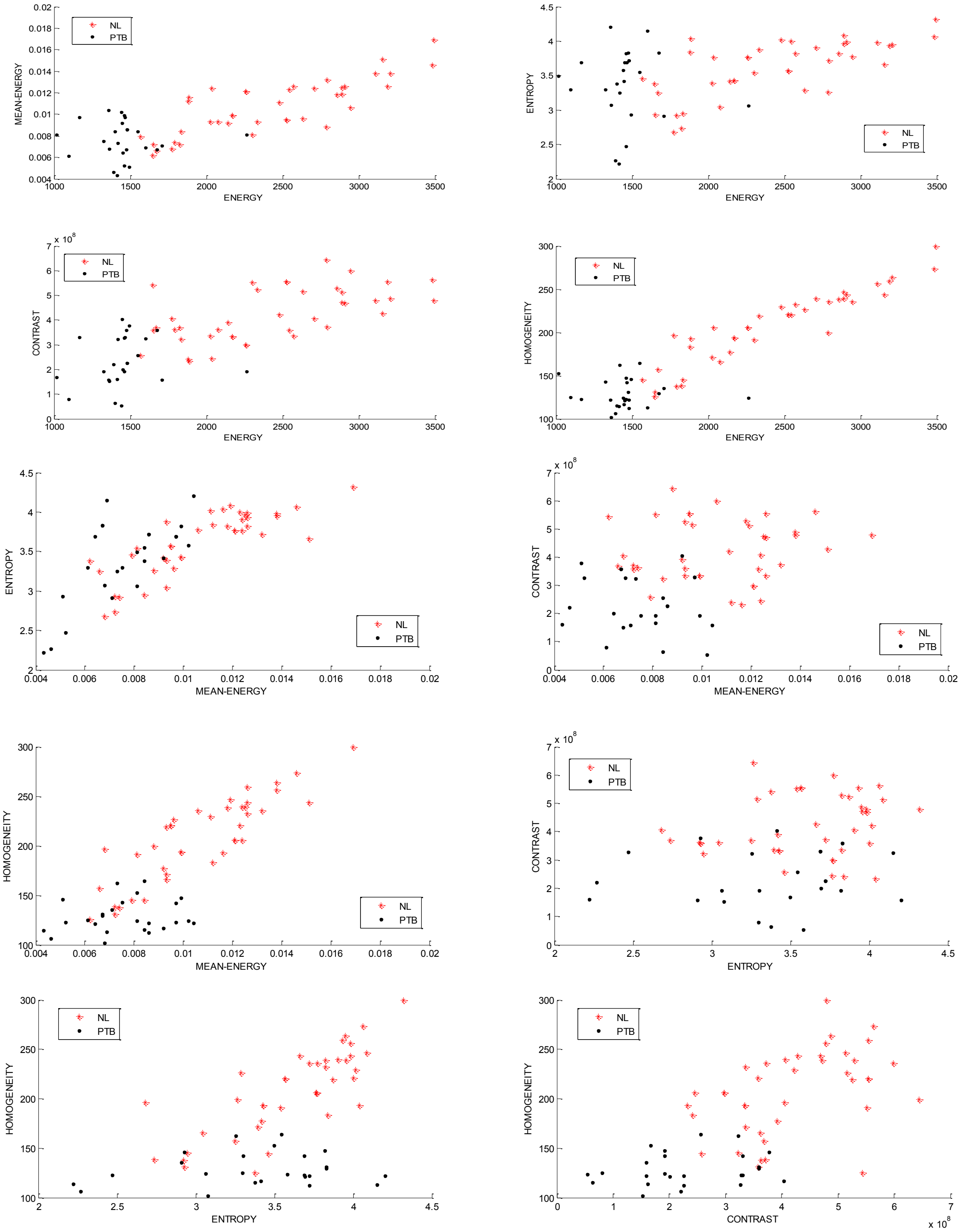

Figure 6.16: Scatter plots of the pairs textures for PTB and NL discrimination.

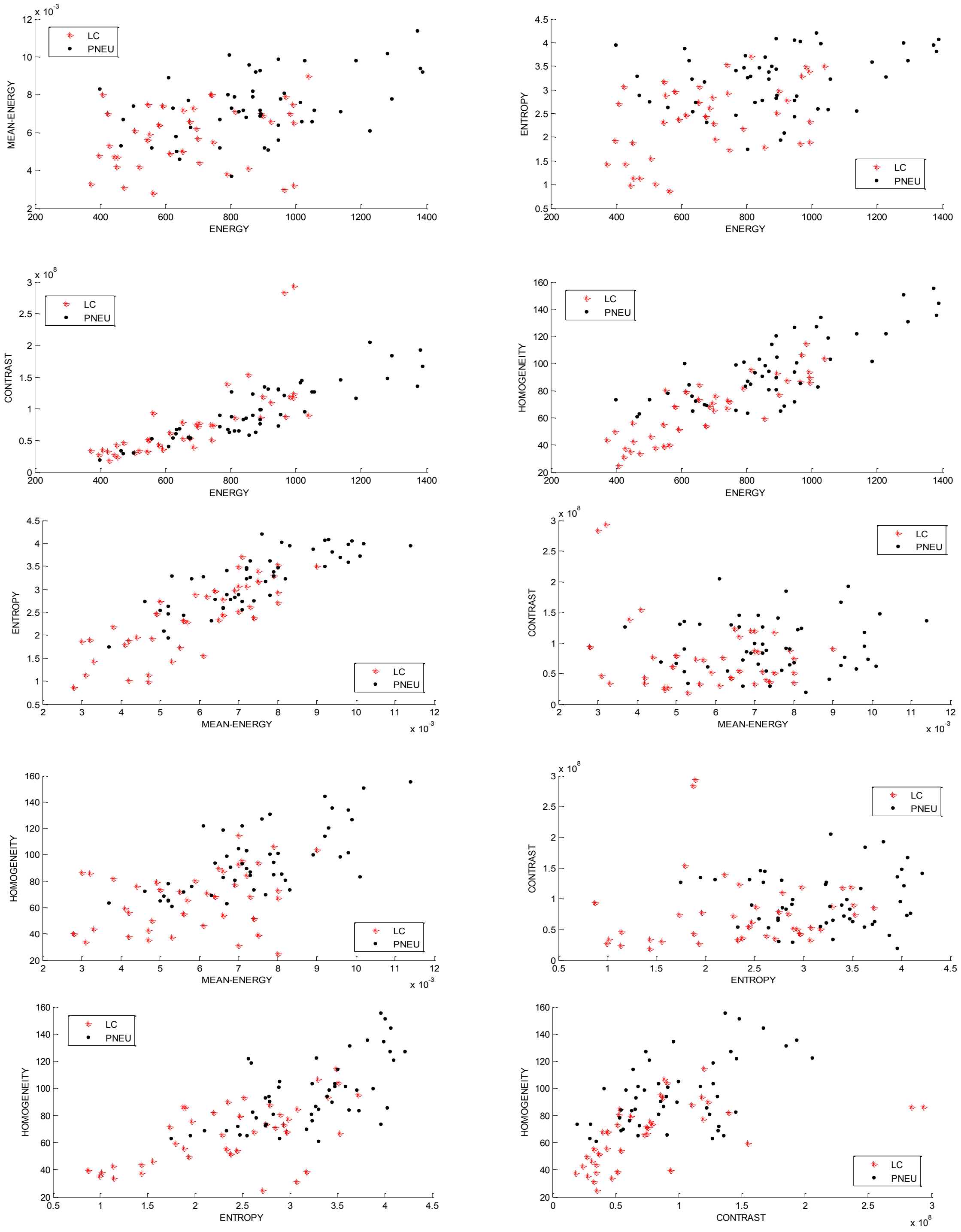

Figure 6.17: Scatter plots of the pairs textures for PNEU and LC discrimination.

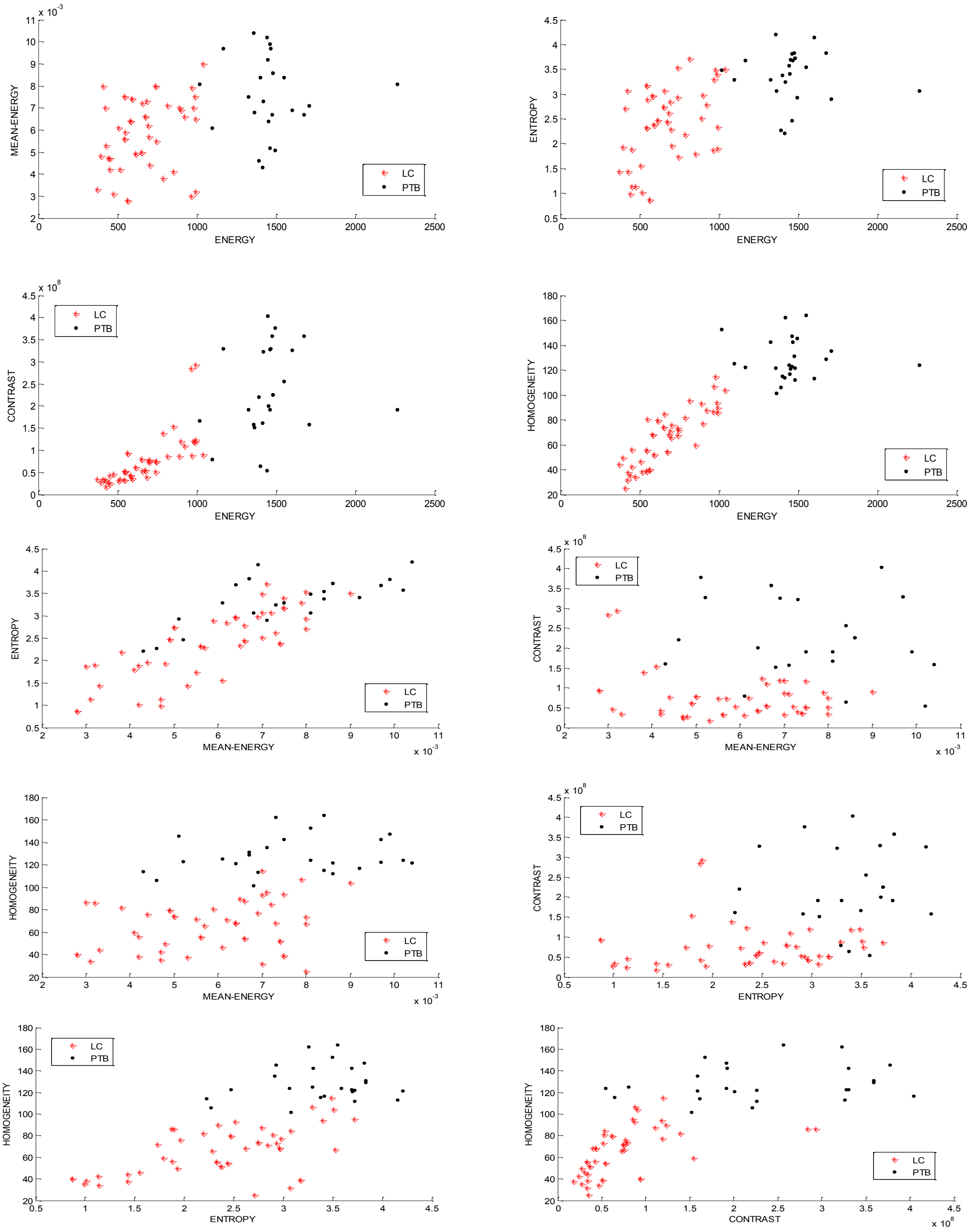

Figure 6.18: Scatter plots of the pairs textures for PTB and LC discrimination.

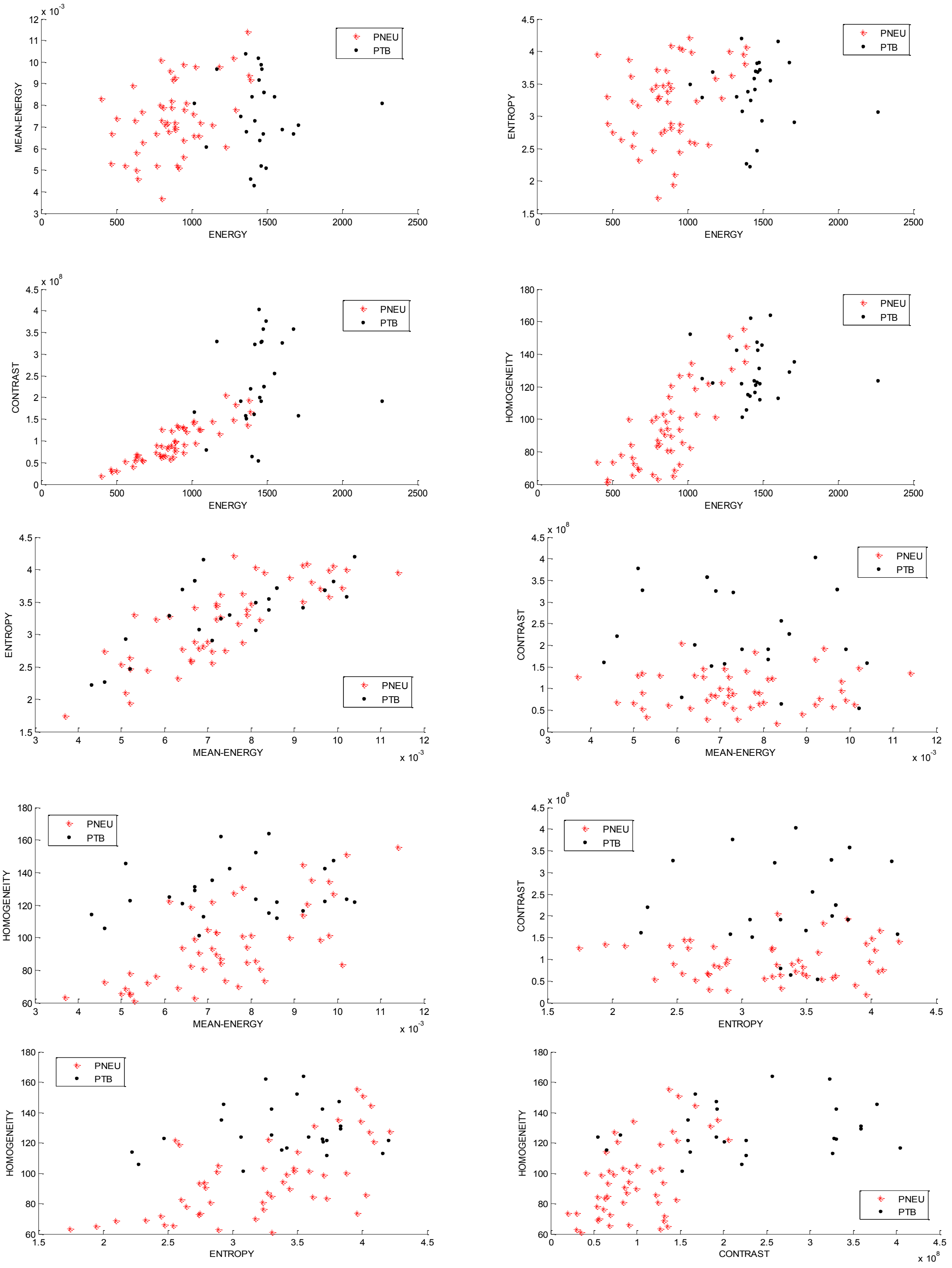

Figure 6.19: Scatter plots of the pairs textures for PNEU and PTB discrimination.

6.7 Testing Equality of Variances

Consider two univariate normal populations π_1 and π_2 that are represented by $N(\mu_1, \sigma_1^2)$ and $N(\mu_2, \sigma_2^2)$ respectively. Let $X^T = (x_1, x_2, ..., x_{n_1})$ and $Y^T = (y_1, y_2, ..., y_{n_2})$ be random samples taken from π_1 and π_2 respectively. Since it is known that $\frac{(n_1-1)S_1^2}{\sigma_1^2} \sim \chi^2_{n_1-1}$ and $\frac{(n_2-1)S_2^2}{\sigma_2^2} \sim \chi^2_{n_2-1}$, therefore $F = \frac{S_1^2/\sigma_1^2}{S_2^2/\sigma_2^2} \sim F_{n_1-1,n_2-1}$.

In the case of $\sigma_1^2 = \sigma_2^2$, $F = \frac{S_1^2}{S_2^2} \sim F_{n_1-1,n_2-1}$. Henceforth we consider testing the hypothesis $H_0 : \sigma_1^2 = \sigma_2^2$ versus $H_1 : \sigma_1^2 \neq \sigma_2^2$.

The null hypothesis is accepted at the γ significance level if the ratio of sample variances (F) falls within the range $F_{n_1-1,n_2-1,(\gamma/2)} \leq F \leq F_{n_1-1,n_2-1,(1-\gamma/2)}$ (Rosner, 1990). Figure 6.20 illustrates the rejection regions.

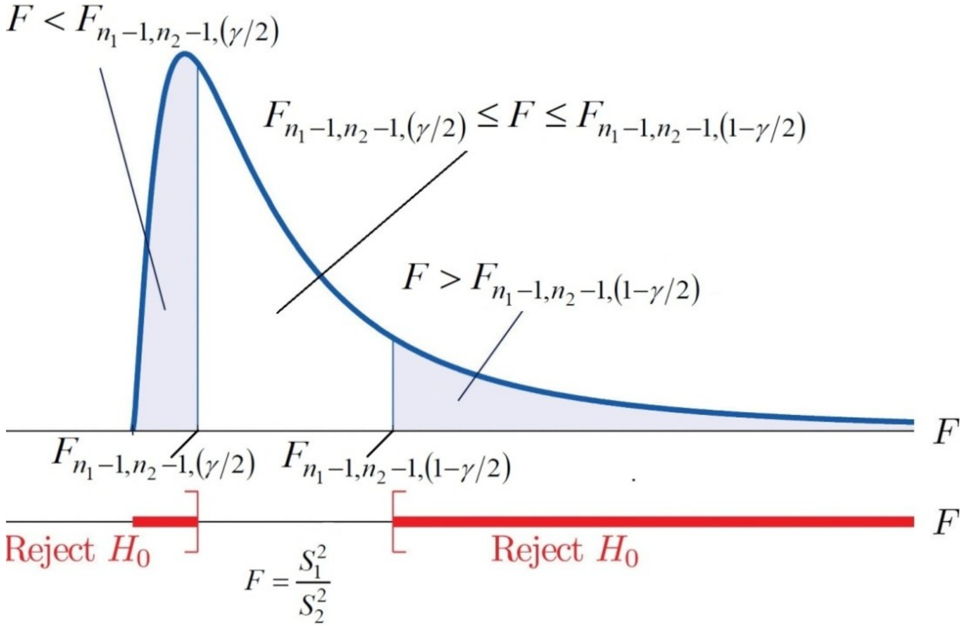

Figure 6.20: Rejection regions for the F-test.

Results of testing equality of two variances at $\gamma = 0.05$ significance level are given in Table 6.12 to Table 6.17.

Table 6.12: Equality test for variances of texture measures of NL and LC cases.

Energy				
Data		$\bar{x}$	S	$H_0 : \sigma_1^2 = \sigma_2^2$?
Population 1	NL	2589.37	597.1459	Reject
Population 2	LC	645.55	217.2295	
Mean-energy				
Data		$\bar{x}$	S	$H_0 : \sigma_1^2 = \sigma_2^2$?
Population 1	NL	0.0111	0.0029	Reject
Population 2	LC	0.0055	0.0017	
Entropy				
Data		$\bar{x}$	S	$H_0 : \sigma_1^2 = \sigma_2^2$?
Population 1	NL	3.7351	0.3802	Reject
Population 2	LC	2.2918	0.7917	
Contrast				
Data		$\bar{x}$	S	$H_0 : \sigma_1^2 = \sigma_2^2$?
Population 1	NL	454355607.00	91011404.00	Accept
Population 2	LC	79920487.00	73054791.00	
Homogeneity				
Data		$\bar{x}$	S	$H_0 : \sigma_1^2 = \sigma_2^2$?
Population 1	NL	218.74	48.9661	Reject
Population 2	LC	63.58	24.1759	

Table 6.13: Equality test for variances of texture measures of NL and PNEU cases.

Energy				
Data		$\bar{x}$	S	$H_0 : \sigma_1^2 = \sigma_2^2$?
Population 1	NL	2589.37	597.1459	Reject
Population 2	PNEU	945.64	233.0260	
Mean-energy				
Data		$\bar{x}$	S	$H_0 : \sigma_1^2 = \sigma_2^2$?
Population 1	NL	0.0111	0.0029	Accept
Population 2	PNEU	0.0072	0.0019	
Entropy				
Data		$\bar{x}$	S	$H_0 : \sigma_1^2 = \sigma_2^2$?
Population 1	NL	3.7351	0.3802	Reject
Population 2	PNEU	3.1330	0.6579	
Contrast				
Data		$\bar{x}$	S	$H_0 : \sigma_1^2 = \sigma_2^2$?
Population 1	NL	454355607. 00	91011404.00	Reject
Population 2	PNEU	110250894. 00	42183149.00	
Homogeneity				
Data		$\bar{x}$	S	$H_0 : \sigma_1^2 = \sigma_2^2$?
Population 1	NL	218.7403	48.9661	Reject
Population 2	PNEU	97.9343	26.8292	

Table 6.14: Equality test for variances of texture measures of NL and PTB cases.

Energy				
Data		$\bar{x}$	S	$H_0 : \sigma_1^2 = \sigma_2^2 ?$
Population 1	NL	2589.37	597.1459	Reject
Population 2	PTB	1455.3852	228.4494	
Mean-energy				
Data		$\bar{x}$	S	$H_0 : \sigma_1^2 = \sigma_2^2 ?$
Population 1	NL	0.0111	0.0029	Reject
Population 2	PTB	0.0076	0.0017	
Entropy				
Data		$\bar{x}$	S	$H_0 : \sigma_1^2 = \sigma_2^2 ?$
Population 1	NL	3.7351	0.3802	Accept
Population 2	PTB	3.3820	0.5212	
Contrast				
Data		$\bar{x}$	S	$H_0 : \sigma_1^2 = \sigma_2^2 ?$
Population 1	NL	454355607. 00	91011404.00	Accept
Population 2	PTB	233514377. 00	100818509.00	
Homogeneity				
Data		$\bar{x}$	S	$H_0 : \sigma_1^2 = \sigma_2^2 ?$
Population 1	NL	218.7403	48.9661	Reject
Population 2	PTB	128.6444	16.6215	

Table 6.15: Equality test for variances of texture measures of LC and PNEU cases.

Energy				
Data		$\bar{x}$	S	$H_0:\sigma_1^2=\sigma_2^2$?
Population 1	LC	645.5564	217.2295	Accept
Population 2	PNEU	945.6456	233.0260	
Mean-energy				
Data		$\bar{x}$	S	$H_0:\sigma_1^2=\sigma_2^2$?
Population 1	LC	0.0055	0.0017	Accept
Population 2	PNEU	0.0072	0.0019	
Entropy				
Data		$\bar{x}$	S	$H_0:\sigma_1^2=\sigma_2^2$?
Population 1	LC	2.2918	0.7917	Accept
Population 2	PNEU	3.1330	0.6579	
Contrast				
Data		$\bar{x}$	S	$H_0:\sigma_1^2=\sigma_2^2$?
Population 1	LC	79920487. 00	73054791.00	Reject
Population 2	PNEU	110250894. 00	42183149.00	
Homogeneity				
Data		$\bar{x}$	S	$H_0:\sigma_1^2=\sigma_2^2$?
Population 1	LC	63.5840	24.1759	Accept
Population 2	PNEU	97.9343	26.8292	

Table 6.16: Equality test for variances of texture measures of LC and PTB cases.

Energy				
Data		$\bar{x}$	S	$H_0 : \sigma_1^2 = \sigma_2^2$?
Population 1	LC	645.5564	217.2295	Accept
Population 2	PTB	1455.3852	228.4494	
Mean energy				
Data		$\bar{x}$	S	$H_0 : \sigma_1^2 = \sigma_2^2$?
Population 1	LC	0.0055	0.0017	Accept
Population 2	PTB	0.0076	0.0017	
Entropy				
Data		$\bar{x}$	S	$H_0 : \sigma_1^2 = \sigma_2^2$?
Population 1	LC	2.2918	0.7917	Reject
Population 2	PTB	3.3820	0.5212	
Contrast				
Data		$\bar{x}$	S	$H_0 : \sigma_1^2 = \sigma_2^2$?
Population 1	LC	79920487. 00	73054791.00	Accept
Population 2	PTB	233514377. 00	100818509.00	
Homogeneity				
Data		$\bar{x}$	S	$H_0 : \sigma_1^2 = \sigma_2^2$?
Population 1	LC	63.5840	24.1759	Accept
Population 2	PTB	128.6444	16.6215	

Table 6.17: Equality test for variances of texture measures of PNEU and PTB cases.

Energy				
Data		$\bar{x}$	S	$H_0 : \sigma_1^2 = \sigma_2^2 ?$
Population 1	PNEU	945.6456	233.0260	Accept
Population 2	PTB	1455.3852	228.4494	
Mean-energy				
Data		$\bar{x}$	S	$H_0 : \sigma_1^2 = \sigma_2^2 ?$
Population 1	PNEU	0.0072	0.0019	Accept
Population 2	PTB	0.0076	0.0017	
Entropy				
Data		$\bar{x}$	S	$H_0 : \sigma_1^2 = \sigma_2^2 ?$
Population 1	PNEU	3.1330	0.6579	Accept
Population 2	PTB	3.3820	0.5212	
Contrast				
Data		$\bar{x}$	S	$H_0 : \sigma_1^2 = \sigma_2^2 ?$
Population 1	PNEU	110250894. 00	42183149.00	Reject
Population 2	PTB	233514377. 00	100818509.00	
Homogeneity				
Data		$\bar{x}$	S	$H_0 : \sigma_1^2 = \sigma_2^2 ?$
Population 1	PNEU	97.9343	26.8292	Reject
Population 2	PTB	128.6444	16.6215	

6.8 Univariate Discriminant Functions

For those texture measures that are normally distributed the LDF can be used for discrimination when variances are equal, otherwise the QDF is used. The performance of the discriminant functions are given by the probability of Type I Error (α) and probability of Type II Error (β) (Johnson & Wichern, 2002). Definitions and notations for the LDF, QDF, α and β are given as follows:

Without loss of generality, for discriminating LC cases from NL cases using the discriminant function $Q(x_0) = \ln\left(\frac{f_{LC}(x_0)}{f_{NL}(x_0)}\right)$, If $Q(x_0) \geq \ln(C)$, x_0 is identified as LC, otherwise x_0 is identified as NL where $C = \left[\left(\frac{c(LC \mid NL)}{c(NL \mid LC)}\right) \cdot \left(\frac{p_{NL}}{p_{LC}}\right)\right]$.

When samples have equal variances the well known linear discriminant function (LDF),

$$\hat{L}(x_0) = (\bar{x}_{LC} - \bar{x}_{NL})^T S^{-1} x_0 - \frac{1}{2}(\bar{x}_{LC} - \bar{x}_{NL})^T S^{-1}(\bar{x}_{LC} + \bar{x}_{NL}),$$

is used. Otherwise the quadratic discriminant function (QDF),

$$\hat{Q}(x_0) = -\frac{1}{2} x_0^T \left(S_{LC}^{-1} - S_{NL}^{-1}\right) x_0 + \left(\bar{x}_{LC}^T \; S_{LC}^{-1} - \bar{x}_{NL}^T \; S_{NL}^{-1}\right) x_0 - k \, .$$

is used, where,

$\bar{x}_{LC} = \frac{1}{n_{LC}} \sum_{i=1}^{n_{LC}} x_{LC}$, $S_{LC} = \frac{1}{n_{LC} - 1} \sum_{i=1}^{n_{LC}} (x_{LC} - \bar{x}_{LC})^2$ and

$\bar{x}_{NL} = \dfrac{1}{n_{NL}} \sum_{i=1}^{n_{NL}} x_{NL}$, $S_{NL} = \dfrac{1}{n_{NL}-1} \sum_{i=1}^{n_{NL}} \left(x_{NL} - \bar{x}_{NL}\right)^2$, where n_{LC} and n_{LC} denoted the number of control data from LC and NL respectively, and

$$S = \left[\frac{n_{LC}-1}{(n_{LC}-1)+(n_{NL}-1)}\right] S_{LC} + \left[\frac{n_{NL}-1}{(n_{LC}-1)+(n_{NL}-1)}\right] S_{NL} \text{ and}$$

$$k = \frac{1}{2}\ln\left(\frac{|S_{LC}|}{|S_{NL}|}\right) + \frac{1}{2}\left(\bar{x}_{LC}^{T}\ S_{LC}^{-1}\ \bar{x}_{LC} - \bar{x}_{NL}^{T}\ S_{NL}^{-1}\ \bar{x}_{NL}\right).$$

The choice of LDF and QDF follows the result of the $H_0 : \sigma_1^2 = \sigma_2^2$ where σ_j^2 is the variance of $x_j, \quad j = 1,2$.

Twenty-five LC cases and twenty NL cases were used to develop the optimal discriminant function for a given texture measure *x*. For the remaining data set the same texture measure *x* substituted into the proper discriminant function.

Let *x* is a texture measure extracted from a lung cancer image. For the NL-LC pair wise discrimination, Consider hypothesises:

H_0 : *x* extracted from a lung cancer image

versus

H_1 : *x* extracted from a normal lung image.

Type I Error occurs when null hypothesis is rejected incorrectly and Type II Error occurs when null hypothesis is accepted incorrectly. Henceforth α and β is defined as probability of type I Error and Type II Error respectively.

α_1 = P(reject H_0 | H_0 is true) or equivalently α_1 = P(NL | LC) and

β_1 = P(accept H_0 | H_0 is false) or equivalently β_1 = P(LC | NL).

Since we do not have global information about distribution of lung cancer we assume equal misclassification costs and equal a prior probabilities, total ignorance (C=1). The probability of Type I Error and Type II Error of NL-LC pair wise discrimination is given in Table 6.18. The procedure of calculating Type I Error and Type II Error is demonstrated in Figure 6.21.

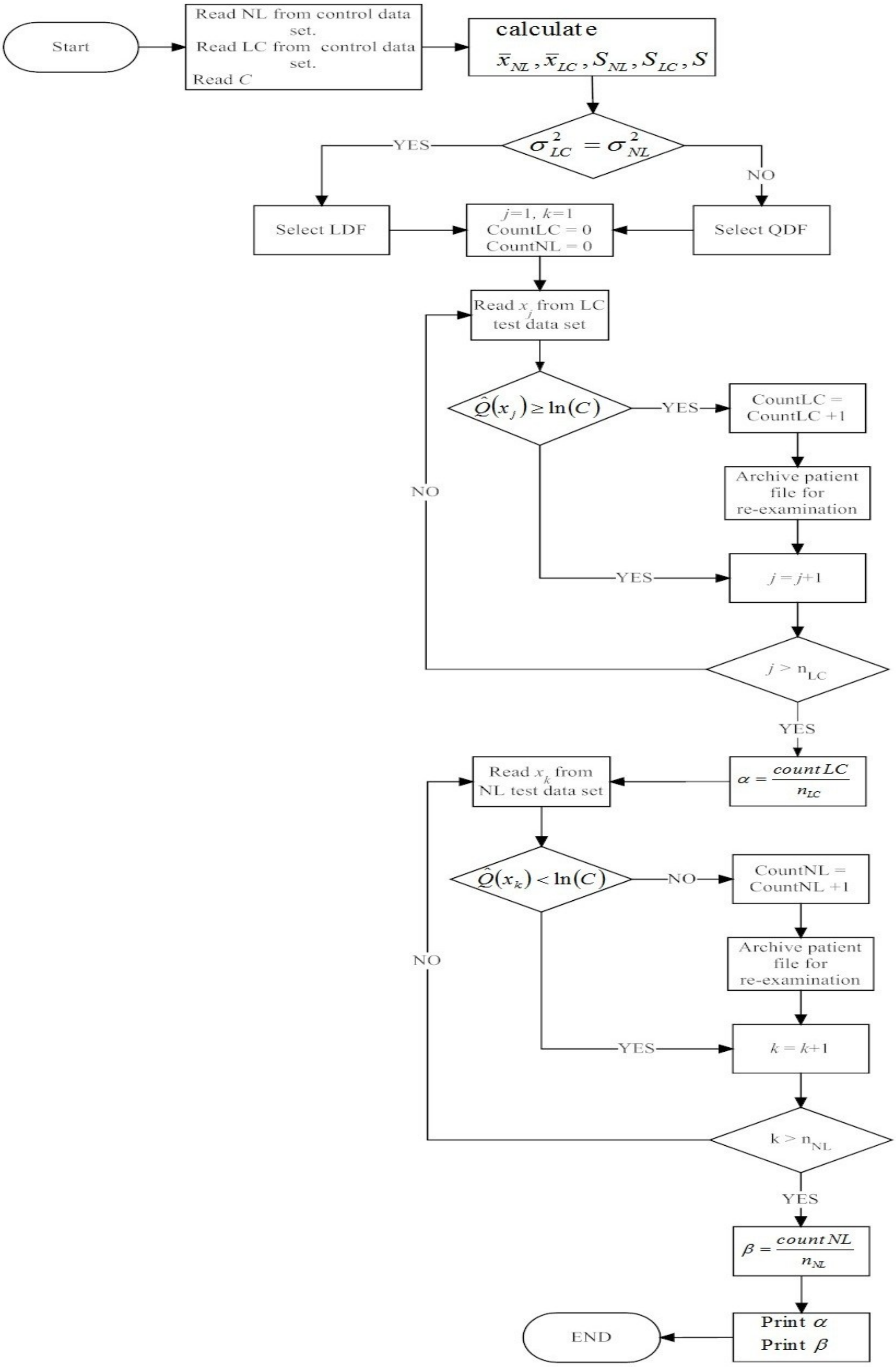

Figure 6.21: Procedure of calculating Type I Error and Type II Error.

Similarly for PNEU-NL pair wise discrimination, PTB-NL pair wise discrimination, LC-PNEU pair wise discrimination, LC-PTB pair wise discrimination and PNEU-PTB pair wise discrimination the probability of Type II Error and probability of Type II Error are listed in Table 6.19 to Table 6.23.

Table 6.18: Probability of Type I and Type II Errors of LC-NL discrimination.

	Texture measure				
	Energy	Mean energy	Entropy	Contrast	Homogeneity
Type I Error	0.00	0.00	0.08	0.00	0.00
Type II Error	0.00	0.28	0.32	0.06	0.08

Table 6.19: Probability of Type I and Type II Errors of PNEU-NL discrimination.

	Texture measure				
	Energy	Mean energy	Entropy	Contrast	Homogeneity
Type I Error	0.00	0.28	0.44	0.00	0.00
Type II Error	0.00	0.44	0.48	0.00	0.04

Table 6.20: Probability of Type I and Type II Errors of PTB-NL discrimination.

	Texture measure				
	Energy	Mean energy	Entropy	Contrast	Homogeneity
Type I Error	0.04	0.20	0.40	0.06	0.00
Type II Error	0.06	0.56	0.60	0.06	0.08

Table 6.21: Probability of Type I and Type II Errors of LC-PNEU discrimination.

	Texture measure				
	Energy	Mean energy	Entropy	Contrast	Homogeneity
Type I Error	0.24	0.56	0.48	0.24	0.20
Type II Error	0.44	0.16	0.12	0.44	0.32

Table 6.22: Probability of Type I and Type II Errors of LC-PTB discrimination.

	Texture measure				
	Energy	Mean energy	Entropy	Contrast	Homogeneity
Type I Error	0.12	0.44	0.36	0.08	0.12
Type II Error	0.16	0.36	0.20	0.12	0.16

Table 6.23: Probability of Type I and Type II Errors of PNEU-PTB discrimination.

	Texture measure				
	Energy	Mean energy	Entropy	Contrast	Homogeneity
Type I Error	0.24	0.52	0.44	0.36	0.24
Type II Error	0.22	0.48	0.38	0.38	0.32

Results show disease-present (lung cancer, lobar pneumonia and pulmonary tuberculosis) can be successfully discriminated from disease-absent (normal lung) however, the lowest rate of misclassification for discrimination of two different lung diseases occurs when energy, contrast and homogeneity is involved. Results in Table 6.23 show that the proposed discrimination procedure is performed poorly for the case of PNEU and PTB discrimination.

6.9 ROC Analysis

Receiver operating characteristic (ROC) is a fundamental method to diagnostic test evaluation when a given disease is discriminated from normal (Griner, Mayewski, Mushlin & Greenland, 1981; Metz, 1978; Zweig & Campbell, 1993).

In the discriminating between disease-present and disease-absent, four possible ways may be occurred:

1) Unhealthy case is detected as unhealthy case truly which the probability so called true positive fraction (TPF),
2) Unhealthy case is detected as healthy case wrongly which the probability so called false negative fraction (FNF),
3) Healthy case is detected as healthy case truly which the probability so called true negative fraction (TNF),

4) Healthy case is detected as unhealthy case wrongly which the probability so called false positive fraction (FPF).

It should be noted that TPF + FNF = 1 and TNF + FPF = 1. It is also noticeable that FNF is equivalent to probability of Type I Error (α) and FPF is equivalent to probability of Type II Error (β).

The performance of the discrimination procedure is indicated in terms of the size of the α and β errors for the case of equal misclassification costs and equal a prior probabilities (see Table 6.18 to Table 6.23). In practice this assumption does not hold and instead all possible combinations of these parameters should be considered for a given texture measure. This problem may be solved by calculating α and β for all possible values of $C = \left(\frac{c(1|2)}{c(2|2)}\right)\left(\frac{p_2}{p_1}\right)$ and then calculate TPF and FPF. A plot of (FPF , TPF) for increasing values of C greater than zero is defined as an ROC curve for the texture measure considered. The choice of two texture measures is made by comparing their corresponding ROC curves. The ROC curve which is left most and highest will imply that the corresponding texture measure should be preferred.

The ability of each texture measures for discriminating pair-wise of NL, LC, PNEU and PTB was illustrated with ROC curves. Figure 6.22 illustrates that the performance of proposed discrimination procedure is may better when texture measures of energy or homogeneity is used as image feature for either LDF or QDF.

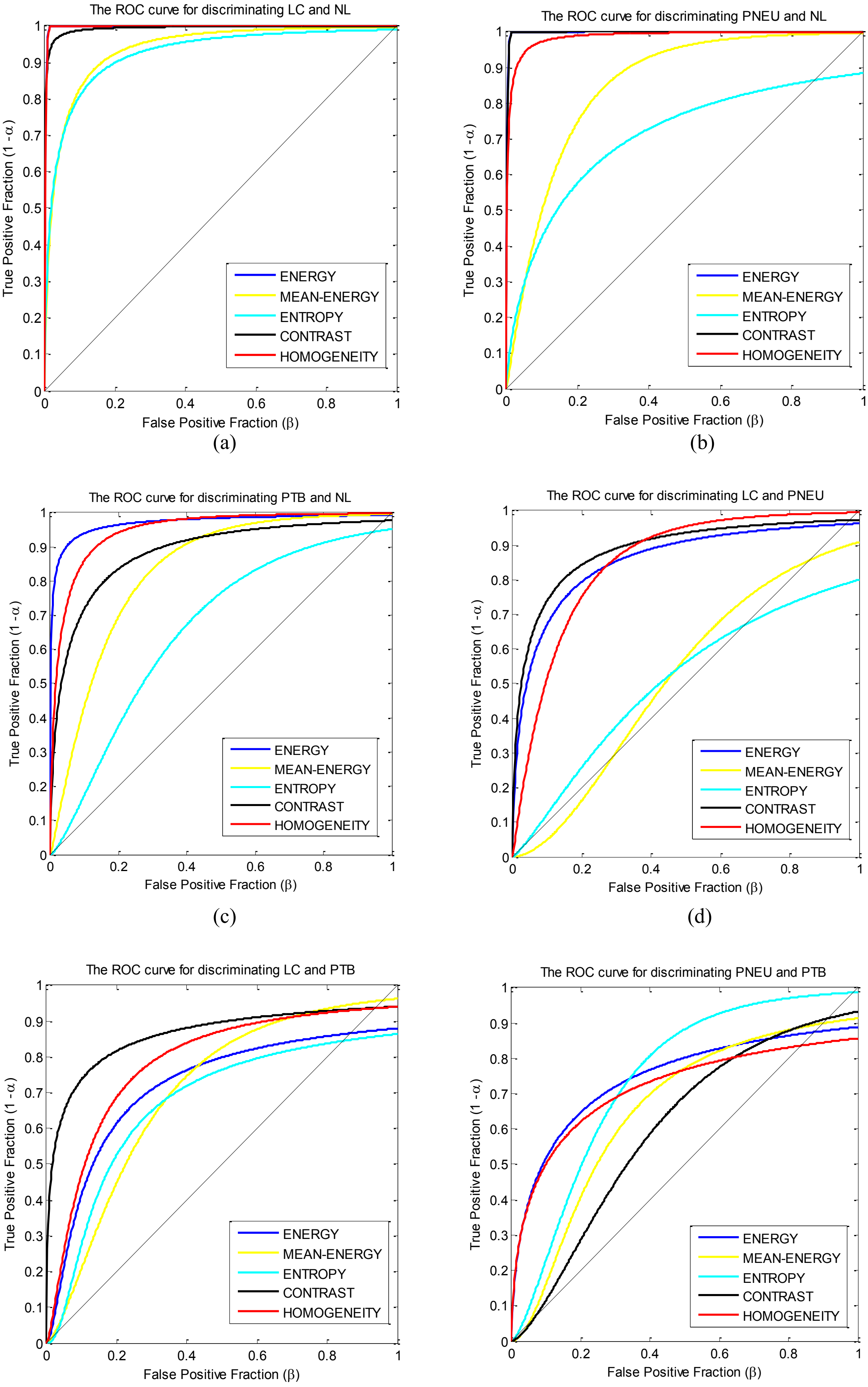
The ROC curve for discriminating LC and NL

The ROC curve for discriminating PNEU and NL

The ROC curve for discriminating PTB and NL

The ROC curve for discriminating LC and PNEU

The ROC curve for discriminating LC and PTB

The ROC curve for discriminating PNEU and PTB

(a) (b) (c) (d) (e) (f)

Figure 6.22: The ROC curves for discriminating (a) LC and NL, (b) PNEU and NL, (c) PTB and NL, (d) LC and PNEU, (e) LC and PTB and (f) PNEU and PTB.

CHAPTER 7

PROTOTYPE OF A CAD SYSTEM

The combination and capabilities of the semi automatic procedure to find the ROI and the procedure of discriminating between disease-absent and disease-present cases should be verified by the radiologists. Before this could be done the combination of methods and procedures suggested in this study should be encompassed in a form which may be conveniently used or tested by the radiologists. In particular, a prototype CAD system was proposed and is detailed in this chapter.

7.1 Semi Automatic CAD System

The proposed CAD system is composed with two main procedures, segmentation and discrimination. The procedures were developed in MATLAB R2011b environment and a semi automatic CAD system was developed using MATLAB Graphical User Interface (GUI). Three different CAD systems were created separately for lung cancer detection, lobar pneumonia detection and pulmonary tuberculosis detection based on discrimination of disease-absent and disease-present as discussed in Chapter 6 (see Figure 7.1, Figure 7.2 and Figure 7.3).

Without loss of generality, the structure of the semi automatic CAD system for lung cancer is described as follows:

1) Reading and loading a digital chest radiograph image: An arbitrary chest X-ray image was read and saved.
2) Cropping the lungs : lungs are selected by choosing a landmark, the cervical vertebrae, C7, and the extreme end points of the right lung and left lung.
3) Lung segmentation: the cropped image was then converted to a binary image with a non-overlap block processing technique using area moments (the technique was discussed in Chapter 5).
4) Location or detection of ROI: From Step (3), white pixels represent normal healthy lung and black pixels represent non-healthy lung in the binary image. The binary image was then divided into six zones, and the ratio of the number of white pixels from a pair boxes determines the ROI (see Chapter 5). Henceforth, when the ratio is close to one, the value indicate healthy lung. When the ratio is significantly bigger than one, it indicates the ROI is on the right lung otherwise it is on the left lung.
5) Cropping the ROI: After Step (4) all black pixels in the selected box are converted to its original pixel values.
6) Transform the ROI using phase congruency model: the ROI in original pixel values was then converted to PC(x) (the technique was discussed in Chapter 6).
7) Feature extraction and lung disease detection: For LC-NL pair wise discrimination, the homogeneity texture measure was calculated and used as the feature in the quadratic discriminant function (the technique was discussed in Chapter 6). The appropriate texture measures will be calculated for the other two CAD systems.
8) Results: Confirmation of disease and its location displayed.

7.2 GUI of Prototype CAD System

The button "Help" is a general guide for users of the proposed CAD system. The button "Select an image" allows users to browse and select an arbitrary chest radiograph from a patient's data base. The selected original chest radiograph image is shown in diagram A, Figure 7.1. The CAD system then ask the user to crop the image by clicking on the middle of the cervical vertebrae, C7, and the extreme end points of the left lung and right lung. The cropped image is then shown in diagram B, Figure 7.1. Next, clicking on the button "Convert to binary format", segments the lungs and highlights the region of infection (ROI) by black pixels within the lungs. The segmented binary image of the lung is displayed in diagram C, Figure 7.1 and this is followed by a display of a text message indicating the location of the ROI. However the user may still select his ROI based on the collective information from diagram A, diagram B and diagram C in Figure 7.1. The Auto selected ROI in original pixel value is shown in diagram D, Figure 7.1. The button "Convert to PC model" transforms the ROI into PC-values (see diagram E, Figure 7.1). The CAD system then calculates the texture measure and uses it in the discriminant function. Although user is free to put any C-value, The optimal discrimination is valid when $C = 1$ is assigned. The auto detection result will then displayed. The "RESET" button will allow the user to restart the program. The CAD system can be closed by clicking on "EXIT' button.

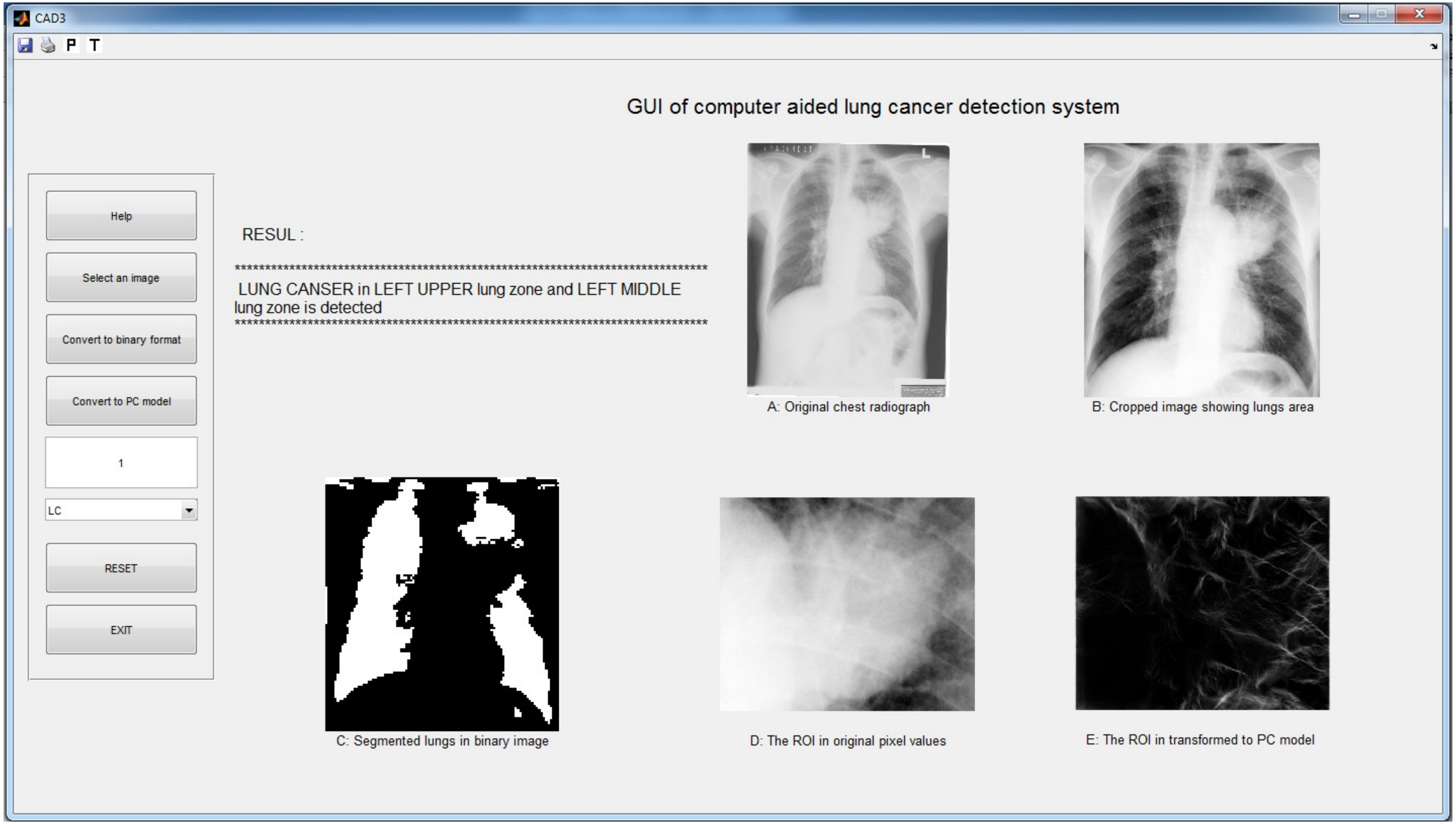

GUI of computer aided lung cancer detection system

1

LC

```
RESUL :

******************************************************************************
 LUNG CANSER in LEFT UPPER lung zone and LEFT MIDDLE
lung zone is detected
******************************************************************************
```

Figure 7.1: GUI of CAD system for lung cancer cases. The texture measure used is homogeneity.

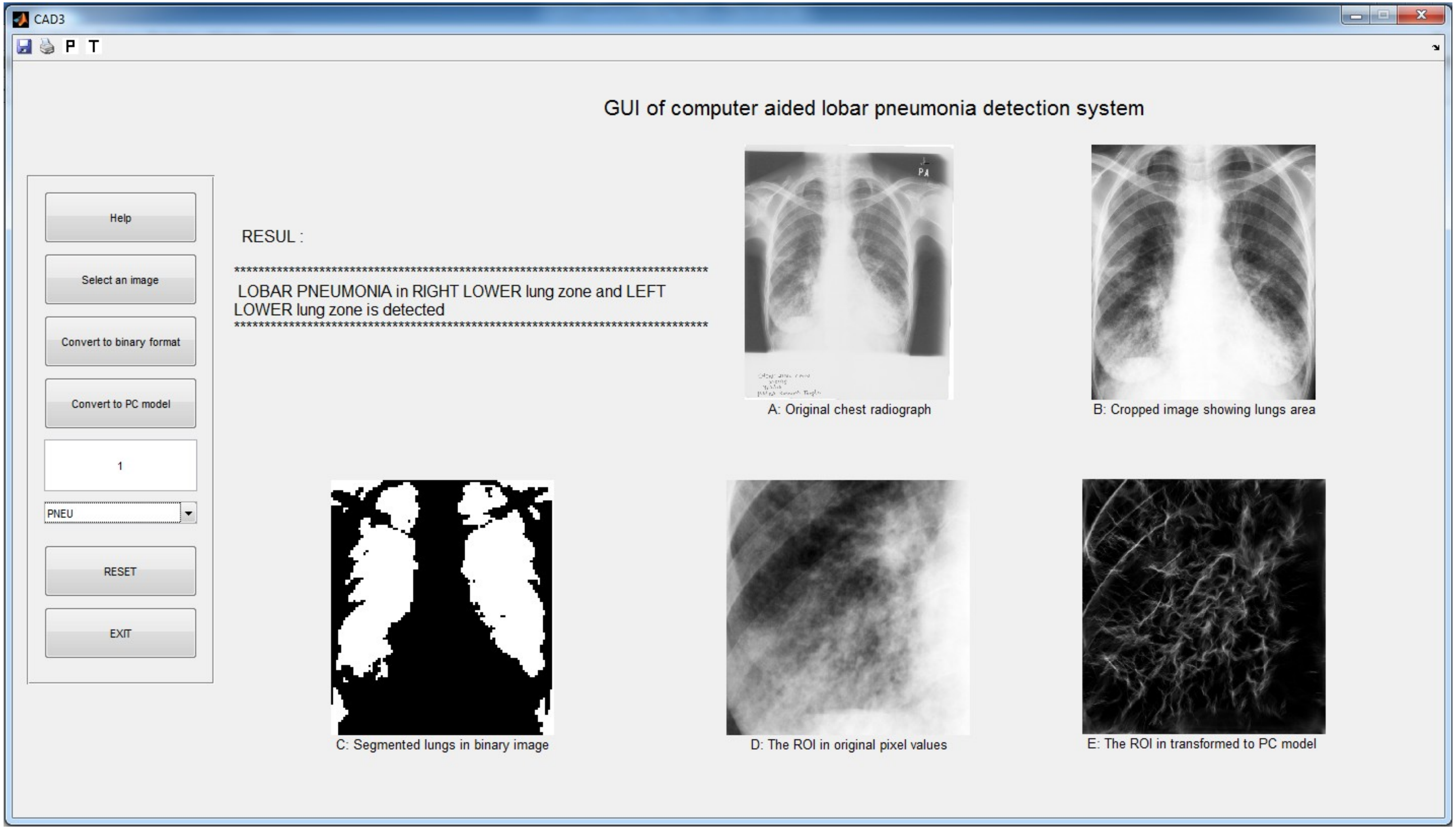

GUI of computer aided lobar pneumonia detection system

```
RESUL :
*********************************************************************************
LOBAR PNEUMONIA in RIGHT LOWER lung zone and LEFT
LOWER lung zone is detected
*********************************************************************************
```

Figure 7.2: GUI of CAD system for lobar pneumonia cases. The texture measure used is energy.

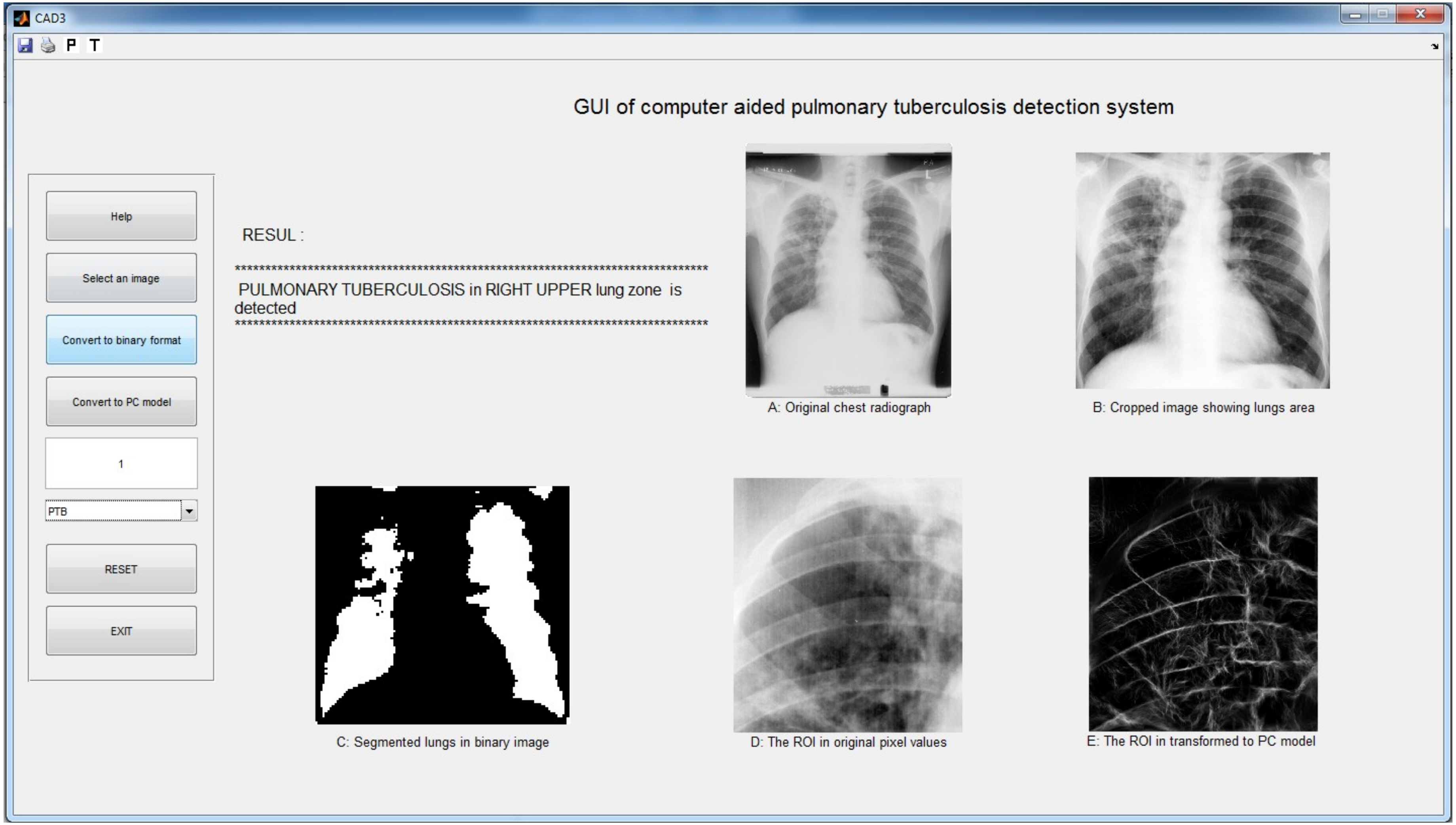

GUI of computer aided pulmonary tuberculosis detection system

```
RESUL :

********************************************************************************
 PULMONARY TUBERCULOSIS in RIGHT UPPER lung zone  is
detected
********************************************************************************
```

A: Original chest radiograph

B: Cropped image showing lungs area

C: Segmented lungs in binary image

D: The ROI in original pixel values

E: The ROI in transformed to PC model

Figure 7.3: GUI of CAD system for pulmonary tuberculosis cases. The texture measure used is energy.

CHAPTER 8

DISCUSSION AND CONCLUSION

8.1 Discussion

The main objective of this study is to develop statistical methods to solve the difficult problem of discriminating lung diseases using chest radiograph. Although diagnosing lung diseases is mainly based on the results of pathological and clinical tests, radiological tests are also widely used. Further, economic considerations dictate the wide use of chest X-ray images especially in developing countries.

A difficult and still unsolved problem in statistical discrimination is the separation of two very similar populations. The image data from digital chest radiographs were seen to be very similar and usually discrimination methods will fail in this situation. The bulk of this study concentrate on finding appropriate feature vectors to represent normal lungs (NL), lung cancer (LC), lobar pneumonia (PNEU) and pulmonary tuberculosis (PTB) so that discrimination can be performed with high confidence. A further problem for discrimination arises since the region of infection (ROI) in the chest X-ray does not appear in standard shape, size and configuration making visual interpretations difficult, and therefore, developing discrimination systems may solve or minimize the problem.

This study begins when statistical area moments were used to segment the lung area. Then a simple approximate procedure was proposed for detecting the ROI. The original pixel values of the ROI were transformed to its corresponding phase congruency values, and consequently, transformed to appropriate texture measures. These texture measures were found to be normally distributed and hence used as features in optimal discriminant functions which are either the linear discriminant function (LDF) or quadratic discriminant function (QDF). This procedure works well with the disease-present and disease-absent cases for example, discriminating between lung cancer and normal lung.

The texture measure homogeneity was found to be the best feature for discriminating LC from NL. For the discrimination of PNEU from NL as well as PTB from NL, the texture measure energy was selected. These results are true for the case $C = 1$ (total ignorance) and therefore a Receiver Operating Characteristic (ROC) analysis was carried out. The ROC curves represent all possible values of C and it reconfirms homogeneity and energy as the best choice of features for discrimination.

The results thus far should be verified by the radiologist or medical practitioner. Therefore three prototype CAD systems were separately developed for the LC-NL discrimination, PNEU-NL discrimination and PTB-NL discrimination cases.

8.2 Conclusion

Phase congruency values in the form of texture measures have the ability to discriminate LC from NL, PNEU from NL and PTB from NL with high confidence. This texture measures also have good discriminatory properties for the discrimination problem between LC and PNEU. A simple approximate procedure for detecting the region of infection (ROI) combined with the discrimination procedure produced a prototype computer aided diagnosis (CAD) system to solve the disease-present and disease-absent discrimination problem. However the CAD system has not been verified and should be considered for future studies.

APPENDIX

A: Filter Bank Design

In this section a filter bank which is used in the performance of phase congruency model is designed. The algorithm is explained with a simple example for image of size 5 x 5. Results of each stage is illustrated on an image of size 512 x 512.

With shifting the origin from left top corner to the center, position of pixels are relabelled respect to the central origin (see Figure A.1).

$$\begin{matrix} p_{1,1} & p_{1,2} & p_{1,3} & p_{1,4} & p_{5,1} \\ p_{2,1} & p_{2,2} & p_{2,3} & p_{2,4} & p_{5,2} \\ p_{3,1} & p_{3,2} & p_{3,3} & p_{3,4} & p_{5,3} \\ p_{4,1} & p_{4,2} & p_{4,3} & p_{4,4} & p_{5,4} \\ p_{5,1} & p_{5,2} & p_{5,3} & p_{5,4} & p_{5,5} \end{matrix} \Rightarrow \begin{matrix} p_{-2,-2} & p_{-1,-2} & p_{0,-2} & p_{1,-2} & p_{2,-2} \\ p_{-2,-1} & p_{-1,-1} & p_{0,-1} & p_{1,-1} & p_{2,-1} \\ p_{-2,0} & p_{-1,0} & p_{0,0} & p_{1,0} & p_{2,0} \\ p_{-2,1} & p_{-1,1} & p_{0,1} & p_{1,1} & p_{2,1} \\ p_{-2,2} & p_{-1,2} & p_{0,2} & p_{1,2} & p_{2,2} \end{matrix}$$

Figure A.1: Relabeling the pixel positions in terms of polar coordinate system.

Pixel positions are normalized in terms of polar coordinate system where $r = \sqrt{x^2 + y^2}$ and $\theta = \tan^{-1}\left(\frac{-y}{x}\right)$. Radial and radius of each pixel respect to center is given in Table A.1.

Table A.1: Values of radial and radius for an image of size 5 x 5.

r					θ				
0.7071	0.5590	0.5000	0.5590	0.7071	2.3562	2.0344	1.5708	1.1071	0.7854
0.5590	0.3536	0.2500	0.3536	0.5590	2.6779	2.3562	1.5708	0.7854	0.4636
0.5000	0.2500	0.0000	0.2500	0.5000	-3.1416	-3.1416	0.0000	0.0000	0.0000
0.5590	0.3536	0.2500	0.3536	0.5590	-2.6779	-2.3562	-1.5708	-0.7854	-0.4636
0.7071	0.5590	0.5000	0.5590	0.7071	-2.3562	-2.0344	-1.5708	-1.1071	-0.7854

Radial and Radius of pixel positions for a given image of size 512 x 512 is illustrated in Figure A.2.

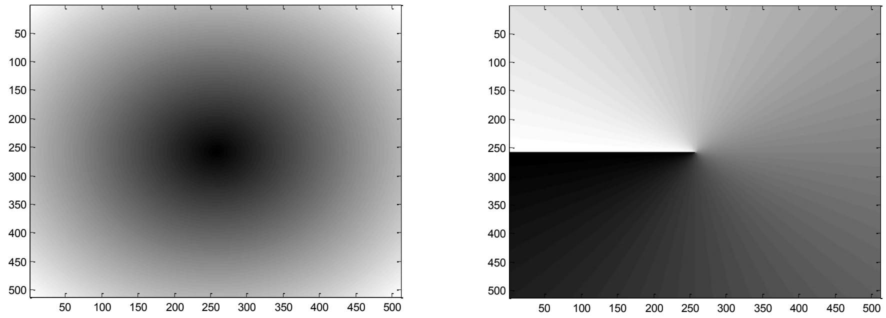

(a) (b)

Figure A.2: Illustrating the values of (a) radius and (b) radial for an image of size 512 x 512.

Again the pixel at center is shifted to top corner. This is done with cross swapping the right bottom quadrate with left top quadrate and right top quadrate with left bottom quadrate left in both radial and radius matrices.

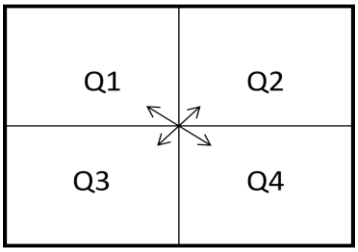

Figure A.3: Cross swapping in a given matrix.

Cross swapped matrices for an image of size 5 x 5 is given in Table A.2 and for an image of size 512 x 512 is shown in Figure A.4.

Table A.2: Cross swapped matrices of radial and radius for an image of size 5 x 5.

r					θ				
1.0000	0.2500	0.5000	0.5000	0.2500	0.0000	0.0000	0.0000	-3.1416	-3.1416
0.2500	0.3536	0.5590	0.5590	0.3536	-1.5708	-0.7854	-0.4636	-2.6779	-2.3562
0.5000	0.5590	0.7071	0.7071	0.5590	-1.5708	-1.1071	-0.7854	-2.3562	-2.0344
0.5000	0.5590	0.7071	0.7071	0.5590	1.5708	1.1071	0.7854	2.3562	2.0344
0.2500	0.3536	0.5590	0.5590	0.3536	1.5708	0.7854	0.4636	2.6779	2.3562

Note that the value of radius at left top corner is replaced by one (a value bigger than maximum value of radius) to get rid of zero frequency point.

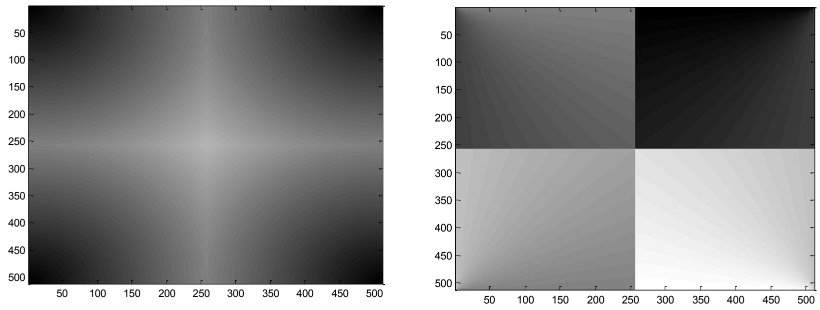

(a) (b)

Figure A.4: Illustration of cross swap for radius (a) and radial (b).

The Filter bank is constructed by multiply two radial and angular components. The radial component controls the frequency bandwidths and the angular component controls the orientations.

The radial filter components is constructed with a low pass filter which forsakes zero at the boundaries. The low-pass filter is defined as $lp = \frac{1}{1+\left(\frac{r}{c}\right)^{2n}}$ where *r* is radius and *c* is a cut-off frequency. the value *n* which filter order controls sharpness of filter.

Assuming $c = 0.45$ and $n = 15$ the low pass filter in term of radius components are given in Table A.3 and Figure A.5.

Table A.3: Low pass filter values for a given image of size 5 x 5.

1.0000	1.0000	0.0407	0.0407	1.0000
1.0000	0.9993	0.0015	0.0015	0.9993
0.0407	0.0015	0.0000	0.0000	0.0015
0.0407	0.0015	0.0000	0.0000	0.0015
1.0000	0.9993	0.0015	0.0015	0.9993

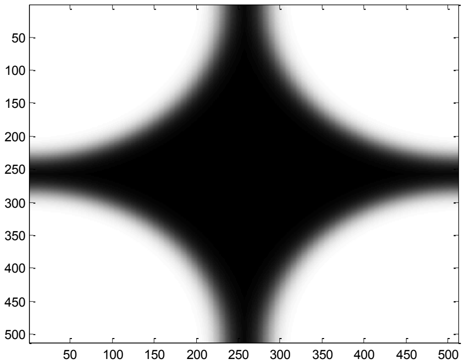

Figure A.5: Illustration of the low pass filter.

On the linear frequency scale the log-Gabor function has a transfer function form of $g(r) = e^{\frac{-\left(\log\left(\frac{r}{f}\right)\right)^2}{2(\log\sigma)^2}}$ where f is the filter's centre frequency and σ is a constant to obtain shape ratio filters.

Wavelength of a signal when is moving with constant speed is determined by $\lambda = \frac{v}{f}$ where *v* obtains the speed. In image analysis the center frequency is defined by $f = \frac{1}{\lambda}$ where the wavelength at scale *n*, is determined by $\lambda = \lambda_{\min} \,.\, \alpha^{n-1}$ where $\lambda_{\min}$ is the wavelength of smallest scale filter and α is the scaling factor between successive filters.

Log-Gabor values for a given image of size 5 x 5 and image of size 512 x 512 are given in Table A.4 and illustrated in Figure A.6.

Table A.4: Values of log-Gabor function for a given image of size 5 x 5.

0.1848	0.8907	0.7945	0.7945	0.8907
0.8907	0.9952	0.6880	0.6880	0.9952
0.7945	0.6880	0.4533	0.4533	0.6880
0.7945	0.6880	0.4533	0.4533	0.6880
0.8907	0.9952	0.6880	0.6880	0.9952

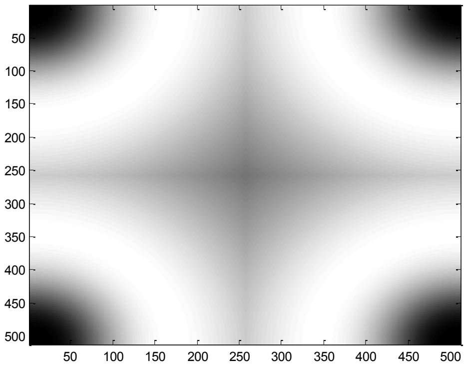

Figure A.6: Illustration of log-Gabor filter.

Finally the radial component of filter is constructed by multiplying the low pass filter values to the log-Gabor values to ensure that there is no extra frequency at the corners.

Table A.5: Values of radial component values for a given image of size 5 x 5.

0.1848	0.8907	0.0323	0.0323	0.8907
0.8907	0.9944	0.0010	0.0010	0.9944
0.0323	0.0010	0.0000	0.0000	0.0010
0.0323	0.0010	0.0000	0.0000	0.0010
0.8907	0.9944	0.0010	0.0010	0.9944

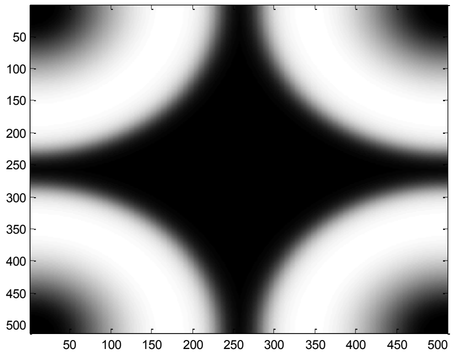

Figure A.7: Illustration of radial component.

Angular spread of each filter is given by $G(\theta) = e^{\frac{-(\theta-\theta_o)^2}{2\sigma_\theta}}$ where θ_o, the orientation angle of the filter, is given by $\theta_0 = \frac{(o-1)\pi}{n_o}$ where *o* denotes the number of current orientation and n_o is the total number of filter orientation. For example filter angles over six orientations are $\theta_1 = 0$, $\theta_2 = \frac{\pi}{6}$, $\theta_3 = \frac{\pi}{3}$, $\theta_4 = \frac{\pi}{2}$, $\theta_5 = \frac{2\pi}{3}$ and $\theta_6 = \frac{5\pi}{6}$. The σ_θ which is standard deviation of the Gaussian spreading functions in the angular direction is calculated by $\sigma_\theta = \frac{\pi}{d\,.\,n_o}$ where d is the ratio of angular interval between filter orientations and the standard deviation of the angular Gaussian function.

In a simple case with assuming *d*=1 the angular filter component over only one orientation is given by $G(\theta) = e^{\frac{-\theta^2}{2\pi^2}}$ where $\theta_1 = 0$ and $\sigma_\theta = \pi$.

Angular filter component values for a given image of size 5 x 5 are listed in Table A.6 when the values *d* = 1 and *o* = 1 are selected. Figure A.8 illustrates the angular filter component for image of size 512 x 512.

Table A.6: Values of angular filter component for an image of size 5 x 5.

1.0000	1.0000	1.0000	0.6065	0.6065
0.8825	0.9692	0.9892	0.6954	0.7548
0.8825	0.9398	0.9692	0.7548	0.8108
0.8825	0.9398	0.9692	0.7548	0.8108
0.8825	0.9692	0.9892	0.6954	0.7548

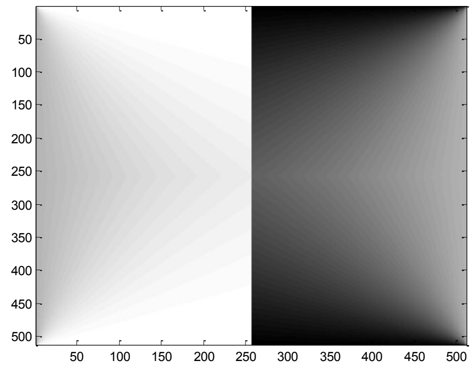

Figure A.8: Illustration of angular filter component.

Finally filter bank is designed when radial filter component multiplies with angular filter component. The designed filter bank values is listed in Table A.7 and illustrated in Figure A.9.

Table A.7: Values of designed filter with combination of radial and angular components for image of size 5 x 5.

0.0000	0.8907	0.0323	0.0196	0.5402
0.7860	0.9638	0.0010	0.0007	0.7506
0.0285	0.0010	0.0000	0.0000	0.0008
0.0285	0.0010	0.0000	0.0000	0.0008
0.7860	0.9638	0.0010	0.0007	0.7506

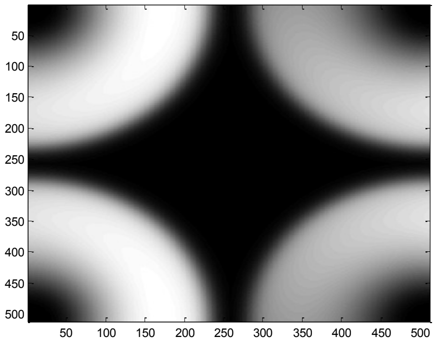

Figure A.9: The designed filter with combination of radial and angular components.

B: Example of Phase Congruency Calculation

Phase congruency values for a one dimension signal at point *x* can be calculated in terms of Fourier series expansion. Definition of Fourier series expansion is given in Section 2.5.

B.1 Fourier Series Expansion

Let *f*(*x*) is a step function with form of $f(x)=\begin{cases}+1 & -\pi \le x < 0 \\ -1 & 0 \le x < \pi\end{cases}$, shown in Figure B.1.

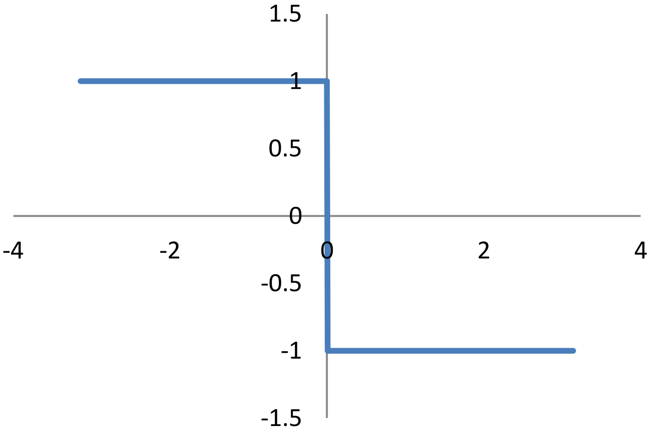

Figure B.1: Square wave on $[-\pi,\pi]$ with amplitude 1 and -1.

The calculation of Fourier components is as follow:

Since *f*(*x*) is an odd symmetric function $a_0 = 0, a_n = 0$ and

$$
\begin{aligned}
b_n &= \frac{1}{\pi}\int_{-\pi}^{\pi} f(x)\sin(nx)dx \\
&= \frac{1}{\pi}\left[\int_{-\pi}^{0}\sin(nx)dx - \int_{0}^{\pi}\sin(nx)dx\right] \\
&= \frac{1}{n\pi}\left[-\cos(nx)\big|_{-\pi}^{0} + \cos(nx)\big|_{0}^{\pi}\right] = -\frac{4}{n\pi}
\end{aligned}
$$

f(*x*) is then decomposed as

$$f(x) = \sum_{\substack{n=1 \\ odd}}^{\infty} -\frac{4}{n\pi}\sin(nx) \text{ or alternatively } f(x) = \sum_{\substack{n=1 \\ odd}}^{\infty} -\frac{4}{n\pi}\cos(nx - \frac{\pi}{2}).$$

Figure B.2 shows the square wave and five first corresponding Fourier components when $n = \{1,3,5,7,9\}$.

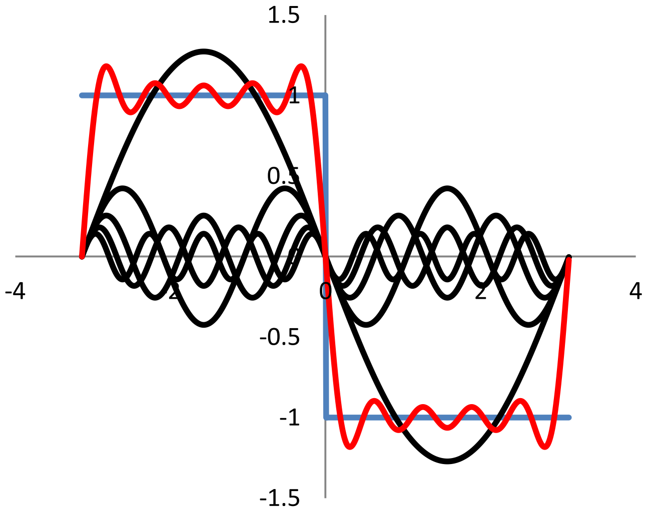

Figure B.2: Square wave (blue) decomposed in five components (black).
Estimated curve is showing by red.

It is noticeable that all Fourier components are in-phase at the step $x = 0$.

B.2 Direct Calculation of Phase Congruency Based on Definition

The step function with form of $f(x)=\begin{cases}+1 & -\pi \le x < 0 \\ -1 & 0 \le x < \pi\end{cases}$ is decomposed to $f(x)=\sum_{\substack{n=1 \\ odd}}^{\infty} -\frac{4}{n\pi}\cos\left(nx-\frac{\pi}{2}\right)$, where $A_n = \frac{4}{n\pi}$ is amplitude of n^{th} Fourier component and $\phi_n(x) = nx - \frac{\pi}{2}$ represents the local phase of the Fourier component.

Amplitude and local phase of first five Fourier components at two points $x = 0$ and $x = \frac{\pi}{2}$ are listed in Table B.1.

Table B.1: Amplitude and local phase values of the square wave for 1,3,5,7,9 Fourier components.

Number of components	$x=0$		$x=\frac{\pi}{2}$	
	Amplitude	Phase	Amplitude	Phase
1	$A_1 = \frac{4}{\pi}$	$\phi_1(0) = -\frac{\pi}{2}$	$A_1 = \frac{4}{\pi}$	$\phi_1\left(\frac{\pi}{2}\right) = 0$
3	$A_3 = \frac{4}{3\pi}$	$\phi_3(0) = -\frac{\pi}{2}$	$A_3 = \frac{4}{3\pi}$	$\phi_3\left(\frac{\pi}{2}\right) = \pi$
5	$A_5 = \frac{4}{5\pi}$	$\phi_5(0) = -\frac{\pi}{2}$	$A_5 = \frac{4}{5\pi}$	$\phi_5\left(\frac{\pi}{2}\right) = 2\pi$
7	$A_7 = \frac{4}{7\pi}$	$\phi_7(0) = -\frac{\pi}{2}$	$A_7 = \frac{4}{7\pi}$	$\phi_7\left(\frac{\pi}{2}\right) = 3\pi$
9	$A_9 = \frac{4}{9\pi}$	$\phi_9(0) = -\frac{\pi}{2}$	$A_9 = \frac{4}{9\pi}$	$\phi_9\left(\frac{\pi}{2}\right) = 4\pi$
	$\sum_{n=1}^{9} A_n = 2.2757$	$\bar{\phi}(0) = -\frac{\pi}{2}$	$\sum_{n=1}^{9} A_n = 2.2757$	$\bar{\phi}\left(\frac{\pi}{2}\right) = 0$

The magnitude of amplitude and local phase are illustrated in Figure B.3.

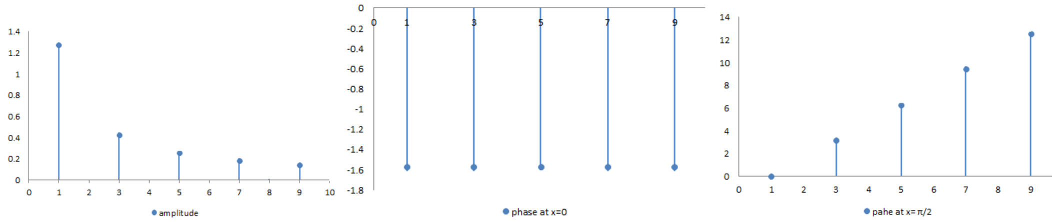

Figure B.3: Value of amplitude and local phases at point $x = 0$ and $x = \pi/2$.

Phase congruency at point x is calculated by

$$PC(x) = \max_{\bar{\phi} \in [0,2\pi]} = \frac{\sum_n A_n \cos(\phi_n(x) - \bar{\phi}(x))}{\sum_n A_n} .$$

PC(x) will be estimated when only five Fourier components are involved. PC(x) value at point $x = 0$ (in-phase point) is

$$\phi_n(x) = \bar{\phi}(x) = -\frac{\pi}{2} \Rightarrow (\phi_n(x) - \bar{\phi}(x)) = 0 \Rightarrow \cos(\phi_n(x) - \bar{\phi}(x)) = 1 ,$$

$$PC(0) = \max_{\bar{\phi} \in [0,2\pi]} \frac{\sum_n A_n \cos(\phi_n(x) - \bar{\phi}(x))}{\sum_n A_n} = 1 ,$$

PC(x) value at point $x = \frac{\pi}{2}$ is

$$\bar{\phi}(x) = 0 \Rightarrow (\phi_n(x) - \bar{\phi}(x)) = \phi_n(x) \Rightarrow \cos(\phi_n(x) - \bar{\phi}(x)) = \cos(\phi_n(x)) ,$$

$$\sum_n A_n \cos(\phi_n(x) - \bar{\phi}(x)) = 1.0631 .$$

$$\mathrm{PC}\left(\frac{\pi}{2}\right) = \max_{\bar{\phi}\in[0,2\pi]} \frac{\sum_n A_n \cos(\phi_n(x) - \bar{\phi}(x))}{\sum_n A_n} = \frac{1.0631}{2.2757} = 0.4671 .$$

B.3 Calculation of Phase Congruency in Terms of Local Energy

Phase congruency is related to local energy by $\mathrm{PC}(x) = \frac{E(x)}{\sum_n A_n}$ where local energy is given by $E(x) = \sqrt{F^2(x) + H^2(x)}$, $F(x)$ is the Fourier Transform of the signal after removing its DC component, and $H(x)$ is Hilbert transform of $F(x)$. Note that Hilbert transform shifts $\frac{\pi}{2}$ in a given phase. Since DC-component of $f(x)$ is equal to zero, then

$$F(x) = f(x) = \sum_{\substack{n=1\\ odd}}^{9} -\frac{4}{n\pi}\cos(nx - \frac{\pi}{2}) \text{ and } H(x) = \sum_{\substack{n=1\\ odd}}^{9} -\frac{4}{n\pi}\sin(nx - \frac{\pi}{2}) .$$

Local energy at point x=0 is calculated by

$$\left.\begin{array}{l} F(0) = 0 \\ H(0) = \sum_{\substack{n=1\\ odd}}^{9} \frac{4}{n\pi} = 2.2757 \end{array}\right. \Rightarrow E(0) = 2.2757 .$$

Since $\sum_n A_n = 2.2757$; thus $\mathrm{PC}(0) = \frac{E(0)}{\sum_n A_n} = 1$.

At point $x = \frac{\pi}{2}$ local energy is calculated by

$$\left.\begin{array}{l} F\left(\frac{\pi}{2}\right) = 1.0631 \\ H\left(\frac{\pi}{2}\right) = 0 \end{array}\right. \Rightarrow E\left(\frac{\pi}{2}\right) = 1.0631 .$$

Since $\sum_n A_n = 2.2757$; thus $\mathrm{PC}\left(\frac{\pi}{2}\right) = \frac{E\left(\frac{\pi}{2}\right)}{\sum_n A_n} = 0.4671$.

Phase congruency values calculated in terms local energy is equal to PC-value when calculated directly.

REFERENCES

Aberle, D., Adams, A., Berg, C., Black, W., Clapp, J., Fagerstrom, R., Sicks, J. (2011). Reduced lung-cancer mortality with low-dose computed tomographic screening. *The New England Journal of Medicine, 365*(5), 395-409.

Ahmed, Z., Sayadi, M., & Faniech, F. (2009). Satellite Images features Extraction using Phase Congruency model. *International Journal of Computer Science and Network Security 9*(2), 192-197.

Arzhaeva, Y., Prokop, M., Tax, D. M. J., De Jong, P. A., Schaefer–Prokop, C. M., & van Ginneken, B. (2007). Computer-aided detection of interstitial abnormalities in chest radiographs using a reference standard based on computed tomography. *Medical Physics, 34*.

Arzhaeva, Y., Tax, D., & Ginneken, B. V. (2009). Dissimilarity-based classification in the absence of local ground truth: Application to the diagnostic interpretation of chest radiographs. *Pattern Recognition, 42*(9), 1768-1776.

Background information about tuberculosis. (2007). Denmark: World Heath Organization, The regional office for Europe.

Barbara, G. C., Carr, D. T., Lee, R. E., & Harman, E. (1998). *Living with lung cancer: a guide for patients and their families*. Florida: Triad publication co.

Barbu, T., Costin, M., & Ciobanu, A. (2010). *Content-based image recognition technique using area moments.* Paper presented at the Soft Computing Applications (SOFA), 2010 4th International Workshop on, Arad.

Beck, J., Prazdny, K., & Rosenfeld, A. (1983). *A theory of textural segmentation*. New York: Academic Press.

Beck, J., Sutter, A., & Ivry, R. (1987). Spatial frequency channels and perceptual grouping in texture segregation. *Computer Vision, Graphics, and Image Processing, 37*(2), 299-325. doi: http://dx.doi.org/10.1016/S0734-189X(87)80006-3

Boyle, P., & Levin, B. (2008). *World Cancer Report 2008*. France: International Agency for Research on Cancer.

Burlacu, A., & Lazar, C. (2008). *Image features detection using phase congruency and its application in visual servoing.* Paper presented at the Intelligent Computer Communication and Processing, ICCP. 4th International Conference on, Cluj-Napoca.

Carreira, M. J., Cabello, D., Penedo, M. G., & Mosquera, A. (1998). Computer-aided diagnoses: Automatic detection of lung nodules. *Medical Physics, 25*.

Chen, W., Shi, Y. Q., & Su, W. (2007). *Image splicing detection using 2-d phase congruency and statistical moments of characteristic function.* Paper presented at the SPIE Electronic Imaging: Security, Steganography, and Watermarking of Multimedia Contents, San Jose, CA, USA.

Clark, M., Bovik, A. C., & Geisler, W. S. (1987). Texture segmentation using Gabor modulation/demodulation. *Pattern recognition letters, 6*(4), 261-267. doi: http://dx.doi.org/10.1016/0167-8655(87)90086-9

Clark, T. J. H. (1981). *Clinical Investigation of Respiratory Disease*. London: Chaoman and Hall.

Coggins, J. M., & Jain, A. K. (1985). A spatial filtering approach to texture analysis. *Pattern recognition letters, 3*(3), 195-203. doi: http://dx.doi.org/10.1016/0167-8655(85)90053-4

Corne, J., Carroll, M., Delany, D., & Moxham, J. (2002). *Chest X-ray made easy*: Churchill Livingstone.

Crofton, J., Horne, N., & Miller, F. (1992). *Clinical tuberculosis*. London: Macmillan.

Cross, G. R., & Jain, A. K. (1983). Markov random field texture models. *Pattern Analysis and Machine Intelligence, IEEE Transactions on, 5*(1), 25-39. doi: 10.1109/TPAMI.1983.4767341

Curado, M. P., & Cáncer, (2008). Cancer incidence in five continents.

Davis, L., Clearman, M., & Aggarwal, J. (1981). An empirical evaluation of generalized cooccurrence matrices. *Pattern Analysis and Machine Intelligence, IEEE Transactions on, 3*(2), 214-221. doi: 10.1109/TPAMI.1981.4767084

DeFrances, C. J., Lucas, C. A., Buie, V. C., & Golosinskiy, A. (2008). 2006 National Hospital Discharge Survey. *US Centers for Disease Control and Prevention National Health Statistics Reports*(5), 1-20.

Dudani, S. A., Breeding, K. J., & McGhee, R. B. (1977). Aircraft Identification by Moment Invariants. *Computers, IEEE Transactions on, 26*(1), 39-46. doi: 10.1109/TC.1977.5009272

Frame, P. W. (2010). Taming the Rays-A History of Radiation and Protection. *Health Physics, 98*(1), 79.

Frank, J., & Massey, J. (1951). The Kolmogorov-Smirnov test for goodness of fit. *Journal of the American Statistical Association, 46*(253), 68-78.

Frieden, T. (2004). *Toman's Tuberculosis: case detection, treatment, and monitoring: questions and answers* (2 ed.). Gevena: World Health Organization.

Gagalowicz, A., & Graffigne, C. (1988). *Blind texture segmentation.* Paper presented at the 9th International Conference on Pattern Recognition, Rome.

Giger, M. L., Ahn, N., Doi, K., MacMahon, H., & Metz, C. E. (1990). Computerized detection of pulmonary nodules in digital chest images: use of morphological filters in reducing false-positive detections. *Medical Physics, 17*(5), 861.

Ginneken, B. V., Katsuragawa, S., HaarRomeny, B., Doi, K., & Viergever, M. A. (2002). Automatic detection of abnormalities in chest radiographs using local texture analysis. *Medical Imaging, IEEE Transactions on, 21*(2), 139-149.

Global tuberculosis control. (2011). France: World Health Organization.

Gonzalez, R. C., & Woods, R. E. (1992). *Digital Image Processing*. Massachusetts: Addison-Wesley Publishing Company.

Griner, P. F., Mayewski, R. J., Mushlin, A. I., & Greenland, P. (1981). Selection and interpretation of diagnostic tests and procedures. Principles and applications. *Annals of internal medicine, 94*(4), 557-600.

Haralick, R. M. (1979). Statistical and structural approaches to texture. *Proceedings of the IEEE, 67*(5), 786-804. doi: 10.1109/PROC.1979.11328

Hargreaves, T., & Moridi, R. (2010). *X-Ray Safety Awareness Handbook.* Ottawa, Canada: Canadaian Air Transportation Security Authority.

Harries, A. D., Maher, D., & Graham, S. (2004). *TB/HIV: a clinical manual*: WHO.

Hu, M. K. (1962). Visual pattern recognition by moment invariants. *Information Theory, IRE Transactions on, 8*(2), 179-187. doi: 10.1109/TIT.1962.1057692

Jemal, A., Siegel, R., Ward, E., Hao, Y., Xu, J., Murray, T., & Thun, M. J. (2008). Cancer statistics, 2008. *CA: a cancer journal for clinicians, 58*(2), 71-96.

Johnson, D. H., Blot, W. J., & Carbone, D. P. (2008). Cancer of the lung: non-small cell lung cancer and small cell lung cancer. In A. M.D., A. J.O., N. J.E., K. M.B. & M. W.G. (Eds.), *Abeloff's clinical oncology* (4 ed., pp. 2555). Philadelphia: Churchill Livingstone/Elsevier.

Johnson, R. A., & Wichern, D. W. (2002). Applied multivariate statistical analysis.

Julesz, B. (1981). Textons, the elements of texture perception, and their interactions. *Nature, 290*, 91-97. doi: 10.1038/290091a0

Julesz, B. (1986). Texton gradients: The texton theory revisited. *Biological Cybernetics, 54*(4), 245-251. doi: 10.1007/BF00318420

Karetzky, M., Cunha, B. A., & Brandstetter, R. D. (1993). *The pneumonias*. New York: Springer-Verlag.

Kashyap, R., Chellappa, R., & Ahuja, N. (1981). Decision rules for choice of neighbors in random field models of images. *Computer Graphics and Image Processing, 15*(4), 301-318.

Katsuragawa, S., & Doi, K. (2007). Computer-aided diagnosis in chest radiography. *Computerized Medical Imaging and Graphics, 31*(4-5), 212-223. doi: http://dx.doi.org/10.1016/j.compmedimag.2007.02.003

Keserci, B., & Yoshida, H. (2002). Computerized detection of pulmonary nodules in chest radiographs based on morphological features and wavelet snake model. *Medical Image Analysis, 6*(4), 431-447.

Kovesi, P. (1991). *A dimensionless measure of edge significance.* Paper presented at the The Aoustralian Pattern Recongnition Society, Conference on Digital Image Computing. Techniques and Applications, Melbourne.

Kovesi, P. (1993). *A dimensionless measure of edge significance from phase congruency calculated via wavelets.* Paper presented at the The First New Zealand Conference on Image and Vision Computing, Auckland.

Kovesi, P. (1999). Image features from phase congruency. *Videre: Journal of Computer Vision Research, 1*(3), 1-26.

Kovesi, P. (2003). *Phase congruency detects corners and edges.* Paper presented at the The Australian Pattern Recognition Society Conference: DICTA2003, Sydney.

Krech, R. L., Davis, J., Walsh, D., & Curtis, E. B. (1992). Symptoms of lung cancer. *Palliative medicine, 6*(4), 309-315.

Li, Q., Katsuragawa, S., & Doi, K. (2001). Computer-aided diagnostic scheme for lung nodule detection in digital chest radiographs by use of a multiple-template matching technique. *Medical Physics, 28*, 2070.

McClelland, I. R. (2004). *X-Ray Equipment Maintenance and Repairs Workbook for Radiographers and Radiological Technologists*: World Health Organization.

Metz, C. E. (1978). Basic principles of ROC analysis. *Seminars in Nuclear Medicine, 8*(4), 283-298. doi: 10.1016/S0001-2998(78)80014-2

Milton, J. S., & Arnold, J. C. (2002). *Introduction to probability and statistics: principles and applications for engineering and the computing sciences*: McGraw-Hill, Inc.

Morrone, M. C., & Burr, D. (1988). Feature detection in human vision: A phase-dependent energy model. *Proceedings of the Royal Society of London. Series B, biological sciences, 235*(1280), 221-245.

Morrone, M. C., & Owens, R. A. (1987). Feature detection from local energy. *Pattern Recognition Letters, 6*(5), 303-313. doi: http://dx.doi.org/10.1016/0167-8655(87)90013-4

Morrone, M. C., Ross, J., Burr, D. C., & Owens, R. (1986). Mach bands are phase dependent. *Nature, 324*(6094), 250-253.

Mukundan, R., & Ramakrishnan, K. (1998). *Moment functions in image analysis: theory and applications*. Singapore: World Scientific Publication.

Murphy, S. L., Xu, J. Q., & Kochanek, K. D. (2012). Deaths: preliminary data for 2010. *National Vital Statistics Reports, 4*(60).

Nakamura, K., Ohmi, A., Kurihara, T., Suzuki, S., & Tadera, M. (1970). Studies on the diagnostic value of 70 mm radiophotograms by mirror camera and the reading ability of physicians. *Kekkaku, 45*(4), 121-128.

National Heart, Lung and Blood Institute. (2007). Maryland, U.S.A: U.S. Department of Health & Human Services.

Noor, N. M., Rijal, O. M., Yunus, A., & Abu-Bakar, S. A. R. (2010). A discrimination method for the detection of pneumonia using chest radiograph. *Computerized Medical Imaging and Graphics, 34*(2), 160-166.

Noor, N. M., Rijal, O. M., Yunus, A., Mahayiddin, A. A., ChewPeng, G., & Abu-Bakar, S. (2010). *A statistical interpretation of the chest radiograph for the detection of pulmonary tuberculosis.* Paper presented at the Biomedical Engineering and Sciences (IECBES), 2010 IEEE EMBS Conference on, Kuala Lumpur.

Noor, N. M., Yunus, A., Bakar, S., Hussin, A., & Rijal, O. M. (2011). Applying a statistical PTB detection procedure to complement the gold standard. *Computerized Medical Imaging and Graphics, 35*(3), 186-194.

Oliveira, L. L. G., Ribeiro, L. H. V., de Oliveira, R. M., Coelho, C. J., & S Andrade, A. L. S. (2008). Computer-aided diagnosis in chest radiography for detection of childhood pneumonia. *International journal of medical informatics, 77*(8), 555-564.

Oppenheim, A. V., & Lim, J. S. (1981). The importance of phase in signals. *Proceedings of the IEEE, 69*(5), 529-541. doi: 10.1109/PROC.1981.12022

Owens, R., Venkatesh, S., & Ross, J. (1989). Edge detection is a projection. *Pattern recognition letters, 9*(4), 233-244. doi: http://dx.doi.org/10.1016/0167-8655(89)90002-0

Pentland, A. P. (1984). Fractal-based description of natural scenes. *Pattern Analysis and Machine Intelligence, IEEE Transactions on, 6*(6), 661-674. doi: 10.1109/TPAMI.1984.4767591

Prokop, R. J., & Reeves, A. P. (1992). A survey of moment-based techniques for unoccluded object representation and recognition. *CVGIP: Graphical Models and Image Processing, 54*(5), 438-460. doi: http://dx.doi.org/10.1016/1049-9652(92)90027-U

Rieder, H. L., Yuan, C. C., Gie, R. P., & D.A, E. (2009). *Crofton's Clinical Tuberculosis* (3rd ed.). Oxford: Macmillan Education.

Rizon, M., Yazid, H., Saad, P., Shakaff, A. Y. M., Saad, A. R., Mamat, M. R., Karthigayan, M. (2006). Object detection using geometric invariant moment. *American Journal of applied sciences, 2*(6), 1876-1878.

Rontgen, W. C. (1895). On a new kind of ray, a preliminary communication. *Wurzburg Physico-Médical Society on December, 28*.

Rosner, B. (1990). *Fundamentals of biostatistics* (3rd ed.): PWS-KENT.

Sankar, P., & Sklansky, J. (1982). A gestalt-guided heuristic boundary follower for X-ray images of lung nodules. *Pattern Analysis and Machine Intelligence, IEEE Transactions on 4*(3), 326-331.

Schilham, A. M. R., Van Ginneken, B., & Loog, M. (2006). A computer-aided diagnosis system for detection of lung nodules in chest radiographs with an evaluation on a public database. *Medical Image Analysis, 10*(2), 247-258. doi: http://dx.doi.org/10.1016/j.media.2005.09.003

Schiller, J. H., Parles, K., & Cipau, A. (2009). *100 questions & answers about lung cancer*: Jones & Bartlett Learning.

Sklansky, J., & Petkovic´, D. (1984). Two-resolution detection of lung tumors in chest radiographs. In A. Rosenfeld (Ed.), *Multiresolution Image Processing and Analysis* (pp. 365–378). Berlin: Springer.

Someda, C. G. (2006). *Electromagnetic waves*: CRC Press.

State of Lung Disease in Diverse Communities. (2010). Washington, DC: American Lung Association.

Thode, H. C. (2002). *Testing for normality*: Taylor & Francis.

Tuceryan, M. (1994). Moment-based texture segmentation. *Pattern recognition letters, 15*(7), 659-668. doi: http://dx.doi.org/10.1016/0167-8655(94)90069-8

Tuceryan, M., & Jain, A. K. (1990). Texture segmentation using Voronoi polygons. *Pattern Analysis and Machine Intelligence, IEEE Transactions on, 12*(2), 211-216. doi: 10.1109/34.44407

Tuceryan, M., & Jain, A. K. (1993). Texture Analysis. In C. H. Chen, L. F. Pau & P. S. P. Wang (Eds.), *Handbook of pattern recognition and computer vision* (pp. 996). USA: World Scientific.

Turner, M. R. (1986). Texture discrimination by Gabor functions. *Biological Cybernetics, 55*(2-3), 71-82. doi: 10.1007/BF00341922

Venkatesh, S., & Owens, R. (1989). *An energy feature detection scheme.* Paper presented at the International Conference on Image processing, Singapore.

Venkatesh, S., & Owens, R. (1990). On the classification of image features. *Pattern Recognition Letters, 11*(5), 339-349. doi: http://dx.doi.org/10.1016/0167-8655(90)90043-2

Voorhees, H., & Poggio, T. (1987). *Detecting textons and texture boundaries in natural image.* Paper presented at the First International Conference on Computer Vision, London.

Wipf, J. E., Lipsky, B. A., Hirschmann, J. V., Boyko, E. J., Takasugi, J., Peugeot, R. L., & Davis, C. L. (1999). Diagnosing pneumonia by physical examination: relevant or relic? *Archives of internal medicine, 159*(10), 1082.

Xiong, Z., Xiong, G., Man, Y., Wang, L., & Jing, W. (2010). Detection of lung cancer by oral examination. *Medical hypotheses, 74*(2), 346-347.

Yinan, S., Weijun, L., & Yuechao, W. (2003). *United moment invariants for shape discrimination.* Paper presented at the Robotics, Intelligent Systems and Signal Processing, 2003. Proceedings. 2003 IEEE International Conference on.

Zusne, L. (1965). Moments of area and of the perimeter of visual form as predictors of discrimination performance. *Journal of Experimental Psychology, 69*(3), 213. doi: 10.1037/h0021735

Zweig, M. H., & Campbell, G. (1993). Receiver-operating characteristic (ROC) plots: a fundamental evaluation tool in clinical medicine. *Clinical chemistry, 39*(4), 561-577.